



# **On the synthesis and analysis of dyes for stochastic optical reconstruction microscopy**

By

**Daniel Ray Jenkinson**

A thesis submitted in partial fulfilment of the requirements for the degree of  
Doctor of Philosophy

The University of Sheffield  
Faculty of Science  
Department of Chemistry &  
Department of Physics and Astronomy

Submission date: May 2018

# Table of Contents

|   |      |
|---|------|
| Declaration   | iv   |
| List of publications                                      | iv   |
| Abstract  | v    |
| Acknowledgements  | vii  |
| Abbreviations   | viii |
| 1 Introduction  | 1    |
| 1.1 Fluorescence in microscopy                            | 2    |
| 1.2 High-resolution fluorescence microscopy               | 5    |
| 1.3 Super-resolution fluorescence microscopy              | 7    |
| 1.4 Single molecule detection and localisation microscopy | 10   |
| 1.5 STORM   | 14   |
| 1.5.1 dSTORM and data analysis                            | 16   |
| 1.5.2 3D STORM  | 18   |
| 1.5.3 Commonly used fluorophores                          | 19   |
| 1.5.4 Theories on the blinking mechanism                  | 21   |
| 1.6 Dye modification                                      | 24   |
| 1.7 Project background                                    | 26   |
| 1.8 Aims  | 27   |
| 2 Benzochalcogenadiazole synthesis and analysis           | 29   |
| 2.1 Benzochalcogenadiazoles in the literature             | 29   |

|     |   |     |
|-----|---|-----|
| 2.2 | Dye synthesis   | 30  |
| 2.3 | Vicarious nucleophilic substitution                   | 35  |
| 2.4 | Aryl aminations                                       | 39  |
| 2.5 | Photophysical properties                              | 44  |
| 2.6 | Nanoparticle synthesis and functionalisation          | 57  |
| 2.7 | High-resolution imaging of nanoparticles              | 59  |
| 2.8 | Conclusions   | 61  |
| 3   | Rhodamine synthesis and analysis                      | 63  |
| 3.1 | Rhodamines in the literature                          | 63  |
| 3.2 | Dye synthesis   | 68  |
| 3.3 | Computational studies and solution phase analysis     | 79  |
| 3.4 | PVA blinking studies                                  | 89  |
| 3.5 | Conclusions   | 93  |
| 4   | Conclusions and future work                           | 95  |
| 5   | Experimental  | 100 |
| 6   | Appendix  | 134 |
| 6.1 | Appendix 1: MatLab code used to obtain bleaching data | 134 |
| 7   | References  | 136 |

## **Declaration**

This thesis records the work carried out in the Department of Chemistry and the Department of Physics and Astronomy, University of Sheffield, UK between October 2013 and September 2018 and is original except where acknowledged by reference.

No part of this work is being, nor has been submitted for a degree, diploma, or any other qualification at any other university.

## **List of publications**

Jenkinson, D. R., Cadby, A. J., Jones, S., “The synthesis and photophysical analysis of a series of 4-nitrobenzochalcogenadiazoles for super-resolution microscopy,” *Chemistry – A European Journal*, **23** (51), 2017, 12585-12592.

## Abstract

In this work, two series of chemically similar dyes were synthesised and tested for their ability to exhibit photoblinking – a phenomenon required for single molecule localisation (SMLM) techniques such as STORM and PALM so that individual molecules can be detected and high-resolution images can be captured. For each of the two sets of synthesised dyes (benzodiazoles and rhodamines), heteroatoms were substituted to create heteroaromatic rings with different electronic, and thus photophysical properties.

For the benzodiazole series of dyes a series of 4-nitrobenzodiazoles with atomic substitution through the chalcogen group were synthesised and analysed in solution phase, sparsely dispersed through a PVA matrix, and supported on the surface of a silica nanoparticle *via* conjugation with the silane terminated primary amine APTES. All three benzodiazole derivatives were found to be capable of photoblinking, however, it was found that benzodiazole dyes with larger atoms in their heteroaromatic system were favourable for single molecule detection techniques due to a reduced blink rate, with the sulfur containing derivative being deemed most appropriate for super-resolution imaging due to its relative ease of synthetic manipulation compared to the selenium-containing analogue. The blinking mechanism in this case was thought to be related to redox reactions with substances in the buffered solutions creating stable radicals via triplet states, which are stabilised in systems containing heavier atoms.

During the synthesis of the 2,1,3-benzoselenadiazole dye, it was necessary to utilise an aryl amination coupling reaction. Although the method was adapted due to solubility issues from a procedure found in the literature, reactions of this type had not been performed using the 4-nitrobenzodiazole construct, and so a substrate screen was undertaken. Although yields were not always impressive and were very wide ranging (6

– 87%), it was found that the 2,1,3-benzochalcogenodiazole systems could all be aminated *via* this method. Although useful substrates with functionalisable termini were screened (e.g. silanes, alkenes, amino acids), yields were highest when reacting with secondary amines.

The second series of dyes that were synthesised were a range of rhodamine dyes with variation at position 10 of the parent xanthene structure with atoms from around the p-block of the periodic table which were analysed in solution phase and sparsely dispersed through a PVA matrix. Some like-for-like atomic substitution down one group of the periodic table was explored (using silicon and germanium), and the photophysical properties of the majority of dyes were similar. It was shown that despite the absence of a 2-carboxy group on the pendant aryl ring, xanthene dyes are capable of reversible photoblinking.

The dye containing an N-oxide at position 10 behaved very differently from the other rhodamine analogues. This dye absorbed and emitted light at a drastically lower wavelength to the other dyes in the series and was not photostable to continued laser irradiation when in solution, but also proved to be capable of reversible photoswitching.

A method was used to assess whether dyes would be suitable for SMLM imaging by measuring the bleaching of fluorescence intensity with continuous laser irradiation, followed by fluorescence reactivation by repeated dissolution of oxygen into the aqueous media by agitation. Although this method was used to successfully predict the blinking properties of the benzodiazole series of dyes, the technique gave no indication that the rhodamine dyes would exhibit photoblinking under SMLM conditions – a result that was later disproved, since all five rhodamine dyes were capable of blinking. As such, this method solution phase analysis was deemed unreliable.

## Acknowledgements

I would firstly like to thank Prof Simon Jones and Dr Ashley Cadby for their continued support and guidance throughout, the Molecular Scale Engineering CDT for providing funding from the EPSRC, and the countless opportunities they provided for my personal development (even if I did sometimes moan about them at the time).

Thank you to all the staff and co-workers in the chemistry and physics departments who ran samples, gave advice, and provided training to me. Without you this thesis would have taken much longer to prepare! Particular thanks to Sandra Marshall who was always cheerful, kind, and provided enough work for me to keep my bank balance afloat!

Of course, my PhD was heavily influenced by the people who worked around me every day and I'm so grateful to all of the members of the Jones and Cadby groups, not only for giving me helpful experimental advice but also making the working environment bearable, sharing cups of tea, and joining me at our local watering hole. Special thanks go to Dr Andrew Reeder, Dr Sam Barnett, Dr Jonny Simmons, Dr Bryony Cotterell, Jenna Spencer-Briggs, and Al Fields. I have also had the luxury and honour of making friends with and working alongside people from across the wider departmental community and special mentions go to Dr Esther Allen, Dr Ash Wragg, Dr Mat Pringle, Dr Ashlie Butler, Dr Hannah Dexter, Dr Caroline Glover, Dr Zeyed Abdulkarim, Dr Alexa Cleasby, Dr Matthew Jackson, everyone that has shared the E26 office or E floor RRB corridor with me since I started my Masters project in 2012, and my fellow CDT-ers.

Last, but not least, a man without whom I probably wouldn't have finished my PhD. He kept me sane when I wanted to quit, lifted my spirits when I was low, and was a fountain of unconditional love through the good and the bad times. Thank you, Joe.

## Abbreviations

|                      |   |
|----------------------|---|
| 3D                   | Three dimensional   |
| APTES                | (3-Aminopropyl)triethoxysilane                                |
| Boc                  | <i>tert</i> -Butyloxycarbonyl group                           |
| <i>C. crescentus</i> | <i>Caulobacter crescentus</i>                                 |
| ca.                  | Circa   |
| CW                   | Continuous wave   |
| Cy                   | Cyanine   |
| d/STORM              | Direct/Stochastic optical reconstruction microscopy           |
| DCM                  | Dichloromethane   |
| DFT                  | Density functional theory                                     |
| DH-PSF               | Double helix point spread function                            |
| DIPEA                | Diisopropylethyl amine  |
| DLS                  | Dynamic light scattering                                      |
| DMAP                 | N,N-Dimethylamino pyridine                                    |
| DMSO                 | Dimethylsulfoxide   |
| DNA                  | Deoxyribonucleic acid   |
| <i>E. coli</i>       | <i>Escherichia coli</i>                                       |
| EM                   | Electron Microscopy   |
| ER                   | Endoplasmic reticulum   |
| ESR                  | Electron spin resonance spectroscopy                          |
| EtOH                 | Ethanol   |
| F/PALM               | Fluorescence/Photoactivatable localisation microscopy         |
| FITC                 | Fluorescein isothiocyanate                                    |
| FRET                 | Förster resonance energy transfer                             |
| FWHM                 | Full width at half maximum intensity of a Gaussian curve      |
| G/FP                 | Green/Fluorescent protein                                     |
| GLOX                 | Glucose oxidase   |
| GSDIM                | Ground state depletion followed by individual molecule return |
| HOMO                 | Highest occupied molecular orbital                            |
| HPLC                 | High performance liquid chromatography                        |
| IR                   | Infrared  |
| ISC                  | Intersystem crossing  |
| LSFM                 | Light sheet fluorescence microscopy                           |
| LUMO                 | Lowest unoccupied molecular orbital                           |
| <i>m/z</i>           | Mass to charge ratio  |
| MEA                  | $\beta$ -Mercaptoethylamine                                   |
| NADA                 | 4-Nitrobenzoxadiazole-D-alanine conjugate                     |
| NBD                  | 4-Nitrobenzoxadiazole   |
| NMR                  | Nuclear magnetic resonance spectroscopy                       |
| NPSe                 | 4-Nitrobenzoselenadiazole                                     |
| NPT                  | 4-Nitrobenzothiadiazole                                       |



|                                 |  |
|---------------------------------|--|
| NSOM                            | Near-field optical microscopy                                      |
| <i>P. falciparum</i>            | Plasmodium falciparum  |
| PDI                             | Polydispersity index   |
| PED                             | Pre-exponential decay  |
| PL                              | Photoluminescence  |
| PPFA                            | <i>N,N</i> -dimethyl-1-[2-(diphenylphosphino)ferrocenyl]ethylamine |
| PSF                             | Point spread function  |
| PTSA                            | <i>p</i> -Toluenesulfonic acid                                     |
| PVA                             | Polyvinyl alcohol  |
| REDOX                           | Reduction or oxidation   |
| RPM                             | Reversible photobleaching microscopy                               |
| <i>S. aureus</i>                | <i>Staphylococcus aureus</i>                                       |
| S <sub>0</sub>                  | Singlet ground state   |
| S <sub>1</sub>                  | First excited singlet state  |
| SADA                            | 4-Nitrobenzothiadiazole-D-alanine conjugate                        |
| SEM                             | Scanning electron microscopy                                       |
| SMD                             | Single molecule detection  |
| SMLM                            | Single molecule localisation microscopy                            |
| S <sub>N</sub> Ar/ <sup>H</sup> | Nucleophilic aromatic substitution/of hydrogen                     |
| SNR                             | Signal to noise ratio  |
| SPIM                            | Single plane illumination microscopy                               |
| STED                            | Stimulation emission depletion                                     |
| TCSPC                           | Time correlated single photon counting                             |
| TD-SCF                          | Time dependent self-consistent field                               |
| TFA                             | Trifluoroacetic acid   |
| THF                             | Tetrahydrofuran  |
| TIRF                            | Total internal reflection fluorescence                             |
| TLC                             | Thin layer chromatography  |
| TMHI                            | 1,1,1-Trimethylhydrazonium iodide                                  |
| TMR                             | <i>N,N,N',N'</i> -Tetramethyl rhodamine                            |
| Tris                            | Trisaminomethane   |
| UV                              | Ultra-violet   |
| UV/Vis                          | UV – visible light absorption spectroscopy                         |
| VNS                             | Vicarious nucleophilic substitution                                |
| ε                               | Molar absorption coefficient                                       |
| λ                               | Wavelength   |
| τ                               | Excited state lifetime   |
| Φ                               | Fluorescence quantum yield   |



# 1 Introduction

Imaging is a broad term used to describe the creation of visual representations of objects. In a scientific context the object in question may be, for example, a body part, a supernova many light-years away, or the interior of a cell. For centuries one of the greatest challenges facing scientists has been to visualise those objects which are very far away or too small to be detected by the human eye, but the practice of enlargement using lenses is actually millennia old.

The first instances of the magnification of objects may date back to the first century when glass was first invented and Romans investigated how curved panes could make objects appear larger, reportedly achieving up to 2.5x magnification.<sup>1</sup>

Though the creator of the first compound microscope cannot be easily identified, the invention is often attributed to the Dutch lens-maker Hans Janssen and his son Zacharias during the 1590s after the discovery that placing two lenses in line with each other amplified their effect.<sup>2</sup> Word of the device was spread in the early 17<sup>th</sup> century (ca. 1620) and gave a magnification of nine diameters. The microscope was at first widely perceived as a toy and was seen as no more than a novelty until Galileo used a converted telescope to examine ‘the organs of motion and of the senses in small animals’ such as the eyes of insects.<sup>2</sup> The earliest record of microscopic observations was published in 1625 by the Italian prince Federico Cesi and Francesco Stelluti who investigated bees in great detail, though all accounts of microscopy for the following 36 years were purely observational and made no attempt at scientific explanation.<sup>3</sup>

In 1661 Italian anatomist Malpighi used microscopy to discover the circulatory nature of blood vessels and identified alveoli in the lungs of frogs.<sup>4</sup> His use of the microscope was

the first to be considered truly scientific because it was deemed systematic and aimed to provide an explanation for a problem that existed in science.

## 1.1 Fluorescence in microscopy

From this point the design of the microscope evolved into the devices recognised today and many scientific advances were made because of it, however the limits of what could be achieved using optics were being realised by the late 1800s in terms of the magnification power of the lenses used and the aperture of the cone of rays being taken up by the objective lens. Since the resolving power of microscopes could not be increased by improving optical conditions, it was necessary to find other means with which to do so. It was thought for many years that the maximum achievable lateral ( $x,y$ ) resolution was approximately 0.2 micrometres and that this limit was fixed by a fundamental physical law. In 1873 Earnst Abbe described the resolution limit as a relationship between the wavelength of light and the angular aperture of the optical system, implying the lateral resolution limit is proportional to approximately half the wavelength of light used to illuminate the specimen (Equation 1.1).<sup>5</sup>

$$\text{Resolution } (x,y) = \lambda / 2[n.\sin(\theta)] \quad \text{Equation 1.1}$$

$\lambda = \text{wavelength}, n = \text{refractive index}, \theta = \text{aperture angle}$

It was then realised that the resolution limit could be doubled by using light of half the wavelength and exploiting ultra-violet light. It was postulated as early as 1874 that microscopic images would be better differentiated and would have higher resolutions if the microscopic subject itself were to emit light,<sup>6</sup> and in 1910 the first UV microscopes were manufactured by the firms of Carl Zeiss and C. Reichert after developing filters that could absorb all wavelengths above 400 nm. These microscopes illuminated a large area of a sample (a wide field) and measured the light emitted by fluorophores. Modern

systems include a dichroic filter which allows some wavelengths of light to be transmitted but reflects all other wavelengths (Figure 1.1).<sup>7</sup>

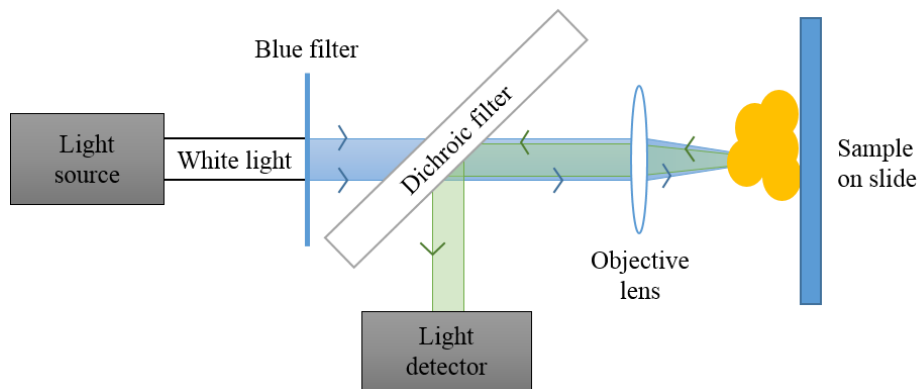


*Figure 1.1 – The simplified workings of a fluorescence microscope. White light is passed through a filter (in this case blue, or alternately a coloured laser is used) before passing through a dichroic filter and is focussed onto the sample. Fluorophores in the sample emit light (in this case green) which is reflected by the dichroic filter towards the detector.*

For a short time, this technology was only used to observe objects that give off fluorescence naturally. In 1914 Prowazek attempted to stain non-fluorescent objects with fluorescent materials in order to make them observable by fluorescence microscopy and by 1917 the technique had been used to recognise and differentiate bacterial strains. It must be admitted though that despite providing contrast, fluorescence microscopy (or epifluorescence) cannot itself increase the resolution achievable using light microscopy.

In 1955 Marvin Minsky started working towards the invention of the confocal microscope.<sup>8</sup> While studying the brain Minsky became increasingly frustrated at the fact that it was only possible to visualise one neuronal cell at a time and was hence unable to deduce the nature of how the cells within the brain were connected to form a network. Further adding to his frustrations he found that, because the neurones are so intertwined, staining large sections of the brain was unproductive and gave blurry images due to light

scattering. He set out to create a microscope that could confine each view to a thin plane in a small area.

By passing the incident light through a pinhole aperture, Minsky was able to focus the light onto small sections of the sample using point illumination (whose intensity at a point can be defined by its point spread function, PSF). Instead of illuminating the whole specimen at the same time and allowing all fluorescent molecules to emit simultaneously, point illumination ensures that only a small subset of fluorophores is radiating light at a time. To avoid scattering of the emitted light from the fluorophores a second pinhole aperture was positioned in front of the light detector (Figure 1.2).

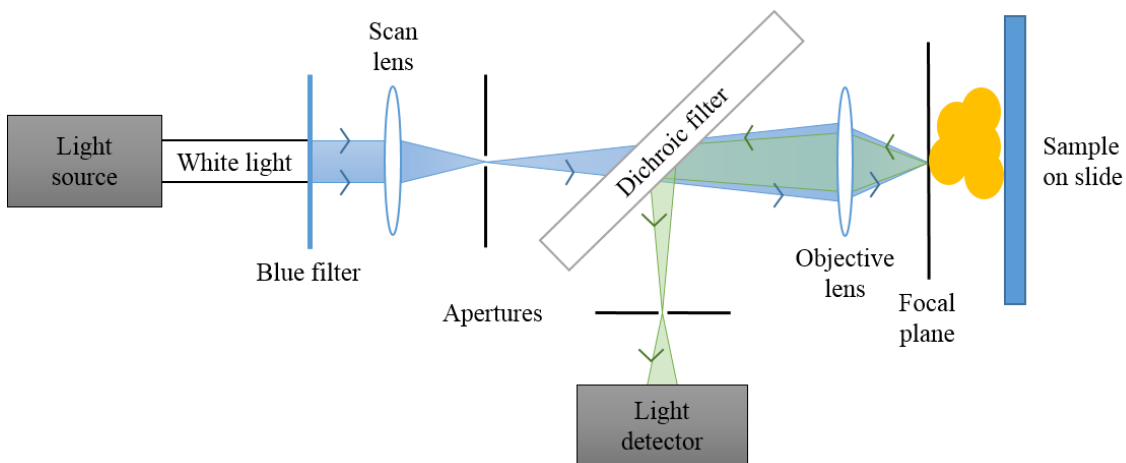


*Figure 1.2 – The simplified workings of a confocal microscope. White light is passed through a filter (in this case blue, alternately a coloured laser is used) before being focussed through an aperture. The beam is passed through a dichroic filter and focussed again onto the focal plane. Fluorophores in the sample emit light (in this case green) which is reflected by the dichroic back through an aperture to the detector.*

To capture an image of the whole sample the point illumination is scanned across it to capture a series of images that can be recombined (in modern systems the point illumination is moved using mirrors or pinhole wheels as opposed to the original system in which the sample was moved). Not only did confocal microscopy offer an improvement in resolution (the highest lateral resolution achievable has been calculated

to be as small as 50 nm),<sup>9</sup> but the ability to focus light at a particular height within the specimen. With the correct software it has become possible to render a 3D representation of the sample (known as a z stack).

Armed with the knowledge that using a smaller wavelength gave images with a higher resolution, electron microscopes (EM) were created. Instead of using light waves, these microscopes use electron waves whose wavelengths are substantially smaller to the point where angstrom (atomic) resolution can be attained.<sup>10</sup> However, since wavelength is inversely proportional to energy, specimens require specific preventative measures including coating the sample in a conducting metal that protects the sample from high energy electron waves and provides a means of neutralising any charge that builds up during the imaging process. Images of live samples cannot be taken using EM which led to the need for super-resolution optical microscopy techniques. As well as confocal microscopy, many other efforts have been made in optical and fluorescence microscopy to circumvent the resolution limit, leading to the emergence of several other high-resolution microscopy techniques.

## **1.2 High-resolution fluorescence microscopy**

Optical microscopy is favoured for imaging live samples due to its non-invasive nature, although, when using light of lower wavelength, high energy photons can be damaging to living specimens. This problem was partially solved by employing the phenomenon of two-photon absorption which was first observed in  $\text{CaF}_2:\text{Eu}^{2+}$  crystals by Wolfgang Kaiser in 1961.<sup>11</sup> Two-photon spectroscopy is based on the concept that two photons with twice the wavelength (thus half the energy) can be absorbed simultaneously to excite a fluorophore that would ordinarily require high energy radiation. The technique is sometimes preferred to confocal microscopy due to deeper tissue penetration (millimetre scale) and reduced phototoxicity.<sup>12</sup>

Two-photon microscopy can still be used to take sectioned images through the  $z$ -axis due to the shape of the PSF which is long in the  $x$ - $y$  plane (compared to single photon excitation where the PSF is long in the  $z$ -axis for light of the same wavelength), and focussed light is still scanned across the sample. The change in the shape of the PSF is because the excitation density in single photon absorption is proportional to the local intensity, whereas the density of two-photon excitation is proportional to the square of the intensity.<sup>13</sup> Because the PSF is shallow in  $z$ , the axial resolution is improved, and thinner optical sections can be taken. The technique offers a similar lateral resolution to confocal microscopy. Pinhole apertures are also unnecessary since excitation is restricted to very small focal volumes, thus out-of-focus objects are easily rejected.<sup>14</sup> The absence of the pinhole aperture also means that scattered photons can contribute towards image acquisition leading to a less noisy image. Fluorophores used for two-photon microscopy often have a donor-acceptor-donor type structure.

The primary disadvantage of this technique is that the likelihood of a fluorophore absorbing two photons almost simultaneously is very low, thus very intense, pulsed laser light is required. Pulsed lasers are substantially more expensive than the continuous wave (CW) lasers used for single photon excitation. The two-photon absorption spectrum for a given fluorophore can vary significantly from its one-photon counterpart meaning that many fluorophores may not be suitable for use in the technique. Two-photon microscopy finds its forte when imaging deep samples due to greater scattering (such as tissues).

Another technique which boasts superior sample sectioning in the  $z$ -axis is light sheet fluorescence microscopy (LSFM, or single plane illumination microscopy, SPIM). These systems offer lateral resolution on par with epifluorescence but offers  $z$ -sectioning capabilities similar to that of confocal microscopy.<sup>15</sup> LSFM is particularly useful for the examination of large samples (such as small animals, e.g. zebrafish, or individual organs



within a larger animals). Only a thin slice (as thin as a few hundred nanometres) of a sample is illuminated at a time perpendicular to the direction of observation (Figure 1.3).

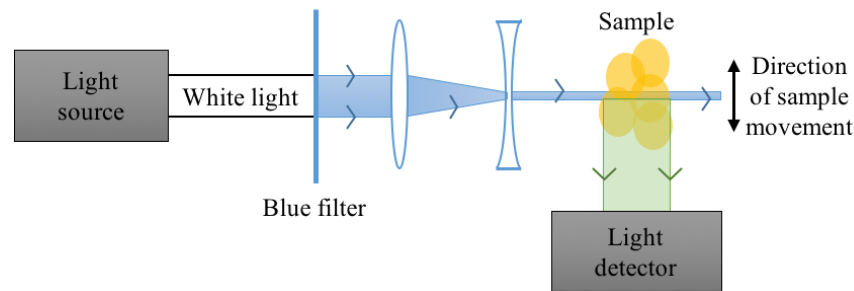


*Figure 1.3 – The simplified workings of a light sheet microscope drawn from above. White light is passed through a filter (in this case blue, alternately a coloured laser is used) before being focussed into a thin sheet of light. A labelled sample is moved back and forth through the light sheet and emitted light (in this case green) is collected perpendicular to the light sheet.*

Since only the section currently being observed is illuminated LSFM can go some way to reducing the photostress induced on living samples. This also means that there are fewer noisy background signals leading to images with higher contrast compared to confocal microscopy. Additionally, since focussed light does not have to be scanned over the entire specimen, images can be acquired up to 1000 times quicker than point-scanning methods. LSFM has recently been used in conjunction with two-photon microscopy in order to reduce further the levels of photoinduced stress on brain samples.<sup>16,17</sup> LSFM has been employed in combination with many other techniques including the super-resolution technique known as simulated emission depletion (STED).

### **1.3 Super-resolution fluorescence microscopy**

The term super-resolution has been used in microscopy to describe techniques that can achieve spatial resolution that is not limited by the diffraction of light.<sup>18</sup> Where the imaging systems described above are limited by the size of the PSF (two points closer than the full width at half maximum (FWHM) of the PSF are unresolvable because their

images have substantial overlap), the following methods are limited by the instruments or fluorophores used.

Though still reliant on the size of the PSF, stimulated emission depletion uses a secondary PSF to selectively deactivate fluorophores in order to minimise the area of illumination at the focal point and enhance the achievable resolution.<sup>19</sup> The deactivation of fluorescence occurs as a result of the non-linear response of fluorophores after irradiation with light of different wavelengths. STED beams interrupt normal fluorescence by forcing excited states to relax into a high vibrational level of the ground state resulting in the release of a lower energy, longer wavelength photon. Since these photons have different characteristics to those of the photons released by normal fluorescence they can be filtered and ignored.

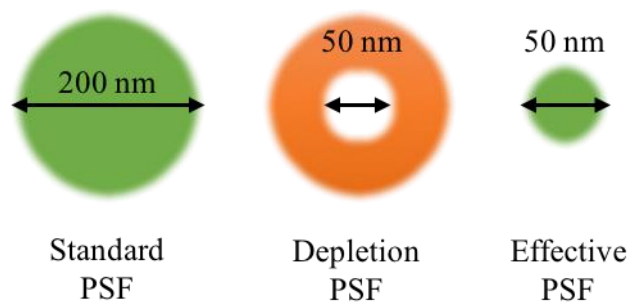


*Figure 1.4 – The standard PSF of an excitation spot is reduced in size by a donut shaped PSF of a depletion STED beam to give a smaller effective excitation PSF.*

The focal area can be engineered by altering the properties of the PSF of the STED beam. The most common shapes for these point spread functions are two-dimensional donuts generated by circular polarisation of the depletion laser combined with a helical phase ramp (Figure 1.4).<sup>20</sup> The resultant effective PSF typically has a diameter of approximately 50 nm, though lateral resolutions as high as 2.4 nm have been reported with the ability to localise emitting fluorophores with sub-angstrom accuracy.<sup>21</sup>

The main limitations of STED are the complex instrumentation required to create the depletion beam and the photophysical requirements of dyes for use in STED (which must be able to exhibit stimulated emission non-linearly and be photostable under the high laser powers). As yet there appear to be no common structural features to the dyes chosen for STED microscopy and, as with many super-resolution techniques, dyes that are fit for purpose appear to have been randomly cherry picked *via* trial and error. In terms of the photophysical properties, good STED dyes are characterised by high quantum yields, emission spectra that overlap with the STED wavelength, high photostability, long fluorescence lifetimes (of at least 0.8 ns), and a low cross-section for multiphoton absorption or for absorption by the excited states.<sup>22</sup> A search of the current literature gives no results on how to tune dyes for stimulated emission depletion microscopy.

As mentioned previously, STED microscopy has been combined with light sheet microscopy to give STED-SPIM. The combined technique, which was first described in 2011 by Harms and co-workers, initially allowed for an improvement of the axial resolution of up to 60%, lateral resolution improvements of up to 40% (both with respect to the resolutions achievable using epifluorescence), and an imaging depth of over 100  $\mu\text{m}$ .<sup>23</sup> A STED depletion beam makes the original light sheet thinner by sandwiching it with the higher energy radiation.

The resolutions achievable using STED are governed by the size of the ‘hole’ in the middle of the STED depletion PSF, which in turn is controlled by the intensity of the light being used.<sup>24</sup> A high laser power will decrease the size of the ‘hole’ but may induce damage to the sample.

Another technique unaffected by the diffraction limit is near-field scanning optical microscopy (NSOM). When light leaves an aperture there is a distance much smaller than the wavelength of light used in which light does not diffract (Figure 1.5). Placing a sample

in the near-field means the diffraction of light no longer limits the resolution of the image obtained, but only the dimensions of the aperture.<sup>25</sup> Typically, the length of the near-field as measured from the end of the aperture is less than fifty times smaller than the wavelength of the light used. Images are obtained by scanning the aperture closely over the surface of a specimen.

Originally used to acquire images of lithographically etched surfaces with spatial resolutions as small as 12 nm (using light with a wavelength of 514 nm),<sup>26</sup> the technique was intended for use in solid-state physics for mask inspection and repair of nanolithographically patterned structures. Though it was suggested that NSOM could be used to study living cells in their native environments, it is difficult to conduct in a non-invasive manner due to the fact that the aperture itself must scan over the sample surface which may accidentally scrape the sample, as opposed to previously discussed scanning microscopy methods which scan light beams.<sup>27</sup> Imaging beyond the surface of live specimens is also not possible using NSOM, thus the development of other wide-field techniques was prioritised.

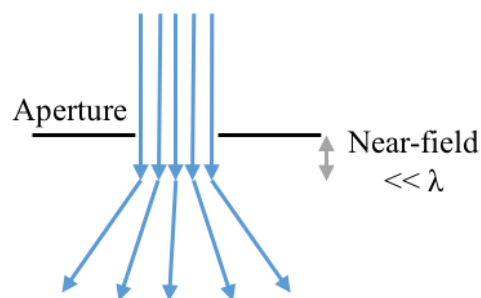


*Figure 1.5 – The small distance after light leaves an aperture in which light does not diffract is known as the near-field and has a distance much smaller than the wavelength used.*

#### **1.4 Single molecule detection and localisation microscopy**

Where the above discussed methods can be described as being ensemble fluorescence techniques that detect multiple fluorophores in small areas, single molecule localisation

involves the detection of individual fluorophores in a wide area and has helped further push the limits of resolution beyond Abbe's limit. Tracking of individual molecules was first reported in 1976 by Hirschfeld who observed single antibodies tagged with FITC (fluorescein isothiocyanate) using an epifluorescent microscope.<sup>28</sup> By tagging FITC to a polymer (polyethyleneimine) it became possible to label and track the single molecules of the antibody  $\gamma$ -globulin.

In 1989 single molecules were detected in condensed phases (solids) at liquid helium temperatures by Moerner *et al.*<sup>29</sup> The absorption spectra of single molecules of pentacene were detected in host crystals of *p*-terphenyl. Four years later NSOM was used to detect single carbocyanine dye molecules sparsely dispersed throughout a thin film of polymethylmethacrylate by Betzig and coworkers.<sup>30</sup> This method allowed for the pinpoint localisation with an accuracy 50 times smaller than the wavelength used, and the measurement of five of the six degrees of freedom for each molecule which in turn enabled the exact determination of molecular orientation.

Up to this point detecting individual molecules required them to be thinly dispersed in a medium at a distance that surpassed the diffraction limit. This all changed when, in 1997, Moerner reported the first observation of on/off fluorescence switching (photoblinking) of single molecules of green fluorescent protein (GFP) suspended in aerated aqueous polymer gels at room temperature.<sup>31</sup> It was reported that each molecule produced several seconds of fluorescence then several seconds without emission, followed by resumption of emission and repeating the cycle over the course of many minutes. This study not only reported the first instance of blinking by fluorescent molecules, but also demonstrated that once GFP had gone into a long-lasting dark state its fluorescence activity could be reactivated by illumination with a shorter wavelength laser correlating to a weaker absorption band (photoswitching).

After discovering more fluorophores that were capable of photoswitching and photoblinking, many researchers attempted to exploit the phenomenon in order to overcome the diffraction limit. In 2006, three journal articles detailing methods that could stochastically and sequentially record photoblinking fluorophores in order to determine their precise locations and reconstruct a high resolution image were published. The three methods were named photoactivated localisation microscopy (PALM),<sup>32</sup> fluorescence photoactivated localisation microscopy (FPALM),<sup>33</sup> and stochastic optical reconstruction microscopy (STORM).<sup>34</sup> These methods could record images with lateral resolutions down to 2 nm in fixed samples,<sup>32</sup> and have since been used to track the expression and movement of proteins and other substrates in live cells.<sup>35</sup>

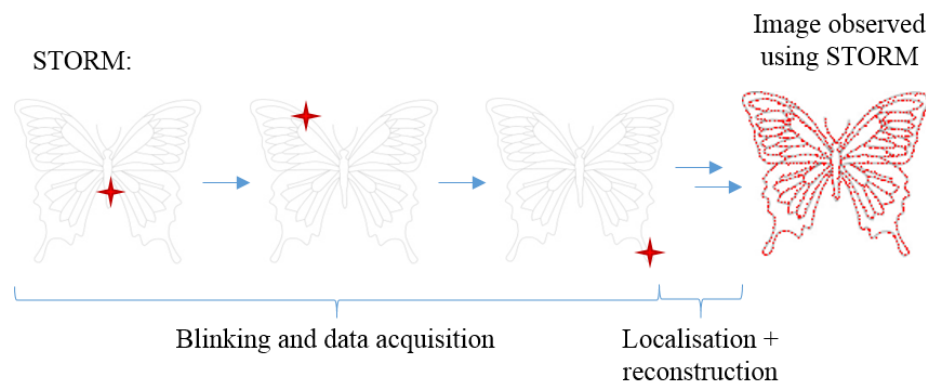


*Figure 1.6 – A cartoon showing how STORM works. Single molecules exhibit photoblinking and are captured in a series of frames. Frames are analysed by a program that reconstructs blinks to give a high-resolution image. Butterfly outline found: <https://goo.gl/SzXAVT> (accessed 02/2017).*

Though each method varies slightly from the other, all three rely on an activation laser applied at a low power to trigger photoswitching. The low laser power ensures that only a subset of fluorophores become fluorescent and each fluorophore in the sample exists in either a fluorescent ‘on’ state, or a non-emissive ‘off’ state.<sup>36</sup> Photoswitching is recorded over time (using pulsed lasers or FRET pairs) and in each frame individual molecules are pinpointed and localised based on the assumption that the intensity profile of the PSF for

each molecule fits to a Gaussian bell curve.<sup>34</sup> A final image is then reconstructed by plotting each molecule relative to each other in space (Figure 1.6). The primary difference between the three methods at the time of their publication was the nature of the fluorophore and microscope used in each case. PALM and FPALM used photoswitchable fluorescent proteins, STORM used photoswitchable organic dyes; and PALM and STORM images were taken on a total internal reflection fluorescence microscope (TIRF microscope) whereas FPALM images were captured using a confocal microscope.

The fundamental principle of the three methods is that the fluorescent ‘on-state’ of each fluorophore must lead to the consecutive emission of sufficient photons to enable visualisation and precise localisation before it enters its non-emissive ‘off-state’ or becomes deactivated by photobleaching. Conversely, however, the molecule must also not continue emitting for such a long time that its fluorescence interferes with the emission of surrounding molecules as they enter their fluorescent state.<sup>37</sup> If these conditions are met for a given fluorophore, the probability of one blinking molecule being close (closer than Abbe’s diffraction limit) to another simultaneously blinking molecule is low and it is possible to identify individual molecules in each frame. As such, the three techniques can be grouped together as single molecule localisation microscopy (SMLM) techniques.

As SMLM techniques have evolved they have been used to study biological systems in much greater detail. Methodologies that allow for the use of optically orthogonal fluorophores that absorb and emit at different wavelengths have been used to uncover the previously obscured details of morphological dynamics of mitochondrial fusion and fission as well as endoplasmic reticulum (ER) remodelling. Time-lapse STORM images revealed thin extended tubular structures connecting neighbouring mitochondria both prior to fusion and after fission.<sup>38</sup> The tubes were speculated to be necessary for bringing

mitochondria into close proximity before fusion and pushing the organelles away from one another after fission. Studies indicate that the tubes are ER tubules composed of a dynamin-family protein without which mitochondrial division is impossible, and whose use was unknown prior to the observation of the tubes.

Collaborators in Sheffield are currently working towards the elucidation of the cell wall elongation mode in bacteria using STORM. Foster and co-workers used the technique to closely inspect the cell walls of Gram-negative bacteria *E. coli* and *C. crescentus* by specifically labelling the peptidoglycan network of the cell wall and discovered that in these cells new peptidoglycan material is inserted at distinct *foci* along the cylindrical portion of the cell, contrary to previous reports that suggested elongation machinery moves about the cell in a cylindrical manner.<sup>39</sup> Focus has now shifted to Gram-positive bacteria and the latest results show novel features in cell wall architecture during division. Moerner *et al.* used SMLM to track single proteins during bacterial division.<sup>40</sup> The rate of DNA base excision repair rate was measured by tracking DNA polymerase I and DNA ligase in live *E. coli* cells, finding that on average it took two seconds for the pair of enzymes to carry out repair operations.

## **1.5 STORM**

Though STORM has been used since its conception to make advancements in the microbiological sciences there are still many unanswered questions surrounding the technique regarding all aspects from the best way to collect data to fluorophore selection. Although the requirements stated for fluorophore suitability seem trivial (fluorescent phase long enough to collect sufficient photons but not so long that neighbouring molecules will be simultaneously fluorescent) it can be difficult to select molecules with the desired qualities. Indeed, the best fluorophores were cherry-picked from a suite of existing commercially available dyes, or their favourable properties were discovered by



accident. It is still difficult to predict whether a dye will present such properties, and as such a range of variations of STORM have been developed. The hardware used for capturing images has remained roughly unchanged, with most researchers opting to use DIY systems or repurposing old microscopes instead of purchasing expensive commercial systems. A researcher in the Cadby group uses a children's play microscope to acquire their images, proving that with proper software and labelling equipment STORM is a highly accessible technique.

Problems arise when neighbouring fluorophores (closer than the diffraction limit) exist in their 'on' state simultaneously as it then becomes impossible to distinguish between their PSFs, lowering the localisation precision. The result is a misleading average position between the two (Figure 1.7).<sup>41</sup> In the absence of 'perfect' fluorophores it has become necessary to develop methods that allow for a compromise between high density labelling (increased likelihood of overlapping PSFs) and long acquisition periods (may damage specimen or experience sample drift) to give the best resolution. As well as this, it has been essential to develop software capable of distinguishing between signal and noise, that are also capable of correcting for drift in the position of the sample over time and many approaches have been taken in order to do so.

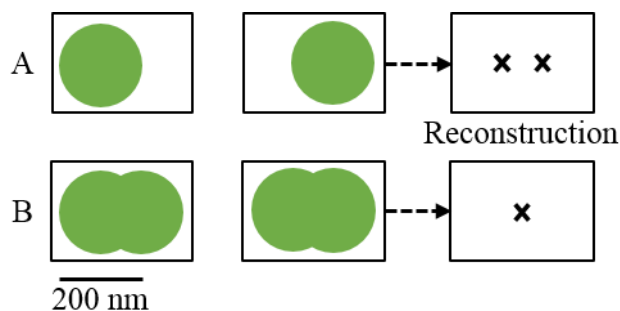


*Figure 1.7 – Cartoon illustrating the importance of fluorescence duration. A) Neighbouring molecules exhibit fluorescence at separate times and can be resolved by software as two distinct diffraction limited points. B) Neighbouring molecules exhibit fluorescence simultaneously. They cannot be resolved and software reconstructs them as one molecule.*

### 1.5.1 dSTORM and data analysis

The first major advancement in SMLM imaging techniques came in 2008 when, again, three independently published journal articles gave details of reversible photobleaching microscopy (RPM),<sup>42</sup> ground state depletion microscopy followed by individual molecule return (GSDIM),<sup>43</sup> and direct STORM (dSTORM – the now generally accepted name for the three analogous methods, however, developments in PALM, STORM and dSTORM have led to the three terms being used interchangeably in recent years).<sup>44</sup>

Where STORM and PALM at first relied on ‘manually’ photoswitchable dyes (e.g. the cy3-cy5 FRET pair that required pulsed lasers at two wavelengths) and fluorescent proteins, dSTORM exploits the phenomenon of photoblinking. Appropriate dye molecules are subjected to high intensity laser light which forces the majority of the dye molecules into their non-fluorescent ‘dark’ state (e.g. a semi-stable triplet state). At this point individual molecules stochastically return to the ground state (e.g. *via* molecular vibration) and are able to fluoresce for a short time before returning to the ‘dark’ state. The advantages over the other methods of the time were that fluorophore choice became much less limited as many commercial fluorophores were capable of photoblinking with high-power laser irradiation, and images could be taken in standard aqueous or glycerol-based buffers as opposed to the special immersion or embedding buffers used for PALM and STORM, opening the door to the possibilities of live-cell imaging.

To enhance the photoblinking ability different combinations of additives were used when imaging. To stabilise the ‘dark’ state, it was necessary to remove molecular oxygen from buffered solutions. Though this could be achieved by bubbling oxygen-free gases through solutions, enzymatic consumption was preferred and a cocktail of glucose oxidase and catalase with  $\beta$ -D-glucose as a substrate (GLOX buffer) has become the most commonly used.<sup>45</sup> This absence of oxygen increased the stability of triplet states leading to very short

photoblinking events and prolonged dark states, thus triplet quenchers and reducing agents were added to lengthen the ‘on’ state. Thiols such as  $\beta$ -mercaptoethylamine (MEA) are frequently used as the reductant.<sup>46</sup>

With imaging conditions established, researchers set out to write algorithms to analyse their data. Many teams across the globe attempted to write code that could avoid sacrificing precision, fluorophore density in the sample, or imaging and reconstruction speed. Many software packages emerged, including Auto-Bayes which uses Bayesian statistics to accurately discriminate between signal and noise resulting in vastly more accurate images,<sup>47</sup> and QuickPALM which localises particles based on the centre of mass of a point spread function and revolutionised the field by reducing image reconstruction time from hours or days to almost real-time (though this came with a small reduction in resolution).<sup>48</sup>

With a plethora of software to choose from it became confusing for researchers to choose the appropriate data analysis tools, so in 2015 a comprehensive comparative review was published testing each algorithm by using it to reconstruct ‘synthetic data’ and scoring each package in various categories including accuracy, precision, time taken and signal to noise ratio (SNR).<sup>49</sup> The software that performed the best overall was ThunderSTORM,<sup>50</sup> a plugin for the popular open-access image analysis programme ImageJ/Fiji.<sup>51,52</sup> Users of ThunderSTORM are able to customise the programme in multiple categories such as the way in which signal is filtered from noise, and how Gaussian curves are fit to acquired data until the best results are achieved. The developers also included a ‘preview’ function so that whole image stacks did not have to be reconstructed before modifying the settings. As such, ThunderSTORM has become one of the most popular and commonly used analysis packages and will be used throughout this work for data analysis.

### 1.5.2 3D STORM

Though lateral resolutions had been improved to beat the diffraction limit tenfold, improvements in axial resolution were lacking, and SMLM images could only be reconstructed in two dimensions for the two years after the development of the technique. In 2008 SMLM imaging was combined with optical astigmatism to produce the first super-resolution image to be reconstructed in three dimensions.<sup>53</sup> This allowed axial resolutions of up to 50 nm compared to confocal or light-sheet microscopy whose diffraction limited axial resolutions are generally between 500-800 nm owing to the shapes of the PSFs used, again derived by Abbe.<sup>5</sup>

$$\text{Resolution (z)} = 2\lambda / [n \cdot \sin(\theta)]^2 \quad \text{Equation 1.2}$$

$\lambda$  = wavelength,  $n$  = refractive index,  $\theta$  = aperture angle

Optical astigmatism arises from the introduction of a cylindrical lens that creates separate paths for the  $x$  and  $y$  components of the PSF. As such, the PSF appears circular when in the plane of focus but is elliptical when above or below this axial position (Figure 1.8). As such, analysis programmes can then interpret the shape of the PSF and the degree of distortion to reconstruct the image by localising points in all three dimensions.

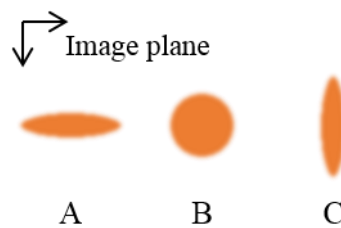


Figure 1.8 – Representations of how a point spread function may look A) below, B) in, or C) above the focal plane with the use of optical astigmatism.

Other attempts have been made in order to improve the axial resolution in SMLM techniques, however the value of 50 nm was not beaten for several years until astigmatism

was combined with a dual-objective system by Xu and co-workers.<sup>54</sup> In this system the light emitted from above and below the sample was collected, recording lateral resolutions of 10 nm and axial resolutions of 20 nm. This improvement was accompanied by increased photon collection and reduced noise.

Double helix point spread functions (DH-PSF) are an alternative to astigmatism in improving the axial resolution and reportedly gave axial resolutions of between 10 – 20 nm.<sup>55</sup> This method involves a spatial light modulator that reshapes the PSF of emitted light to give it two lobes (Figure 1.9). While resolution is on par with astigmatism the  $z$ -range is doubled to approximately 2  $\mu\text{m}$  so its use is advantageous with taller structures.

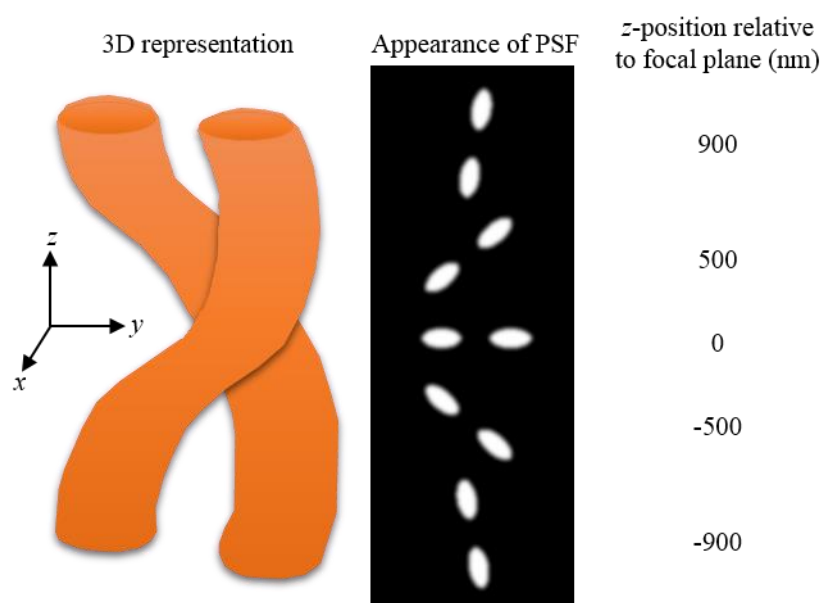


Figure 1.9 – A cartoon representation of a double helix PSF and how it would look under the microscope at various planes within the sample.

### 1.5.3 Commonly used fluorophores

As previously mentioned, the properties possessed by dyes that can be used in STORM are specific and restrictive. As such, only a select few dyes can be used for SMLM imaging. While the technique was in its infancy, dyes were picked at random from the

pool of commercially available fluorophores, and while this gave good results in some cases, if the dye was not appropriate, the results often went unpublished leading to the potential for these errors to be replicated. In order to abate this issue, articles in recent years have contained detailed studies of the photophysical properties of many dyes including which fluorophores are best and, arguably more importantly, worst suited for SMLM.<sup>56,57</sup> These studies primarily focus on commercially available dyes from the Alexa Fluor or Atto brand lines since they are well known and span the whole visible spectrum. These fluorescent probes generally take the form of a coumarin, rhodamine or cyanine structure (Figure 1.10), emitting at the lower, middle, or upper section of the visible spectrum respectively.

In the original STORM paper, two cyanine dyes were used in conjunction with each other.<sup>34</sup> Cyanines 3 and 5 (Cy 3 and 5, named for the number of carbon atoms in the polymethine chain connecting the two heteroaromatic systems, Figure 1.10C,  $n = 1$  and  $2$ , respectively) were used for a long time as a photoswitching pair by utilising light of different wavelengths. Red light can be used to transfer Cy 5 to its dark ‘off’ state before green light is used to reliably bring the molecule back to its fluorescent ‘on’ state, but only when in close proximity to a Cy 3 molecule *via* a FRET-like mechanism.<sup>58</sup>

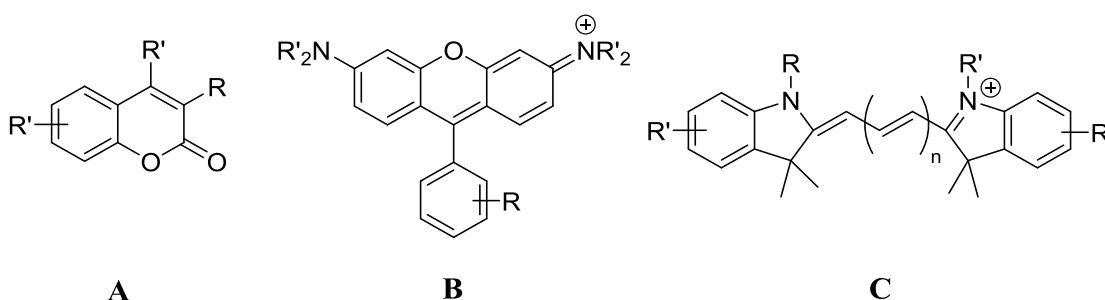


Figure 1.10 – General structures of dyes commonly used in SMLM.  $R$  denotes a position suitable for functionalisation/tethering,  $R'$  denotes positions suitable for dye modification. A) Coumarin, B) Rhodamine, C) Cyanine, where  $n = 1, 2, 3$  for Cy 3, 5 and 7, respectively.

To date, Cy 5 and its derivatives (e.g. Alexa Fluor 647 which has the same base structure as Cy 5 with solubilising sulfonate moieties bound to the aromatic rings) have been one of, if not the best dye for capturing SMLM images, possessing superior qualities such as a high quantum yield, photostability, and ease of inducing photoswitching or blinking.<sup>59,60</sup>

As well as the classes of small-molecule dyes previously mentioned, many SMLM images are taken using fluorescent proteins (FPs). FPs have long been used for epifluorescent imaging since, similarly to molecular dyes, they can be conjugated *via* antibodies for specific targets and, unlike molecular dyes, are natural structures so either cellular uptake is facilitated by membrane proteins or they can be made by the cell *in situ* by the introduction of an appropriate plasmid.<sup>61</sup> Fluorescent proteins have been discovered or modified to give access to emissions wavelengths across the visible spectrum, and cellular tolerance makes the use of FPs more amenable for real-time imaging and organelle tracking. The disadvantage of FPs when capturing SMLM images are their size. Fluorescent proteins are typically approximately 4 nm across and are linked to the protein of interest *via* antibody conjugation, which is usually up to 5 nm in length. As such, the imaged structure can be erroneous by the vector sum of these values in any direction which can give errors in dimensionality studies.<sup>62,63</sup>

#### **1.5.4 Theories on the blinking mechanism**

Many theories have been proposed as to how photoblinking occurs, and these can vary depending on the class of fluorophore being used. In general, theories tend to focus on electronic rather than chemical transitions, though since Cy 5 is the most successful dye used in super-resolution microscopy, many more theories have been developed about its photoswitching mechanism.

For many years it was believed that the ‘dark state’ was an electronic effect arising from intersystem crossing (ISC) to a stable or semi-stable triplet state, and this state was

examined in Cy 5 by Dempster *et al.* as far back as 1971.<sup>36</sup> This supposed triplet state became vastly more stable in the presence of iodide due to heavy atom induced spin coupling. The authors did, however, discover another dark state for pentamethine cyanine that was recognised to be a *trans-cis* isomerisation whose rate of transition was significantly hindered by increased solvent viscosity.

The proposed triplet state of Cy 5 could be accessed *via* irradiation with red light, and the rate of this transition was not impeded by solvent viscosity.<sup>58</sup> The lifetime of this triplet state has been reported to be in the order of hours in the absence of known triplet quenchers such as oxygen. This mystified researchers, since the average triplet state lifetime was in the order of hundreds of milliseconds, and gave rise to the theory that perhaps another more stable non-emissive electronic state exists that can be reached *via* ISC to a triplet state (Figure 1.11).

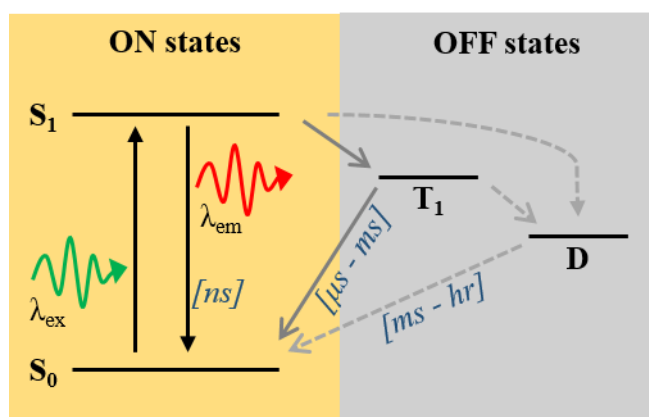


Figure 1.11 – A simplified Jablonski diagram showing possible electronic transitions in STORM-active fluorophores. For simplicity vibrational states are omitted. Approximate relaxation timescales denoted in blue italic text. Adapted from Nahidiazar *et al.*<sup>64</sup>

From the ground state (S<sub>0</sub>), fluorophores can be excited *via* absorption of light (λ<sub>ex</sub>) to the excited singlet state (S<sub>1</sub>). From there the electron relaxes to the ground state *via* fluorescence (λ<sub>em</sub>) or undergoes ISC to a triplet state (T<sub>1</sub>). The electron then either relaxes



to  $S_0$  or to another dark state (D). Direct transition from excited singlet states to non-triplet dark states has been reported for some dye molecules under REDOX conditions.<sup>65</sup>

While the ease of transition to, and stability of the electronic dark state appears to be intrinsic to specific molecules, it was found that minor chemical alterations to dye structure can tailor these properties in cyanine dyes.<sup>66,67</sup> By increasing the barrier to rotation for *trans-cis* isomerisation by adding, e.g. long alkyl chains to the *N*-alkyl substituent (R, Figure 1.10C, p20) or pendant groups such as halogens to the *meso*-carbon (the carbon atom in the middle of the polymethine chain in the symmetrical molecule) the lifetime of the dark state was modified. Another proposed mechanism for the blinking mechanism in cyanine dyes is the reversible chemical binding of thiols in the SMLM buffer solution (e.g. MEA) to the alkenes in the polymethine chain in a reversible thiol-ene reaction.<sup>68</sup> The formation of the carbon-sulfur bond breaks the conjugation in the dye molecule and fluorescence of the reduced species is quenched.

In separate studies using rhodamine dyes, another type of dark state was observed to be a radical-ion, confirmed using electron spin resonance (ESR).<sup>69</sup> A light-induced signal appeared in the ESR spectrum at the resonant field of a free electron, facilitated by the reductants or thiols used in SMLM buffers.

Since SMLM techniques were introduced they have become increasingly popular and even resulted in a Nobel Prize for those who contributed to its development. As such it has become important to determine which qualities a dye must possess in order for it to exhibit photoblinking on a useful timescale for SMLM imaging. Furthermore, it would be useful to probe the photophysical properties of dyes in order to determine why some dyes are able to blink and some are not such that bespoke dye molecules could be rationally designed for SMLM, rather than cherry-picking from commercially available dyes as many do today.

## 1.6 Dye modification

Chemical modification of dyes in order to tune their photophysical properties has been practiced for a number of years using a variety of different classes of dyes. Atomic substitution was examined recently with a series of group 14 rhodamine dyes to introduce a greater range of dyes able to absorb and emit light in the near-infrared region of the visible spectrum – particularly useful wavelengths for avoiding cellular damage when imaging living specimens.<sup>70</sup> By substituting the oxygen at position 10 of the pyronine moiety (Figure 1.10B, p20) with silicon, germanium, or tin the absorption maximum was increased from 549 nm to over 620 nm.

In general, the substitution of heteroatoms in dye molecules gives similar trends in the changes observed in photophysical properties. There is a bathochromic (red) shift in the absorption and emission wavelengths when heavier atoms are incorporated due to a decreased HOMO-LUMO energy gap.<sup>71</sup> This decrease in energy difference is a reflection of oxidation potentials becoming more negative and reduction potentials becoming more positive. This is usually also accompanied by a decrease in molar extinction coefficient ( $\epsilon$ ), quantum yield ( $\phi$ ), and solubility.<sup>72–75</sup> In a study investigating atomic substitution in D-luciferin, these effects were attributed to the polar effect with heavier, less electronegative atoms less able to polarise the aromatic system and having an effect on the aromaticity of the heteroaromatic system.<sup>73</sup>

The effects of the inclusion of heavier atoms on the aromaticity in heteroaromatic compounds was documented in a study by Bird in 1992.<sup>76</sup> Substitution of oxygen for sulfur or selenium into 2,1,3-chalcogenodiazoles (Figure 1.12) has been shown both theoretically and experimentally to increase the degree of aromaticity.<sup>76–79</sup> Bird uses his unified aromaticity index ( $I_A$ ) to assign well-defined rankings of aromaticity and estimate the resonance energy of heteroaromatic compounds (stability afforded to compounds as

a result of aromatic stabilisation). The sulfur containing compound is almost twice as aromatic than the oxygen and selenium containing counterparts on Bird's scale, which takes into account the heats of formation, bond lengths and chemical shift in the  $^1\text{H}$  NMR spectrum. This is rationalised by the fact that, although sulfur has larger orbitals that can give a good overlap with the other atoms in the aromatic cycle, it is much less electronegative than oxygen, so electrons are more freely able to be delocalised around the system. This effect is negated in 2,1,3-selenadiazole since its much larger atomic radius means that its orbitals are now too large to give sufficient overlap with the neighbouring nitrogen atoms, making the aromaticity of the selenium containing molecule on par with the oxygenated derivative ( $I_A = 53, 104, 58$  for  $X = \text{O}, \text{S}, \text{Se}$ , respectively).<sup>76</sup>



Figure 1.12 – The general structure of the benzodiazoles analysed in Bird's study.  $X = \text{O}, \text{S}, \text{Se}$ .

In the aforementioned study on cyanine 5, it was found that the most profound effect of adding long *N*-alkyl chains or *meso*-halogenation was on a quality known as modulation depth – a measure of how efficiently a dark state can be populated and depopulated. In the case of Cy 5, dyes with high modulation depth quickly feed into long-lived dark states which can rapidly be depopulated by a second laser.<sup>67</sup> Modulation depth increased with longer *N*-alkyl chains and decreased with the increasing atomic mass of the halogen used with *meso*-halogenation. Longer alkyl chains appeared to slow *trans-cis* isomerism decreasing the rate at which the molecules switched between the light and dark states, whereas larger halogens seemed to shorten “on” and “off” lifetimes. The introduction of the *meso*-halogen in the dye may have affected the balance of s- and p-orbital character

in the molecular orbital. Reducing the efficiency of p-orbital overlap would make the ground state less stable.

This then begs the question of what else could be done to modify the ratio of s- and p-orbital character of the aromatic system of cyanine dyes. To date, this is an area in which little exploration has been done. Harriman and co-workers have investigated the effects of torsion in bimetallic molecular wire systems,<sup>80</sup> and it was found that the rate at which a triplet state was transferred was hindered by using linkers to hold ligands at increasing dihedral angles to each other. An 80-fold decrease in the rate of electron transfer between ligands was recorded as the dihedral angle between the ligands was increased from 0° to 90°. These findings suggest that in cyanine dyes, adding torsion and increasing the dihedral angle between the two heteroaromatic moieties may affect the degree of conjugation and have an effect on the photophysical properties.

## 1.7 Project background

The existing literature on atomic substitution prompted work within the Jones group in which two dye molecules with valence isoelectronic substitutions (i.e. using elements in the same group of the periodic table) exhibited different properties under STORM conditions. The unpublished work compared two nitrobenzochalcogenadiazole dyes as contrast agents when imaging the cell wall in dividing *S. aureus* cells using epifluorescence microscopy, where 4-nitrobenzoxadiazole-D-alanine conjugate (NADA) contained an oxygen at position 2 of the heteroaromatic ring, and 4-nitrobenzothiadiazole-D-alanine conjugate (SADA) contained a sulfur atom in the same position (Figure 1.13). Images of the labelled cells were taken using a self-built STORM microscope with SMLM buffers and a dramatic difference in dye properties was observed. When using the oxygen containing NADA fluorescence occurred as expected, however when using the sulfur containing SADA, photoblinking was observed.

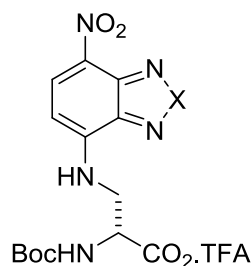


Figure 1.13 – The structure of 4-nitrobenzochalcogenadiazole-D-alanine conjugates.  $X = O, S$  for NADA, SADA, respectively.

This difference in behaviour led to the prediction that increasing the size of the heteroatom in the nitrobenzochalcogenadiazole system would lead to increased blinking activity due to the changes in the degree of aromaticity. Unfortunately, when a control sample of unlabelled cells was examined, the unlabelled cells also exhibited photoblinking at the observed wavelength due to cellular autofluorescence (fluorescence of cellular components). As such, an alternate means of studying the dyes under SMLM conditions was required.

## 1.8 Aims

The overall aim of this project is to synthesise and analyse a series of small organic fluorophores and assess the qualities that make them SMLM-compatible (or SMLM-incompatible as the case may be). It is hoped that probing these qualities will, in the future, enable the bespoke design of dyes for SMLM with favourable properties.

Dyes will be analysed in solution, but to exhibit photoblinking a dye must be mounted onto a solid (e.g. a cellular structure). Due to cellular autofluorescence in *S. aureus* at the wavelength at which the benzodiazole dyes absorb, in order to investigate this set of dyes it is necessary to find an alternative solid support and avoid using biological structures such as cell walls. Studying dyes in the absence of biological systems also ensures that the observed properties are solely a result of dye modification and negates any effect from

the influence of the complex environment within a cell or other organism. As yet, there is no literature precedent for imaging non-biological structures using SMLM techniques.

The method of dye modification that will be examined is atomic substitution. Atomic substitution will be examined in a series of nitrobenzochalcogenozole dyes, adding a selenium containing derivative to see whether or not any trends exist in the series. The synthesis and analysis of various rhodamine dyes will also be undertaken to compare the effect of including different heteroatoms in the context of SMLM imaging.

In order to ligate the dye molecules to a surface, a suitable material must be chosen. The most common material for surface modification is gold, but since gold nanoparticles have their own spectral properties their use may lead to complications in taking measurements.<sup>81,82</sup> As well as this, the thiols used in SMLM buffers could displace any dyes ligated to the gold surface. The next most convenient material for chemical ligation would be silica based (e.g. glass slides or silica nanoparticles) since they have no optical absorption or emission properties.<sup>83</sup> Since silica nanoparticles can be made spherical, they are an obvious choice in their ability to mimic *S. aureus* cells. They are also easy to synthesise and functionalise with appropriately ligated molecules.

Covalent attachment to silica surfaces is well established and exploits the chemical stability of oxygen-silica single bonds.<sup>84,85</sup> (3-Aminopropyl)triethoxy silane (APTES) is commonly used as a linker due to its dual functionality. The primary amine terminus has useful reactive properties and can be used in a range of reactions to add dye molecules. Other reports in the literature have analysed dye molecules suspended in polymer matrices in order to study blink rate and frequency in the absence of biological systems.<sup>86</sup> It would be prudent to replicate these experiments on the dyes synthesised over the course of this project. This method also allows for the analysis of some molecules without having to add a tether for functionalisation, easing the degree of synthesis required.

## 2 Benzochalcogenadiazole synthesis and analysis

In this work a series of benzochalcogenazole dyes were synthesised incorporating the group 16 elements oxygen, sulfur and selenium before immobilisation onto silica nanoparticles in order to characterise them and assess their suitability for use in SMLM imaging. The change in aromaticity due to the incorporation of larger atoms was thought to have an effect on the measured photophysical properties. The structure of the selected dyes ensures that any difference in properties is solely as a result of atomic substitution, and negates any flexibility in the molecule that may disturb aromaticity in another way.

### 2.1 Benzochalcogenadiazoles in the literature

The NBD (4-nitrobenzoxadiazole, Figure 2.1) dye moiety was initially selected as a target in the Jones group due to its small molecular mass, large Stokes shift, and ease of functionalisation. Binding specificity for biological targets can be added *via*  $S_NAr$  reaction of a nucleophile such as an amine with the corresponding commercially available NBD-halide (NBD-Cl is the cheapest and most common halo-derivative of the dye).

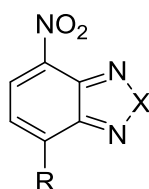


Figure 2.1 – The general structure of the 4-nitrobenzochalcogenazole moiety.  $X = O, S, Se$  for NBD, NPT and NPSe respectively.  $R$  denotes a convenient position for functionalisation.

NBD has proven itself to be a versatile dye and has been used in many live-cell studies to image cellular constructs and to monitor uptake of certain substances by cells.<sup>87–90</sup> The dye has also been used in fluorescence studies and as a sensor for many metals and other functional groups in non-biological settings.<sup>91–94</sup>

The sulfur containing analogue 4-nitropiazthiol (NPT, Figure 2.1) has been used to a much lesser extent as a biological probe but has found application in non-linear optics,<sup>95</sup> shows fungicidal, herbicidal and insecticidal activity and acts as a mild vasodilator,<sup>96</sup> and inhibits the *P. falciparum* thioredoxin reductase enzyme found in the species of bacteria that causes one of the deadliest strains of malaria.<sup>97</sup> It has also been shown that NPT can be metabolised and reduced to the corresponding 4-aminopiazthiol in some biological systems such as *E. coli* and rat livers.<sup>98</sup>

Both NBD and NPT, and the selenium containing derivative 4-nitropiazselenol (NPSe, Figure 2.1) have been patented for use as herbicides and hair colourants.<sup>99,100</sup> Aside from these applications, little work has been done in the study of NPSe derivatives. Publications in which the moiety has been included primarily focus on their synthesis and functionalisation for use as mutagens and fungicides, though these have been proven to be ineffective.<sup>101–103</sup>

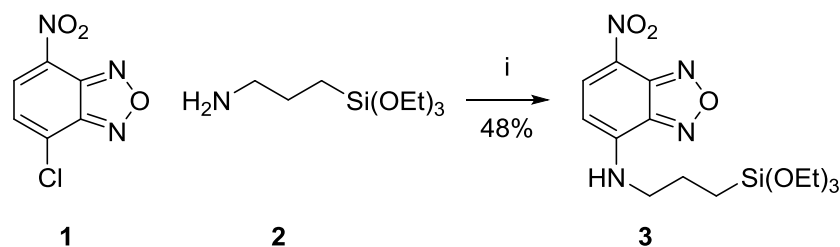
The tellurium containing derivative has been studied to a small extent in a number of experimental and theoretical analyses including the formation of dimers and other non-covalent chains formed via the interactions between the tellurium and nitrogen atoms caused by chalcogen bonding.<sup>104</sup> The potential toxicity of such compounds and the risks associated with using tellurium precludes further investigations though, and tellurium derivatives were omitted from this work as a result.

## 2.2 Dye synthesis

As mentioned above, the simplest method for functionalisation in the NBD series is to perform an  $S_NAr$  reaction using a nucleophile to displace the halogen of the *p*-halo-nitro arene. Given that the chlorine derivative was the cheapest halo-derivative, NBD-Cl (**1**) was selected as the starting material. Since the dyes would be ligated to silica



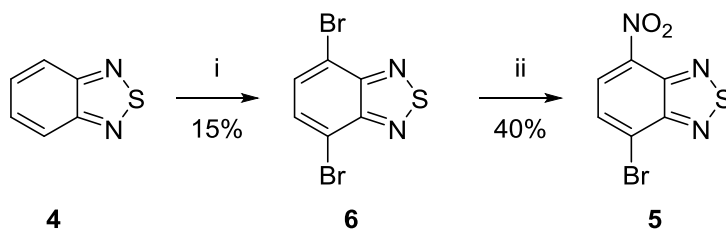
nanoparticles, the bifunctional linker APTES (**2**) was selected for functionalisation. The reaction of NBD-Cl (**1**) with APTES (**2**) to give the silane derivatized NBD-APTES (**3**) was trivial and was preceded in the literature (Scheme 2.1).<sup>91</sup>



*Scheme 2.1 – Synthesis of NBD-APTES (3). i) EtOH, dark, 0 °C – RT, 24 h, 48%.*

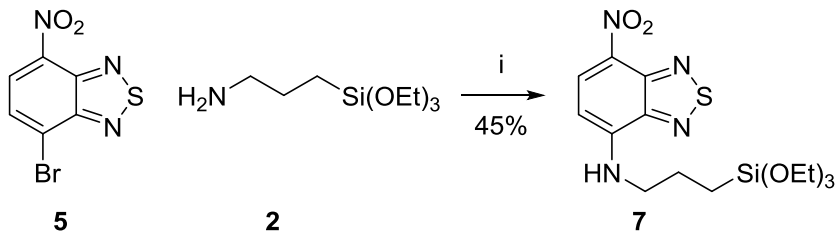
Since there is no commercial source for an NPT-halogen derivative, steps were taken to synthesise one. Though preceded in the literature, tandem bromination/nitration of benzothiazole (**4**, Scheme 2.2) was unsuccessful.<sup>105</sup> The target compound NPT-Br (**5**) was only observed in extremely small quantities in the crude reaction mixture. The primary product was the dibrominated product (**6**, Scheme 2.2), which was proposed as an intermediate in the literature source. Increasing reaction time to 72 hours and performing the reaction at a variety of temperatures did not yield the desired product (**5**). There may, however, have been inaccuracies in the published data since the authors were unable to utilise techniques such as NMR or mass spectrometry at the time of publication.

A more recent publication reports the synthesis of NPT-Br (**5**) by heating dibromobenzothiadiazole (**6**) in aqueous nitric acid (68%) for one hour.<sup>106</sup> The authors indicated that extraction was required, however when repeated the product precipitated when poured over ice water, giving a modest yield of 40% (Scheme 2.2). To increase the rate of this reaction, the gas produced was periodically vented. Without venting the reaction mixture took over 12 hours to change colour from dark orange to pale yellow.



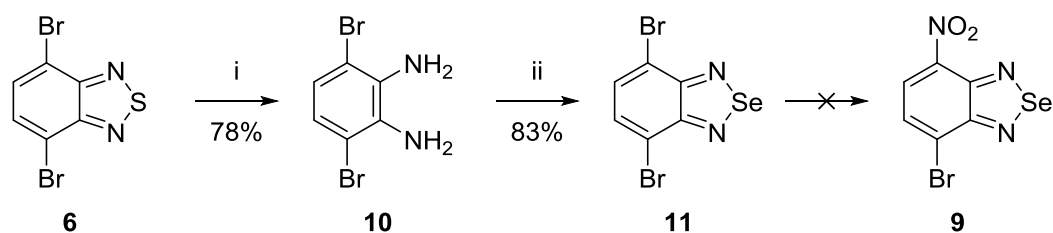
Scheme 2.2 – Synthesis of NPT-Br (**5**) via dibromobenzothiadiazole (**6**). i)  $\text{Br}_2$ ,  $\text{HNO}_3$  (aq), reflux, 48 h, 15%. ii)  $\text{HNO}_3$  (aq), reflux, 1 h, 40%.

With NPT-Br (**5**) in hand, ligation to APTES (**2**) could take place, however attempting to replicate the conditions used for the synthesis of NBD-APTES (**3**) was ineffective and gave recovery of the starting material. Increasing the reaction temperature to  $50^\circ\text{C}$  gave traces of the product by  $^1\text{H}$  NMR analysis but it proved inseparable from the mixture. When repeated with catalytic potassium carbonate, NPT-APTES (**7**) was successfully isolated in a moderate yield (Scheme 2.3).



Scheme 2.3 – Synthesis of NPT-APTES (**7**). i)  $\text{K}_2\text{CO}_3$  (10 mol%), EtOH, dark,  $0^\circ\text{C}$  – RT, 24 h 45%.

The synthesis of the selenium containing derivative NPSe-APTES (**8**) proved to be much more of a challenge. It was initially planned that NPSe-Br (**9**) could be synthesised *via* the reduction of dibromobenzothiadiazole (**6**) giving a 1,2-dianiline species (**10**) into which a selenium atom could be inserted to give a dibromobenzoselenadiazole species (**11**, Scheme 2.4). These reactions were preceded and proceeded with good yields when repeated (78% and 83%, respectively),<sup>107,108</sup> however, *ipso*-substitution of bromine in the dibromo species (**11**) was futile.



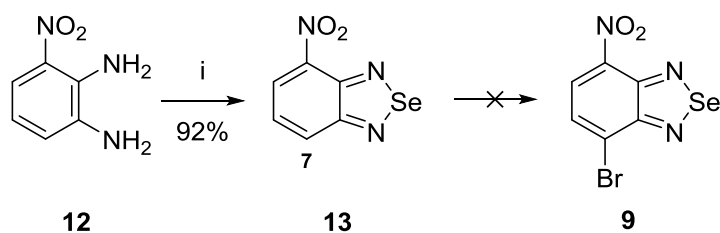
*Scheme 2.4 – Reduction of dibromothiadiazaole (6) followed by selenium insertion. i) NaBH<sub>4</sub>, EtOH, 0 °C – RT, 20 h, 78%. ii) SeO<sub>2</sub>, EtOH/H<sub>2</sub>O, reflux, 2 h, 83%.*

Despite attempting a range of nitrating conditions, including heating the dibromo compound (**11**) to reflux in nitric acid, and using mixtures of nitric and sulfuric acids for varying time periods of up to 24 hours, this reaction only resulted in the degradation of the dibromoselenadiazole starting material (**11**). Alternate nitration conditions using potassium nitrite as the nitrating agent with various copper catalysts were also trialled.<sup>109</sup> The reaction was attempted at a range of temperatures for up to 72 hours with three different copper reagents (CuI, CuBr, and Cu[OTf]<sub>2</sub>) both under thermal conditions (130 °C in DMSO) and under microwave irradiation. None of these approaches gave the desired nitrated product and returned the majority of the starting material. However, since this reaction uses air-sensitive copper(I) in the catalytic cycle, the root of this problem may have been due to an impure nitrogen supply containing oxygen. This was not discovered until after this route had been abandoned.

The next approach taken towards the synthesis of NPSe-APTES (**8**) was the reduction of NPT-Br (**5**) followed by the insertion of selenium in an analogous method to that used for the reduction and selenation of the dibromo species (**6**, Scheme 2.4). Reduction with sodium borohydride was problematic, giving an insoluble black residue as the product. Weaker reductants such as sodium triacetoxyborohydride and sodium cyanoborohydride were trialled. The former reagent gave no reaction and returned the starting material. Analysis of the crude mixture obtained when using the cyanide containing reagent by <sup>1</sup>H

NMR spectroscopy suggested that a small portion of the starting material had been transformed. The reaction was repeated with more hydride equivalents, over a longer time period at varied temperatures. In each case, the starting material was proven to have been consumed by  $^1\text{H}$  NMR spectroscopy and thin layer chromatography (TLC) but mass spectrometry did not provide any evidence of the desired 1,2-diamino-3-bromo-6-nitrobenzene. The peak had an  $m/z$  value that suggested that only one heteroaromatic nitrogen had been reduced fully to the aniline while the other was still bound to sulfur.

As these routes had proven unsuccessful, a survey of structurally similar commercially available compounds was conducted. Insertion of selenium between the nitrogen atoms of commercially available 1,2-diamino-3-nitrobenzene (**12**) was successful in excellent yield to give NPSe-H (**13**, Scheme 2.5), however, subsequent bromination at carbon 7 was unyielding. A range of different brominating agents (molecular bromine, *N*-bromosuccinimide, and tribromocyanuric acid) were trialled in different solvents (acetic acid, dichloromethane, dichloroethane, trifluoroacetic acid, and hydrochloric acid) but no reaction was observed under any of the conditions used.



Scheme 2.5– Selenation of 1,2-diamino-3-nitrobenzene (**12**) to give NPSe-H (**13**), carbon 7 labelled. i)  $\text{SeO}_2$ ,  $\text{EtOH}/\text{H}_2\text{O}$ , reflux, 92%.

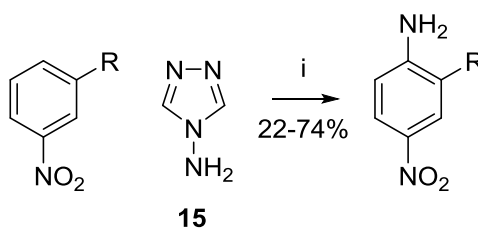
The next analogous commercially available compound was 2-bromo-5-nitroaniline (**14**), whose transformation to the desired dianiline compound was preceded *via* a reaction known as vicarious nucleophilic substitution (VNS).

### 2.3 Vicarious nucleophilic substitution

VNS as a technique was introduced by Makosza and co-workers in 1984 for the introduction of sulfones *ortho*- and *para*- to the nitro functionality in nitroaryl systems.<sup>110</sup>

The reaction involves the addition of an anionic nucleophile bearing a leaving group to aromatic rings. A base is then used to induce  $\beta$ -elimination to give the substituted product.

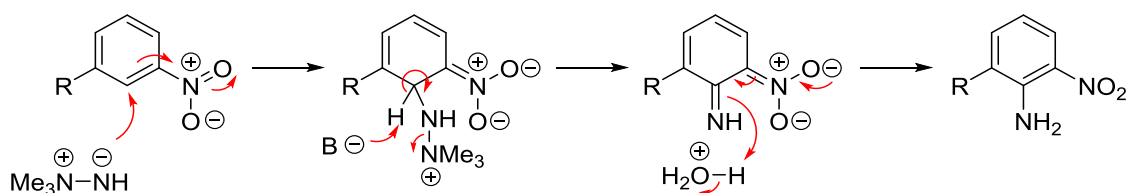
The procedure was adapted in 1986 by Katritzky and Lorenzo as a solution to the harsh and low yielding conditions (photochemical addition in liquid ammonia, or hydrazoic acid in sulfuric acid or with aluminium[III] chloride) usually used for the amination of nitrobenzene compounds.<sup>111</sup> The authors reasoned that the use of a suitable nitrogen containing nucleophile with an attached leaving group may enable similar, more reliable, and higher yielding reactions. The nucleophile they selected was 4-amino-1,2,4-triazole (**15**) due to its tolerance of basic conditions, and they were able to successfully add an amine exclusively to the *para*- position with respect to the nitro group (Scheme 2.6). The reaction would only proceed in dimethylsulfoxide (DMSO).



Scheme 2.6 – Vicarious nucleophilic amination using 4-amino-1,2,4-triazole (**15**) as the nucleophile.  $R = H, \text{ alkyl, EWG, EDG}$ .  $i) ^t\text{BuOK, DMSO, RT, 22-74\%}$ .<sup>111</sup>

Since this publication other reagents were developed for use as aminating agents, all of the general formula of X-NH<sub>2</sub>, where X is a leaving group. *Ortho*- regioselectivity was attained by using the reagents where X was an alkoxy or a trialkylammonium group in combination with an electron donating *meta*-substituent in the 3-position. This invariably

gave amination in the more sterically congested 2-position. Since VNS reactions using *O*-alkyl hydroxylamines (RO-NH<sub>2</sub>) usually required copper catalysis,<sup>112,113</sup> hydrazonium reagents such as 1,1,1-trimethylhydrazonium iodide (Me<sub>3</sub>NNH<sub>2</sub>.I, TMHI) became more popular.<sup>114,115</sup> The positive charge on the quaternary nitrogen vastly improves its leaving group ability and the reagent can be used without catalysis. It also stabilises the deprotonation of the adjacent hydrazone proton to give the hydrazinium ylide – a much more potent nucleophile. A charged intermediate is formed which is protonated on acidic workup (Scheme 2.7).

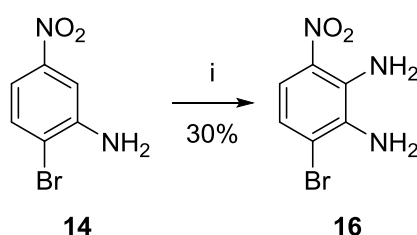


Scheme 2.7 – The proposed mechanism for vicarious nucleophilic amination of nitrobenzene systems using TMHI. R = EDG.<sup>115</sup>

This reaction was reported as being under kinetic control by Kowalski and coworkers in 2009.<sup>115</sup> Their computational analysis of the *ortho*- and *para*- adducts (relative to the nitro group) showed that the transition state energy of *para*- addition is much higher than *ortho*- addition. Additionally, it was shown that when two *ortho*- positions are available and they are not chemically equivalent, only substitution of the position with the lower calculated transition state energy is observed. This energy is lowered by the presence of an electron donating group *meta*- with respect to the nitro moiety.

A British patent published in 2010 claims that VNS can be used for the amination of 2-bromo-5-nitroaniline (**14**) to give 1,2-amino-3-bromo-6-nitrobenzene (**16**), however the characterisation data presented in the patent did not support the proposed product.<sup>116</sup> Despite this, the reaction was attempted using sodium *tert*-pentoxide as the base and

DMSO as the solvent. Initial attempts gave poor mass returns and crude  $^1\text{H}$  NMR spectra with peak splitting to indicate substitution at different positions around the aromatic ring. A change in the work-up procedure, however, did result in the successful isolation of the desired dianiline product (**16**) in 30% yield (Scheme 2.8). The patent suggested that the reaction be worked-up by pouring over ice water and acidifying to pH 3 before extracting with dichloromethane. This procedure was modified such that the product was extracted from the cold aqueous mixture before performing mildly acidic washes to neutralise the mixture and avoid protonation of the dianiline ( $\text{pK}_a$  of the conjugate acids of anilines are usually below 5). The previous work-up procedure may have been causing the desired product to remain in the aqueous phase whereas the modified method gave a crude product that could be used without further purification with only traces of solvents (DMSO) or by-products (trimethylamine or *tert*-pentyl alcohol).



Scheme 2.8 – VNS reaction to yield 1,2-dianiline-3-bromo-6-nitrobenzene (**16**). i) TMHI,  $\text{NaOC}(\text{Me})_2\text{Et}$ , DMSO, RT, 16 h, 30%.

In an attempt to increase the yield of VNS, a range of *N*-protected derivatives (**17-19**) were prepared of 2-bromo-5-nitroaniline (**14**). It was thought that protecting the aniline with electron withdrawing groups would make the benzene ring more electrophilic and thus more susceptible to nucleophilic attack.

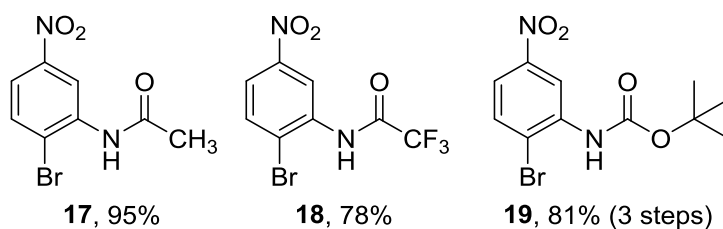
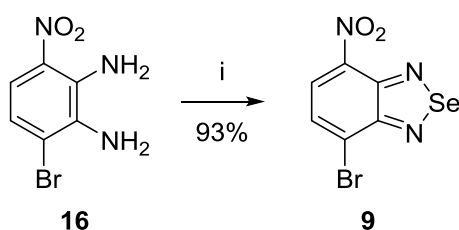


Figure 2.2 – The structures of *N*-protected analogues of 2-bromo-5-nitroaniline.

*N*-Acetyl, trifluoroacetyl, and Boc protected analogues were synthesised (**17**, **18**, and **19** respectively, Figure 2.2), but no reaction was observed when subjected to VNS conditions and starting material was returned in all cases. It is noted that direct Boc-protection was not possible, however, in 1985 it was found that an *N*-acyl-*N*-Boc doubly protected aniline can be selectively cleaved to yield the *N*-Boc compound.<sup>117,118</sup> As such, the *N*-Boc protected aniline was synthesised in 2 steps from the *N*-acetyl aniline (**17**) via a doubly protected *N*-acyl-*N*-Boc aniline intermediate. Although in this case the doubly protected compound was not isolated, it may have been worth attempting to use it in a VNS reaction since one reason that the reaction failed with the monoprotected analogues (**17**, **18**, and **19**) could be deprotonation of the amide N-H proton.



Scheme 2.9 – Selenation to give *N*PSe-Br (**9**). i)  $\text{SeO}_2$  (5 eq), EtOH/ $\text{H}_2\text{O}$ , reflux, 2 h, 93%.

Nevertheless, with the diamine (**16**) in hand it was possible to insert selenium to give *N*PSe-Br (**9**, Scheme 2.9). Unlike the analogous reactions with the dibromo and nitro



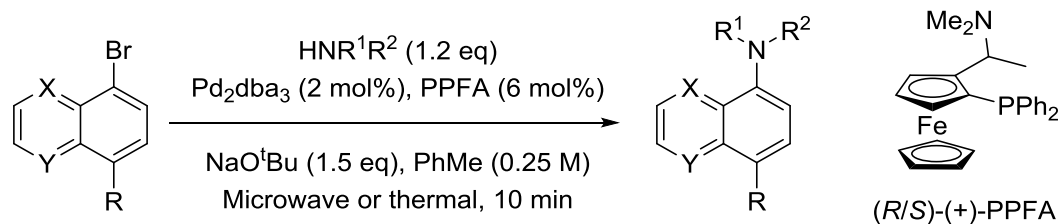
dianiline systems (**10** and **12**, respectively), this reaction required five molar equivalents of selenium dioxide for the reaction to proceed.

Attempts of an  $S_NAr$  reaction on NPSe-Br (**9**) using APTES (**2**) as the nucleophile were unsuccessful under a range of conditions including the use of catalytic or stoichiometric base ( $K_2CO_3$ , NaH,  $KO^tBu$ ) or acid (AcOH), performing the reaction at room or elevated temperatures, and in different solvents (EtOH,  $H_2O$ , THF, DCM), thus a different approach was required for the functionalisation of the selenious heterocycle.

## 2.4 Aryl aminations

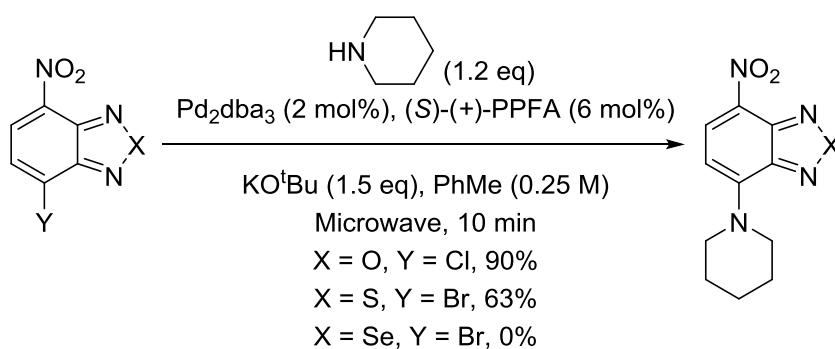
Cross coupling reactions have been used for the functionalisation of aryl halide systems for many years and have revolutionised and broadened the ways in which molecular targets can be synthesised. Suzuki and Sonogashira couplings have been successfully applied to 4,7-dihalogen chalcogenadiazoles for *bis*-arylation to synthesise donor-acceptor-donor systems or conjugated polymers.<sup>95,108</sup> Similar reactions have been applied to 4-halo-7-nitrobenzochalcogenazoles for *ipso*- substitution of the halogen with aryl systems, as well as using CH-activation at position 7 of 4-nitrobenzochalcogenazoles.<sup>95,119–123</sup> To date, the metal catalysed cross coupling of a primary or secondary amine with these systems had not been demonstrated.

On searching through the literature for analogous systems, a palladium catalysed coupling reaction of 1-bromonaphthalenes and 5- and 8-bromoquinolines with primary and secondary amines was possible using the chiral ferrocene based ligand *N,N*-dimethyl-1-[2-(diphenylphosphino)ferrocenyl]ethylamine (PPFA, Scheme 2.10).<sup>124</sup> The products in this study were achiral, and as such the authors do not specify which isomer of PPFA was used. A range of amines were trialled, including aromatic, aliphatic, straight chain, and cyclic variants, with yields ranging from 47-92%.



Scheme 2.10 – Aryl aminations conducted by Wang and co-workers.<sup>124</sup>  $X = CH$  or  $N$ ,  $Y = CH$  or  $N$ ,  $R = H$ ,  $Me$ ,  $OMe$  or  $CN$ . Though the authors did not specify which isomer of PPFA was used, the (+)-planar isomer is shown as an example.

Replication of this reaction using 5-bromoquinoline and piperidine was attempted under both thermal conditions (heating at reflux for 24 hours) and microwave irradiation (ramp from room temperature to 120°C over 360 s using 150 W power then maintain this temperature for a further 540 s at 100 W). Though both conditions did produce the correct product, microwave irradiation gave a higher conversion by analysis of peak integration in the <sup>1</sup>H NMR spectrum of the crude reaction mixture (60% compared to 41% using thermal conditions). In these cases, potassium *tert*-butoxide was used as a substitute for the sodium salt due to availability.

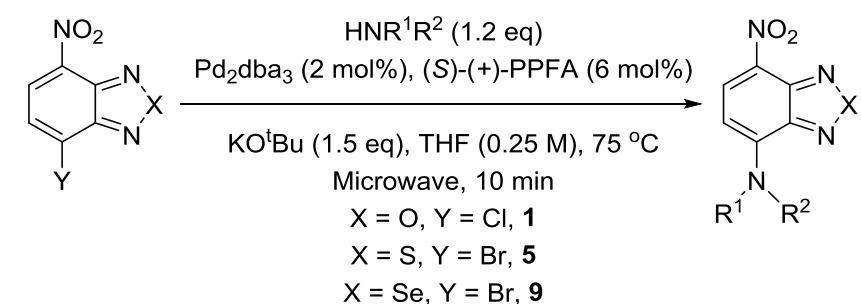


Scheme 2.11 – Amination of oxadiazole, thiadiazole and selenadiazole **1**, **5**, and **9** with piperidine.

This methodology was then applied to NBD-Cl, NPT-Br and NPSe-Br (**1**, **5**, and **9**, respectively) which gave good yields under microwave irradiation for the oxygen and sulfur containing compounds (90% and 63% yields, respectively, Scheme 2.11) but the

selenium compound proved to be unreactive under these conditions. It was thought that the selenium derivative was unreactive due to low solubility in toluene. When the reactions with piperidine were repeated using tetrahydrofuran (THF) as the solvent, the sulfur and selenium containing compounds gave yields of 61% and 30%, respectively.

Table 2.1 – Isolated yields for the amination of diazoles **1**, **5**, and **9** with various amines.

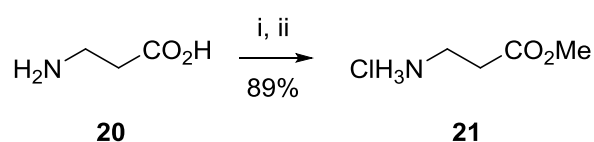


| Entry | $\text{HNR}^1\text{R}^2$ | X  | Yield (%) <sup>a</sup> |
|-------|--------------------------|----|------------------------|
| 1     |                          | O  | 87                     |
| 2     |                          | S  | 61                     |
| 3     |                          | Se | 30                     |
| 4     |                          | O  | 30                     |
| 5     |                          | S  | 45                     |
| 6     |                          | Se | 23                     |
| 7     |                          | O  | 41                     |
| 8     |                          | S  | 24                     |
| 9     |                          | Se | 23                     |
| 10    |                          | O  | 33                     |
| 11    |                          | S  | 17                     |
| 12    |                          | Se | 12                     |
| 13    |                          | O  | 10                     |
| 14    |                          | S  | 8                      |
| 15    |                          | Se | 7                      |
| 16    |                          | O  | 11                     |
| 17    |                          | S  | 6                      |
| 18    |                          | Se | 23                     |
| 19    |                          | O  | 16                     |
| 20    |                          | S  | 36                     |
| 21    |                          | Se | 25                     |

<sup>a</sup> Refers to isolated product.

These yields were perhaps lower due to reduced solubility of the other reagents in THF compared to toluene. Several other amines (including APTES, **2**) were tested to gauge the scope of the reaction (Table 2.1). Once aliphatic, aromatic and benzylic amines had been tested (entries 1 – 12), the remaining amines were selected in order to provide handles for further functionalisation. APTES was used to install silane functionality such that the dyes could be conjugated to silica nanoparticles (entries 13 – 15). Allylamine was used to install an unsaturated bond which could be functionalised in many ways, including halogenation, hydroboration or epoxidation (entries 16 – 18).

A methyl protected amino acid ( $\beta$ -alanine, entries 19 – 21) was successfully coupled to the dyes to provide a handle for peptide synthesis and biological specificity. The coupling reaction was unsuccessful with unprotected amino acids containing a carboxylic acid. The HCl salt of  $\beta$ -alanine methyl ester (**21**) was prepared in one step using thionyl chloride in methanol in high yield (Scheme 2.12).

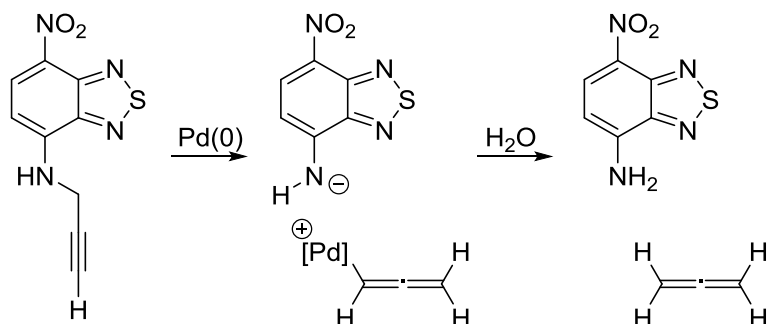


*Scheme 2.12 – Methyl protection of  $\beta$ -alanine (**20**) to the hydrochloride salt of the methyl ester (**21**). i)  $\text{SOCl}_2$ , MeOH, 0 °C to rt, 2h. ii)  $\text{HCl}(\text{aq})$ .*

Interestingly, when attempting to couple NBD-Cl (**1**) with propargylamine a rather different outcome was obtained. It was found that once aryl amination had taken place a rearrangement occurred enabling the release of allene leaving a primary amine bound to the aromatic system (Scheme 2.13). This result was confirmed by  $^1\text{H}$  NMR spectroscopy, high resolution mass spectrometry, and infrared spectroscopy. The depropargylation of propargyl amines and ethers has been documented a number of times in the presence of catalytic palladium species under basic conditions, in some cases showing selectivity for

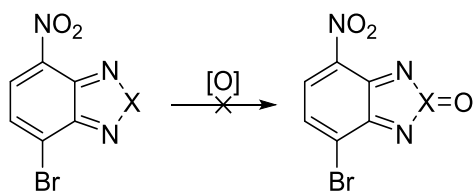
propargyl groups over allyl groups, explaining why the allyl variants were isolable.<sup>125–128</sup>

This reaction pathway may have been particularly favourable in this case due to the ability to delocalise the negative charge in the intermediate to the nitro group in the *para*-position.



Scheme 2.13 – Palladium catalyzed depropargylation of NPT-2-propyne.

A study in which a phosphorus(V) containing rhodamine was synthesised *via* the oxidation of its phosphorous(III) counterpart raised questions about whether more dyes could be added to this study by the oxidation of the sulfur and selenium atoms in NPT- and NPSe-Br (**5** and **9**) to give the sulfoxide and selenoxide (Scheme 2.14).



Scheme 2.14 – Proposed oxidation of sulfur or selenium containing compounds. X = S, Se.

Unfortunately, it was not possible to oxidise either compound using hydrogen peroxide, oxone or potassium permanganate and in all cases starting material was returned. This is likely due to the involvement of the lone pairs of the sulfur and selenium atoms in the aromatic system. In some cases, the bonds in the benzothiadiazole structure have been

drawn differently to show sulfur existing in its S(IV) oxidation state (Figure 2.3).<sup>129</sup> If this was the true structure of the sulfur and selenium containing molecules, it would explain why oxidation at the 2-position is not possible.

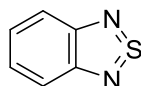


Figure 2.3 – Alternate structure of 2,1,3-benzothiadiazole showing sulfur existing as S(IV).

## 2.5 Photophysical properties

With the three silane functionalised dyes NBD-, NPT- and NPSe-APTES (**3**, **7**, and **8** respectively) in hand, it was important to characterise their photophysical properties. Intrinsic properties such as absorption and emission wavelength maxima ( $\lambda_{\text{abs/em}}$ , Figure 2.5) were measured before subsequently measuring molar absorption coefficient ( $\epsilon$ ), quantum yield ( $\Phi$ ), and excited state lifetime ( $\tau$ , Table 2.2).

Though the absorption and emission maxima for the oxygen and sulfur containing dyes were similar, the maxima were highly red shifted for the selenous dye. Bathochromic shift of selenium containing fluorophores has been observed previously, and in the selenium containing analogue of D-luciferin this was attributed to the polar effect.<sup>73,130</sup>

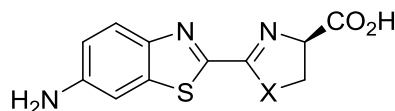


Figure 2.4 – The structure of D-luciferin ( $X = S$ ) and the selenium containing analogue ( $X = Se$ ).

In this context it is assumed that the polar effect refers to the lower electronegativity of selenium meaning that electrons are less drawn to the heteroatom, thus less energy is required to promote an electron to the excited state and the wavelength maxima are larger.

Detty reports that as heavier atoms are incorporated the oxidation potentials of the molecules become more negative and the reduction potentials become more positive, which is reflected in the narrowing of the HOMO-LUMO energy gap, making transition easier and requiring a longer wavelength, lower energy photon.<sup>71</sup>

Table 2.2 – Photophysical properties of NBD-, NPT-, and NPSe-APTES (3, 7, and 8 respectively).

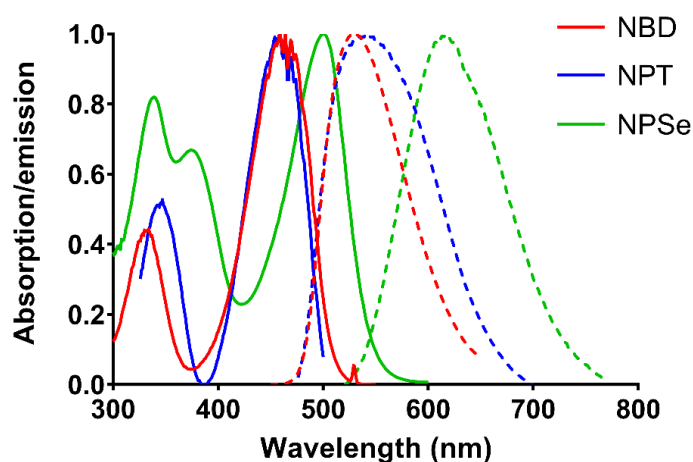


Figure 2.5 – Normalised absorption (solid lines) and emission (dashed lines) for NBD-, NPT- and NPSe-APTES (3, 7, and 8 respectively).<sup>a</sup>

| Dye            | $\lambda_{\text{abs}} / \text{nm}$ | $\lambda_{\text{em}} / \text{nm}$ | $\epsilon / \text{M}^{-1}\text{cm}^{-1}$ <sup>b</sup> | $\Phi / \%$ <sup>c</sup> | $\tau / \text{ns}$ <sup>d</sup> |
|----------------|------------------------------------|-----------------------------------|---|--------------------------|---------------------------------|
| NBD-APTES (3)  | 465                                | 542                               | 24,000  | 0.8                      | 2.6                             |
| NPT-APTES (7)  | 460                                | 550                               | 1,400   | 0.2                      | 1.1                             |
| NPSe-APTES (8) | 500                                | 615                               | 3,900   | 0.2                      | 1.7                             |

<sup>a</sup> Normalised for clarity due to vast differences in magnitude. <sup>b</sup> Extrapolated from calibration curves plotted using solutions with concentrations between 10-100  $\mu\text{M}$ . Accurate to 2 significant figures. <sup>c</sup> Measured using an integration sphere and compared to BODIPY-Br with a quantum yield of 7.5%. <sup>d</sup> Measured using a time-correlated single photon counting method for time-resolved photoluminescence.

The observed decrease in molar absorption coefficient is in broad agreement with other dyes with substitution down the chalcogen group.<sup>72–75</sup> This has previously been attributed to a decrease in the oscillation strength of the  $S_0 \rightarrow S_1$  transition.<sup>131,132</sup> According to Nijegorodov and Mabbs, the introduction of heavier atoms changes the parameters of

matrix elements in the molecular orbital, making absorption less likely. When incorporating heavier, less electronegative atoms the distribution of electrons in the molecular orbitals of the dyes may change. A poorer overlap between the HOMO and the LUMO would result in a smaller oscillator strength.<sup>133</sup> These changes are also reflected in the calculated oscillator strength from the computational studies (Table 2.3). Similarly, there was a drop in the quantum yield when larger atoms were incorporated due to a higher probability of transfer to the triplet state *via* ISC. The method used was not accurate enough to allow more detailed measurements to be taken.

Though there was not a vast difference between the excited state lifetimes of the three dyes, it was clear that the value for NBD-APTES (**3**) was much larger than the other two. This, again, indicates that the oxygen containing dye favours fluorescence rather than intersystem crossing to a dark state.

As a crude assessment of the aromaticity of the three silane functionalised dyes, the chemical shifts of the aromatic protons were compared. As predicted by Jona,<sup>134</sup> the inclusion of heavier atoms resulted in an increase in aromaticity. The aromatic peaks were shifted most downfield in the sulfur containing molecule (**7**), the analogous peaks in the spectrum of the oxygen derivative (**3**) were the most upfield, with the peaks from the selenium containing compound (**8**) in the middle (Figure 2.6). This suggests that the protons in the sulfurous molecule are experiencing the greatest ring current and the sulfur compound is most aromatic, whereas the protons in the oxygenated compound experience a smaller ring current, making the oxygen derivative least aromatic, much like the chalcogenazoles studied in Bird's 1992 article.<sup>76</sup>



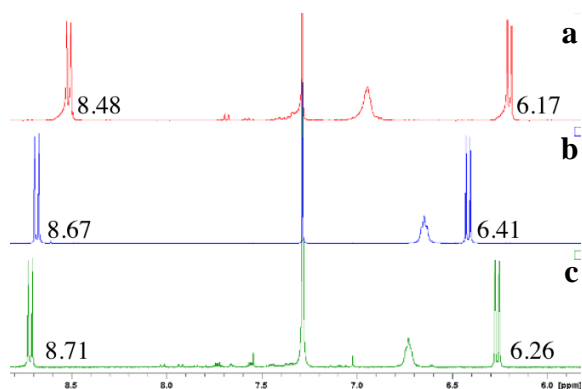
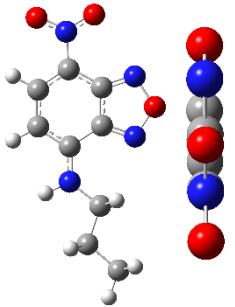
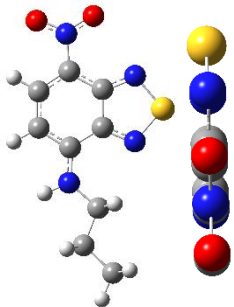
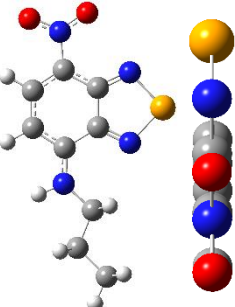


Figure 2.6– Comparison of the aromatic region in the  $^1\text{H}$  NMR spectra of a) NBD-, b) NPT-, and c) NPSe-APTES (**3**, **7**, and **8** respectively) with chemical shift measured on the ppm scale with respect to the  $\text{CDCl}_3$  solvent peak.

In order to prove that the increasing size of the heteroatom was not having an effect on the planarity of the molecules, geometry optimisations of model systems omitting the silane group were undertaken. Subsequently, the energy levels of the optimised structures were calculated in order to calculate the  $S_0 - S_1$  transitional energy. Geometry optimisations were calculated using density functional theory (DFT) which uses electron density rather than wavefunctions to complete calculations, drastically shortening calculation time because there is less of an increase in the complexity of electron density calculations as the number of electrons in the system increases. Energy levels were calculated using a time-dependant self-consistent field (TD-SCF) DFT which is used to calculate the effect of an electromagnetic field (i.e. a photon).

The major component of the calculated  $S_0 - S_1$  transition was attributed to a HOMO – LUMO transition in all three cases, but transitional energies were not in agreement with the experimentally measured figures. However, the calculated figures do correctly predict which dyes will have the highest and lowest absorption maxima, and that the oxygen and sulfur containing dyes would have similar absorption maxima, while the absorption maximum for the selenium containing dye would be red shifted (Table 2.3).

Table 2.3 – Results of the computational analyses of analogues of NBD-, NPT-, and NPSe-APTES (3, 7, and 8 respectively).

| Dye  | NBD-APTES (3)   | NPT-APTES (7)   | NPSe-APTES (8)  |
|--|---|---|---|
| Geometrically optimised structure of analogue <sup>a c</sup> |  |  |  |
| N-X-N internal bond angle (°) <sup>a</sup>                   | 113.0   | 99.4  | 93.5  |
| Average N-X bond length / Å <sup>a</sup>                     | 1.365   | 1.638   | 1.801   |
| HOMO – LUMO difference / eV <sup>b</sup>                     | 3.2014  | 3.2509  | 3.0403  |
| Calculated $\lambda_{\text{abs}}$ / nm                       | 437   | 448   | 482   |
| Calculated oscillator strength                               | 0.3876  | 0.3080  | 0.2381  |
| Experimental $\lambda_{\text{abs}}$ / nm <sup>d</sup>        | 465   | 460   | 500   |

<sup>a</sup> Calculated using Gaussian 09 using DFT theory with a B3LYP 6311g (d,p) basis set.<sup>135</sup> <sup>b</sup> Calculated using Gaussian 09 using TD-SCF DFT theory with a B3LYP 6311g (d,p) basis set and was solved for N=100 states. <sup>c</sup> Molecular models viewed perpendicular to, and in the plane (from above) of the aromatic system of each dye molecule. Hydrogen atoms omitted from in-plane view for clarity. <sup>d</sup> measured in water.

Modelling shows that the aromatic systems do remain planar but the ring in which the chalcogen is contained becomes distorted in order to accommodate the larger atoms. This is shown by an increase in the N-X bond length and a narrowing of the internal N-X-N bond angle as the ring is elongated and becomes more puckered.

The rate of fluorescence bleaching was then measured using a method described by Sauer *et al.*<sup>56</sup> in which dye solutions are exposed to a laser in order to induce photobleaching before fluorescence is reactivated by reincorporation of oxygen *via* agitation. Three differently buffered solutions were tested to assess the differences between them, and confirmed GLOX buffer (glucose oxidase, catalase and glucose) with mercaptoethylamine (MEA) as being the most suited for SMLM imaging. When fluorescence intensity dropped to 10% of initial fluorescence intensity the cuvette was removed from the experimental equipment, the stopper removed for a few seconds to allow oxygen back into the system, then replaced before shaking the cuvette. These interruptions can be observed in the results graphs when fluorescence intensity drops to zero for a short period of time (Table 2.4).

The first system tested was the dye dissolved in distilled water. All three dyes proved to be photostable when irradiated with laser light under these conditions. Although fluorescence intensity of the sulfur and selenium containing dyes neither increased or decreased over the course of the one hour experiment, the oxygen containing NBD-APTES (**3**) actually showed an increase in fluorescence intensity to a plateau after approximately 40 minutes at all concentrations and laser intensities tested (Table 2.4).

This phenomenon has not previously been observed in the literature concerning photoactive molecules. Some fluorescent molecules display an increase in fluorescence intensity on binding to a substrate,<sup>94,136</sup> but since only the dye is present in aqueous solution this is also improbable. Laser irradiation of the compound may photocatalyse a transformation to a more intensely fluorescent species.<sup>137</sup> Although there was no change in the emission maximum, this should not be ruled out. Increases in fluorescence intensity have previously been induced using pulsed lasers by Hell and coworkers,<sup>138</sup> but in this case laser irradiation was continuous. Further investigation is required to determine the

cause of this phenomenon. The MatLab code used to obtain bleaching data integrated absorption spectra between a specified range of wavelengths at each time point to give the area under the spectrum (Appendix 1, page 134).

The introduction of additives had a profound effect on the ways in which the dyes behaved. The second buffer system tested was the dye dissolved in distilled water with the addition of MEA at 0.1 M. This prompted the dyes to begin photobleaching. The rate of decay increased with the increasing atomic mass of the chalcogen contained within the molecules (i.e. the selenium containing compound decayed fastest and the oxygen containing dye decayed slowest). When fluorescence reactivation was attempted there was only a small recovery of fluorescence intensity (Table 2.4).

Next tested was the GLOX buffering system made up of the dyes dissolved in distilled water with MEA at a concentration of 0.1 M, glucose oxidase at a concentration of 0.5 mg/mL, catalase at a concentration of 0.04 mg/mL, and 10% w/v of  $\beta$ -glucose. This prompted faster bleaching in the oxygen and selenium containing dyes, but slowed the bleaching process down in the sulfur containing dye NPT-APTES (7). This indicates that the oxygen scavenging system has the opposite effect on the thiadiazole and promotes a longer 'on' state for super-resolution imaging. It may also imply that the dark 'off' state is less accessible for the sulfur variant.

Table 2.4 – Results of reversible bleaching experiments for NBD-, NPT-, and NPSe-APTES (3, 7, and 8, respectively).<sup>a</sup>

| Dye  | NBD-APTES (3)       |      | NPT-APTES (7) |       | NPSe-APTES (8) |      |
|--|---------------------|------|---------------|-------|----------------|------|
| Bleaching graphs   |                     |      |               |       |                |      |
|  | Buffer <sup>b</sup> | A    | B             | A     | B              | A    |
| Decay rate<br>/ $\times 10^{-3} \text{ s}^{-1}$ <sup>b</sup> | 0.265               | 1.21 | 0.555         | 0.439 | 2.06           | 10.0 |
| Average<br>recovery / %                                      | 12                  | 78   | 12            | 48    | 15             | 81   |
| Average<br>PED / % <sup>c</sup>                              | -                   | 15   | -             | 15    | -              | 24   |

<sup>a</sup> All dye solutions were diluted to  $1 \times 10^{-5}$  M and data was recorded using OceanView and analysed using Matlab.<sup>139</sup> <sup>b</sup> A: Dye solution in distilled water with 0.1 M MEA; B: Dye solution in distilled water with 0.1 M MEA and GLOX buffering. <sup>c</sup> Calculated as a percentage of fluorescence intensity decay before the rate of decay slowed and became exponential.

The addition of GLOX buffer also increased the amount of fluorescence intensity recovered after reincorporation of oxygen into the system. There was a vast increase in the average fluorescence intensity recovery of the oxygen and selenium variants, and a smaller but still notable increase for the thiadiazole. This result also indicates that the sulfur containing molecule has a less accessible 'dark' state since a greater proportion of dye molecules are permanently photobleached rather than entering the dark state.

When dissolved in the GLOX buffer, each dye experienced two phases of fluorescence intensity decay, both at the start of each experiment and after each agitation. Exponential decay was always preceded by a sharp loss in fluorescence intensity which will henceforth be referred to as pre-exponential decay (PED). PED was measured as a percentage of total fluorescence intensity lost in each cycle before decay became exponential. PED was larger for the selenium containing dye (**8**), implying that access to its dark state may be easier than for the other two compounds.

As decay in fluorescence intensity is observed, the structure of the dyes may be altered. Likely candidates for reduced structures are 1,3-dihydro-2,1,3-benzochalcogenazole structures where the nitrogen atoms in the five-membered ring are protonated.

With the solution phase analysis complete, hints about the blinking activity of each dye were uncovered but the phenomenon of photoblinking had not yet been observed for any of the three compounds. The blinking activity of the dyes (and hence suitability for super-resolution imaging) was assessed by adopting a method described by Gibbs, *et al.* in which dyes were dissolved in a polyvinyl alcohol (PVA) solution and subsequently dried onto a glass surface to give a matrix with a low dye concentration (so low that individual dye molecules were not within Abbe's limit from each other and hence were not diffraction limited).<sup>57</sup> The dyes, dissolved in a PVA solution (47,000 MW, 1 wt% in deionised water), were added to glass microscopy slides and air-dried overnight before

adding a buffer, sealing the system with a cover slip and clear nail polish, and imaging under a microscope. Since in the solution phase there was no photobleaching recorded without the addition of either MEA or GLOX, these were the only buffer systems tested.

Table 2.5 – Blink analysis of NBD-, NPT-, and NPSe-APTES (3, 7, and 8, respectively). <sup>a</sup>

| Dye                  | Buffer <sup>b</sup> | Average blink density / $\mu\text{m}^{-2}$ <sup>c</sup> | Average on time / s <sup>d</sup> | Average number of cycles <sup>d</sup> |
|----------------------|---------------------|---|----------------------------------|---------------------------------------|
| NBD-APTES<br>(3)     | A                   | 1.40  | 0.19                             | 2.9                                   |
|                      | B                   | 1.16  | 0.39                             | 4.9                                   |
| NPT-APTES<br>(7)     | A                   | 1.30  | 0.22                             | 1.4                                   |
|                      | B                   | 2.00  | 0.33                             | 3.0                                   |
| NPSe-APTES<br>(8)    | A                   | 1.01  | 0.11                             | 1.5                                   |
|                      | B                   | 1.46  | 0.34                             | 2.9                                   |
| Control <sup>e</sup> | A                   | 0.14  | 0.11                             | 1.3                                   |
|                      | B                   | 0.03  | 0.06                             | 1.0                                   |

<sup>a</sup> All dye solutions were diluted to  $3 \times 10^{-8}$  M in a 1 wt% PVA (48,000 MW) in distilled water. Andor Solis was used with Fiji<sup>51,52</sup> and the ThunderSTORM plugin<sup>50</sup> to record and analyse blink data. <sup>b</sup> A: Dye solution in aqueous 1% PVA with 0.1 M MEA; B: Dye solution in aqueous 1% PVA with 0.1 M MEA and GLOX buffering. <sup>c</sup> Calculated as the number of blinking events captured within a specified area over the duration of the experiment. <sup>d</sup> Calculated by plotting z-axis profiles of pixel intensity for individual molecules. <sup>e</sup> 1% PVA solution dropped onto microscope slide with no dye.

Data were taken between 30-60 minutes after the addition of a buffer such that the buffer had had enough time to fully penetrate the PVA matrix, but not so long as to threaten the integrity of the matrix. The properties analysed for each dye were the average number of blinks in a  $\mu\text{m}^2$  area (blink density), the average length of continuous emission (on time), and the number of times blinking molecules switched between their ‘on’ and ‘off’ states (number of cycles, Table 2.5).

The dyes did not display a trend in blinking density between buffer systems. There was a reduction in blink density for the oxygen containing NBD-APTES (3) when switching from buffer system A to B, though this was reversed for the dyes containing the heavier atoms which both showed an increase in blink density in GLOX buffer. This suggests

that the oxygen scavenging GLOX system has a stabilising effect on the benzoxadiazole dark state, suggesting that the dark state for this molecule does not manifest as, or is not accessed *via* a triplet state since the triplet quenching thiol MEA cannot override this stabilising effect. By this logic, the increase in blink density in GLOX buffer for NPT- and NPSe-APTES (**7** and **8**, respectively) also suggests a stabilisation of the dark states since they can be accessed more rapidly, but the dark states in these molecules may either be triplet states or be accessed *via* triplet states since the presence of triplet quenching MEA forces relaxation down to the ground state and once again begin a cycle of fluorescence emission. This may also be linked to the fact that sulfur atoms in organosulfur compounds have been found to stabilise electronic dark states,<sup>140</sup> however, this area has not been previously investigated in organoselenides.

Blinking molecules in all three cases on average presented prolonged periods of continuous emission (longer on times) and blinked more frequently (higher number of cycles) under the GLOX buffering system. These attributes were measured by plotting *z*-axis profiles for individual blinking fluorophores (Figure 2.7).

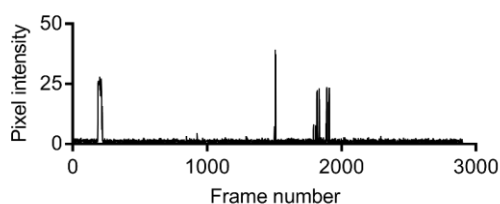


*Figure 2.7 – Representative z-axis profile of pixel intensity for an individual blinking molecule of NBD-APTES (3).*

The *z*-axis profiles can in turn be simplified to so-called on/off trajectories in which any signal above a specified threshold is denoted ‘on’ giving a binary trace (Figure 2.8). In this case, the threshold was set to a pixel intensity of 5 counts. This enables a less



subjective assessment of whether or not a molecule was blinking and whether or not it could be distinguished from the background noise.

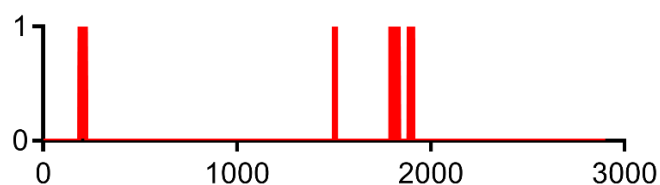
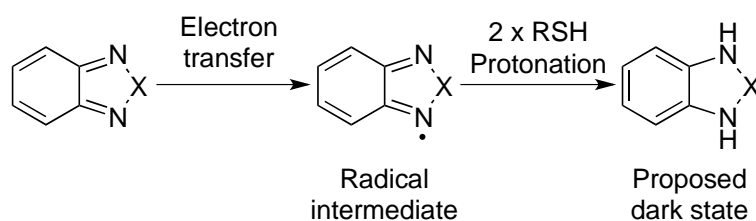


Figure 2.8 – Representative on/off trajectory for an individual molecule of NBD-APTES (3).

The longer on times and higher number of blinking cycles suggest a stabilising effect on the dark state in the presence of GLOX (since it can be accessed more frequently). When comparing the number of blinking cycles going from an MEA to a GLOX buffered solution, there was a higher increase in the number of blinking cycles for the sulfur and selenium containing dyes (214% and 193%, respectively) compared to the oxygen containing compound (169%), which may again suggest that MEA may have less of an effect on quenching the dark state. Despite this, NBD-APTES (**3**) was much more active than its heavier counterparts, and this result correlates with the excited state lifetimes for each dye. The enhanced blink rate may also explain why blinking was not observed in bacteria in the initial control experiments conducted at the start of the project (Section 1.8) – the high density of fluorophores blinking at high speed meant that blinking was undetectable and individual molecules could not be localised. The dye may, however, be more suited to other techniques such as super-resolution radial fluctuation (SRRF) which requires low-level illumination intensity, or 3B which is capable of analysing overlapping fluorophores.

Since the lengths of the dark states for each dye were long-lasting (several seconds) it is likely that the blinking mechanism is redox blinking.<sup>141</sup> Reversible redox reactions of the

dyes with MEA *via* photoinduced electron transfer which result in a non-fluorescent radical intermediate that could subsequently be protonated (Scheme 2.15). Reaction *via* a radical intermediate is more likely to occur from a triplet state,<sup>69,141</sup> and the heavier atoms in the sulfur and selenium containing dyes may be promoting this, resulting in longer dark states and fewer observed blinking events.



*Scheme 2.15 – Route to the proposed dark state for benzochalcogenazoles.*

Further analyses were undertaken to determine the number of photons detected per blinking event (calculated by dividing the pixel intensity value by the analog-to-digital ratio for the camera used) and the average on/off duty cycle (average fraction of time a single molecule spent in the ‘on’ state after equilibrium is reached) over the duration of the 150 s experiment.

The average duty cycles for each of the dyes in this study are comparable and similar to top performing dyes currently used for STORM, as analysed by Dempsey and coworkers.<sup>142</sup> The number of photons detected per blink is on average lower than, but of the same magnitude, as other dyes that absorb in the same region of the visible spectrum.<sup>142</sup> The dyes also perform similarly in this respect to commonly used SMLM dyes suspended in PVA matrices.<sup>57</sup>

Table 2.6 – Further blink analysis of NBD-, NPT-, and NPSe-APTES (**3**, **7**, and **8**, respectively). <sup>a</sup>

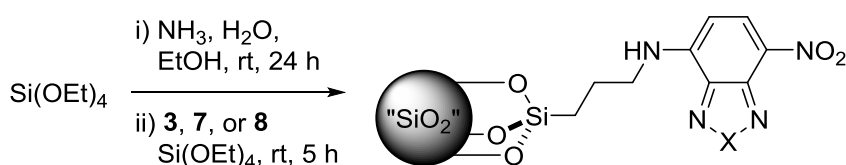
| Dye                        | Buffer <sup>b</sup> | Avg. photons detected per blink <sup>c</sup> | Avg. on/off duty cycle |
|----------------------------|---------------------|--|------------------------|
| NBD-APTES<br>( <b>3</b> )  | A                   | 182  | 0.0013                 |
|                            | B                   | 889  | 0.0027                 |
| NPT-APTES<br>( <b>7</b> )  | A                   | 514  | 0.0015                 |
|                            | B                   | 875  | 0.0023                 |
| NPSe-APTES<br>( <b>8</b> ) | A                   | 164  | 0.00078                |
|                            | B                   | 468  | 0.0023                 |

<sup>a</sup> All dye solutions were diluted to  $3 \times 10^{-8}$  M in a 1 wt% PVA (48,000 MW) in distilled water. FITC filter cube was used. Andor Solis was used with Fiji,<sup>51,52</sup> and the ThunderSTORM plugin to record and analyse blinking data.<sup>50</sup> <sup>b</sup> A: Dye solution with MEA (0.1 M); B: Dye solution with MEA (0.1 M) and GLOX buffer. <sup>c</sup> Calculated based on the analog-to-digital ratio for the camera used (Andor Zyla sCMOS) being 0.28 as stated in the manufacturers specifications.

It has been proven in this study that the dyes emit sufficient photons for fluorescence to be distinguished from background noise and for the localisation of individual molecules. While under ideal SMLM conditions (Buffer B, Table 2.5), the NBD- and NPT-APTES (**3** and **7** respectively) performed similarly, the selenious derivative (**8**) appeared to emit far fewer photons. This may be as a result of the poor overlap of the available laser wavelengths with the absorption spectrum of NPSe-APTES (**8**). All three dyes were capable of stochastically photoblinking throughout the duration of these experiments.

## 2.6 Nanoparticle synthesis and functionalisation

Armed with the knowledge of how individual molecules in sparsely populated samples behave, it was then prudent to see if the previous results could be used to predict the suitability of a dye to take images of small structures using SMLM techniques. Silica nanoparticles were synthesised *via* a Stöber synthesis in which the siloxane functionalised dyes were added at a later stage to coat the surface (Scheme 2.16).



Scheme 2.16 – Synthesis of fluorescent nanoparticles.  $X = O, S,$  or  $Se$  for NBD-, NPT-, and NPSe-APTES (**3**, **7** and **8** respectively).

It was imperative that nanoparticles were not isolated before the addition of the dyes in order for successful ligation to take place. The sizes of the nanoparticles coated with the oxygen, sulfur, and selenium containing dyes were measured to be  $240 \pm 10$ ,  $223 \pm 65$ , and  $257 \pm 8$  nm, respectively by dynamic light scattering (DLS, Figure 2.9A). This result was confirmed for the NBD-APTES (**3**) coated nanoparticles using scanning electron microscopy (SEM, Figure 2.9B). To confirm that the nanoparticles had been coated with the dyes, emission spectra were taken of suspensions of the nanoparticles and they were viewed under a confocal microscope.

After their synthesis, nanoparticles were isolated by centrifugation and resuspended in distilled water for storage. Although aggregation was not an immediate concern sedimentation (particles settling at the bottom of their container) was observed when left unperturbed overnight. Particle size and polydispersity of unlabelled nanoparticles was monitored over time using DLS. There was no evidence of aggregation after 12 days, however at day 49 the average particle size had increased by 22% (from 370 to 451 nm) and the polydispersity index (PDI, a measure of size uniformity ranging from 0 for a completely monodisperse sample to 1 for completely polydisperse sample) had increased from 0.07 to 0.22 showing aggregation to a wide range of particle sizes. To avoid aggregation, the functionalised nanoparticles were isolated by centrifugation and stored dry, which prevents the process from occurring (the high surface tension of water induces aggregation in aqueous solutions/suspensions).<sup>143</sup>

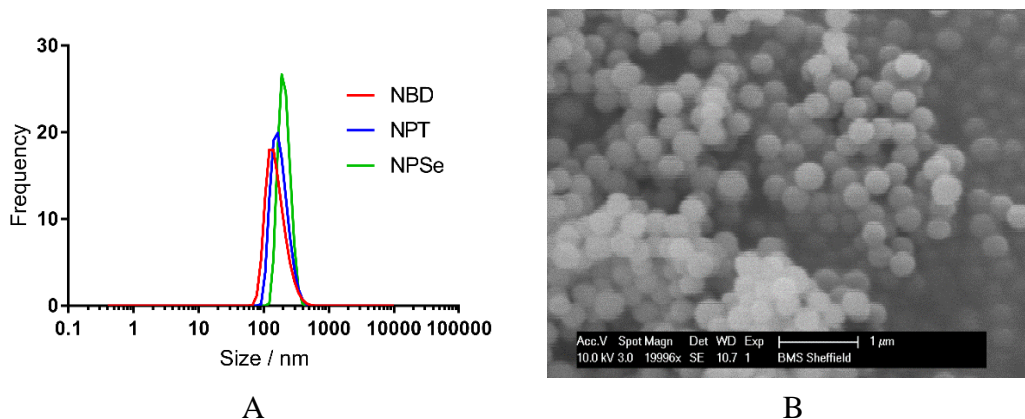


Figure 2.9 – Size analyses of dye coated nanoparticles. A) Dynamic light scattering data for particles ligated to NBD-, NPT-, and NPSe-APTES (3, 7 and 8 respectively. B) Scanning electron micrograph of nanoparticles coated with NBD-APTES (3), scale bar 1  $\mu\text{m}$ .

Attempts were made to analyse the nanoparticles by mass spectrometry. It was hoped that by bombarding the nanoparticles with high-energy entities (such as atoms in fast atom bombardment or electrons in electron impact mass spectrometry) dye molecules may have been cleaved from the particle surface to give analysable fragments and may have enabled the quantification of how many dye molecules had been ligated to the nanoparticles. This approach, however, was not successful and no useful fragments could be identified.

## 2.7 High-resolution imaging of nanoparticles

The functionalised nanoparticles were suspended in a PVA solution (40,000 MW, 1 wt% in deionised water) at a total suspended solids (TSS) concentration of 1 mg/mL before taking an aliquot of 50  $\mu\text{L}$  and dropping onto a microscopy slide and allowing to air-dry overnight. Since GLOX buffer had already been confirmed as the system that gave superior blinking activity, it was the only buffer system used to image the nanoparticles. Data were taken between 30-60 minutes after the addition of a buffer such that the buffer had had enough time to fully penetrate the PVA matrix, but not so long as to threaten the integrity of the matrix.

During acquisition, it was not possible to distinguish between a nanoparticle and a dye molecule that had leached into the surrounding area since both blink and produce a PSF at the diffraction limit. After processing the images, however, the leached molecules could be discounted as noise and nanoparticles loaded with a high density of fluorophores could be observed as separate entities (Figure 2.10).

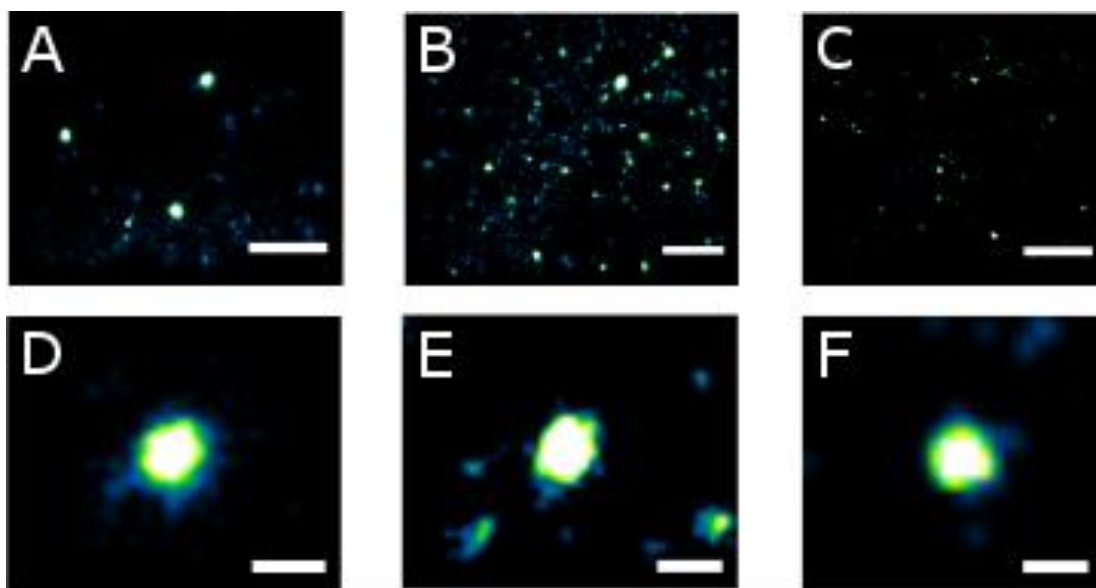


*Figure 2.10 – Reconstructed STORM wide field (1.0  $\mu\text{m}$  scale, A-C) and close-up (0.2  $\mu\text{m}$  scale, D-F) images of silica nanoparticles coated with NBD- (3, A, D), NPT- (7, B, E), and NPSe-APTES (8, C, F)*

As observed in the solution phase bleaching experiments, nanoparticle bound NBD-APTES (3) stopped photoswitching and showed a dramatic increase in fluorescence intensity with continued exposure throughout data acquisition, even at low laser power. Because of this it was only possible to capture images of nanoparticles coated with the oxygen derivative in sparsely populated areas of the sample. Again, this effect was not observed with the sulfur and selenium derivatives.

## 2.8 Conclusions

In summary, disruption of the aromatic systems by the introduction of larger atoms in this series of dye molecules gave rise to distortions in the five-membered heteroaromatic ring which, when combined with increasing orbital size and poorer orbital overlap, resulted in significant changes in the photophysical properties of the dyes.

Integral properties such as extinction coefficient, quantum yield and excited state lifetime were all reduced in dyes containing heavier atoms. These properties correlated with the observed photoblinking behaviour. Blinking density of the two buffer systems tested was lower in GLOX buffer for NBD-APTES (**3**), but higher for NPT- and NPSe-APTES (**7** and **8**, respectively), since the heavy atom stabilisation afforded by the presence of sulfur and selenium meant those dye molecules were less likely to blink unless in an environment in which they are encouraged to do so. The oxygen containing dye has the most long-lived excited state lifetime, meaning that it is more likely to exhibit fluorescence than to exist in its dark state, however, it would appear that this compound has the least accessible dark state and transition to the dark state is hindered by the addition of GLOX buffer, rather than helped.

With regards to the suitability of the dyes for SMLM imaging, the fast blink rate of the oxygen containing NBD-APTES (**3**) is actually its downfall. Although in this study it was possible to analyse individual blinking molecules, this is only because they were present in the sample at only very low concentrations. In reality, when attempting to image densely labelled samples (as is required to attain high quality SMLM images), too many molecules exist in their 'on' states simultaneously and as such individual molecules cannot be localised. This factor, along with the increased fluorescence intensity with prolonged laser exposure, makes NBD a poor candidate for use in STORM.

The slower blink rates of NPT- and NPSe-APTES (**7** and **8**, respectively), make them more suited for purpose, however, due to the ease of synthetic manipulation of the sulfur containing NPT dye, the organosulfur compound would be much more amenable for widespread use as an SMLM dye.

However, although the work in this chapter did provide a valuable insight into an interesting set of dyes, there may be little practical use for the dyes in question. They are not useful for imaging in *S. aureus* cells due to photoblinking of cellular components that would interfere with the signals from dye molecules. Indeed, at such low absorption wavelengths this would likely be the case in many cell types. If the absorption maxima for the dyes could be increased (e.g. by including elements from other groups of the periodic table in the 2-position) their practicality could be improved.



### 3 Rhodamine synthesis and analysis

Continuing the theme of atomic substitution, a range of rhodamine dyes were synthesised incorporating various p-block elements at the 10 position of the xantheno moiety in order to gauge the effect on photophysical properties and suitability for SMLM techniques.

#### 3.1 Rhodamines in the literature

Rhodamines are commonly attributed to be the first class of fluorescent molecule discovered and were in fact synthesised by accident. Fluorescein (Figure 3.1, **22**), so named because of its bright green colour in aqueous or alcoholic solutions, was first synthesised in 1871 by Adolf van Baeyer *via* the condensation of resorcinol and phthalic anhydride.<sup>144</sup> In the decades proceeding this discovery, the first rhodamine dyes were synthesised by industrial chemist Ceresole in 1887. This report showed in particular the condensation of 3-(*N,N*-dimethylamino)phenols with phthalic anhydride to give a pink, very brightly fluorescent dye that was named *N,N,N',N'*-tetramethylrhodamine (TMR, Figure 3.1, **23**).<sup>145</sup> Fluorescein and TMR are structures upon which many of the commonly used modern dyes are based upon (e.g. AlexaFluor555, TAMRA, FITC, Texas Red) due to their favourable properties including high quantum yields, and absorption and emission maxima that can be easily tuned.<sup>146</sup>

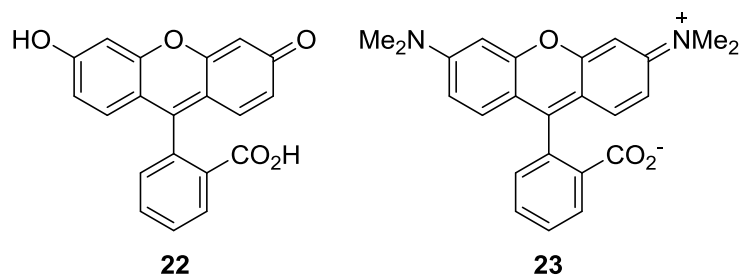
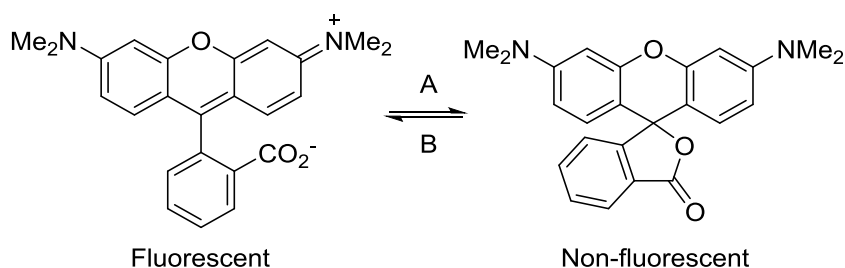


Figure 3.1 – The structures of fluorescein (**22**) and TMR (**23**).

The dyes are known to be versatile scaffolds for a variety of biological probes,<sup>147,148</sup> including cellular stains,<sup>149,150</sup> reversible<sup>151,152</sup> and irreversible<sup>153,154</sup> indicators, fluorogenic enzyme substrates,<sup>155,156</sup> and photoactivatable dyes.<sup>157–160</sup> They can be modified to include groups as handles for functionalisation, most commonly on the benzene moiety (e.g. using *N*-hydroxysuccinimide esters or isothiocyanates), however in most cases it is preferable to keep the carboxylic acid (or carboxylate) intact so that the molecules can retain their photoswitchable properties. The dyes can be controllably switched between a fluorescent ring open form and a non-fluorescent ring closed form by varying the pH or the solvent in which the dye is dissolved (Scheme 3.1). The dyes can be switched from their fluorescent ring open form to its non-fluorescent spirolactone form by raising the pH above neutral, or by dissolving it in an aprotic solvent. Similarly, the reverse process can take place by using a polar protic solvent or by adding acid to a solution of the spirolactone.<sup>161,162</sup>



*Scheme 3.1 – TMR being switched from its fluorescent to its non-fluorescent form by either raising the pH or by using an aprotic solvent (A), and back again by either lowering the pH or using a polar protic solvent (B).*

Absorption and emission maxima can be tuned across the visible spectrum by varying the nature of the alkyl group on the dialkylaniline moieties and/or modification of the xanthene ring system. TMR (**23**) exhibits a 29 nm bathochromic shift compared to its *N,N'*-dimethyl analogue (Figure 3.2, **24**), which is again shifted towards the red end of the spectrum by 22 nm compared to the unalkylated variant (Figure 3.2, **25**).<sup>146</sup> Fusing

the nitrogen substituent with the xanthene ring (Figure 3.2, **26**) gives an even more profound shift towards the red end of the spectrum by 42 nm.<sup>163</sup>

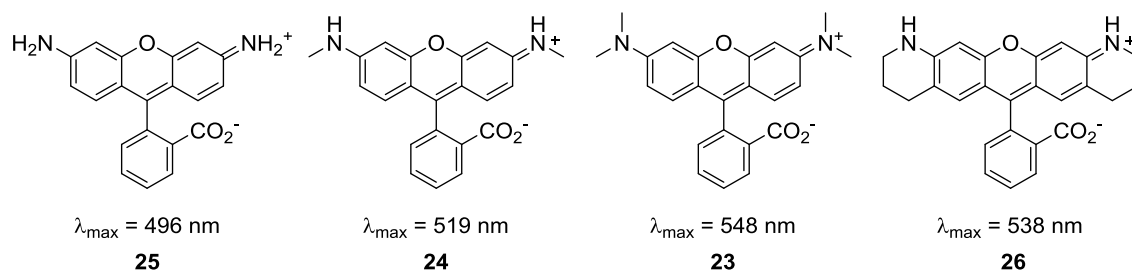


Figure 3.2 – Increasing levels of N-alkylation causes bathochromic shifts in rhodamine dyes.

Substitutions can be made onto the xanthene ring such as halogenation (Figure 3.3, **27**) or the addition of solubilising sulfonate groups (AlexaFluor 555, Figure 3.3, **28**) and this can have a modest effect on the absorption wavelength, but much more extreme shifts can be observed by changing the heteroatom at position 10 of the xanthene system.<sup>164–171</sup> The absorption maximum of carborhodamine (Figure 3.3, **29**) is increased by 56 nm, and substitution for a geminal dimethyl silicon group (Figure 3.3, **30**) gives a further bathochromic shift of 36 nm.<sup>146</sup>

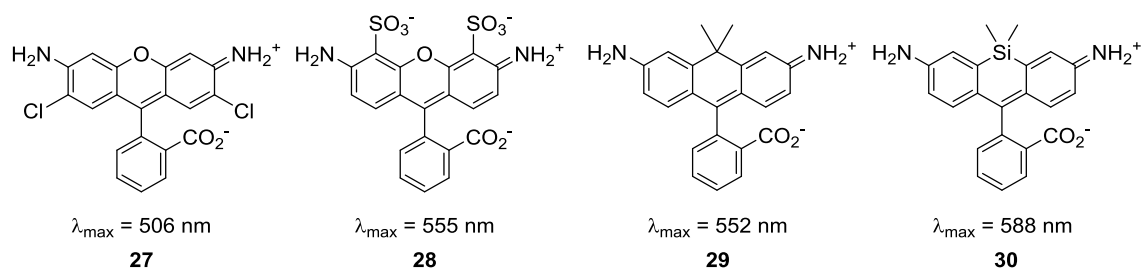
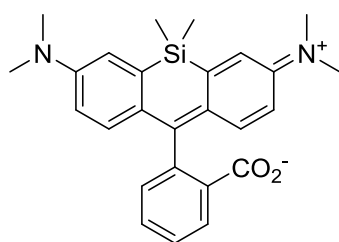


Figure 3.3 – Modifications to the xanthene system cause bathochromic shifts in rhodamine dyes.

These effects are additive and can be exploited at the same time to give fluorophores such as Si-TMS (also known as SiR, Figure 3.4, **31**) which has a far-red absorption maximum of 643 nm (147 nm longer than that of the unalkylated oxygen variant).<sup>168</sup> Rhodamine

dyes containing atoms other than oxygen do tend to have lower absorptivity in water though, since they have a higher propensity to spend more time as the non-fluorescent spirolactone forms.<sup>172</sup> This shift in equilibrium increases cell permeability and can be used as an advantage to create dyes that only emit when bound to their intended target. Because of this, SiR is used more in SMLM imaging than any other rhodamine structure.



$\lambda_{\text{max}} = 643 \text{ nm}$

**31**

Figure 3.4 – The structure and absorption maximum of SiR (**31**).

Though TMR and SiR have both been used in SMLM imaging,<sup>163</sup> many other atomic substitutions have been made in the xanthene moiety, though not studied in the context of super-resolution microscopy. This work aims to compare rhodamines containing different heteroatoms with a view of their potential use in SMLM. To avoid having to manage the equilibrium between the open and closed forms, the benzyl carboxylate ion will be substituted for a methyl group. This approach will also aid in the measurement of photoblinking activity for each dye, since removing the carboxylate moiety ensures that blinking is the sole cause of any on/off switching observed. The methyl group will also help to maintain the geometry of the molecules, such that the pendant aromatic group is held perpendicular to the xanthene moiety and excluded from the conjugated system.

A major limitation in the development of atomically substituted xanthene dyes has been the synthetic strategies used to make them which have been, to date, inefficient and laborious. The traditional approach (Route 1, Figure 3.5) utilises an anthrone-type

electrophile (**32**) and a metalated aryl species (**33**) to install the pendant aryl ring of the resulting rhodamine system. This method is, however, inefficient due to electron donating substituents on the flanks of the anthrone substrate making the ketone electron-rich and decreasing electrophilicity. Conversely, the nucleophile is often electron-poor as a result of the *ortho*- and/or *para*-ester substituent required for functionalisation and labelling specificity, reducing nucleophilicity. As a result, the electronics of the reacting partners are mismatched and syntheses often employ the use of harsh reagents such as *t*-butyllithium and have poor scalability.

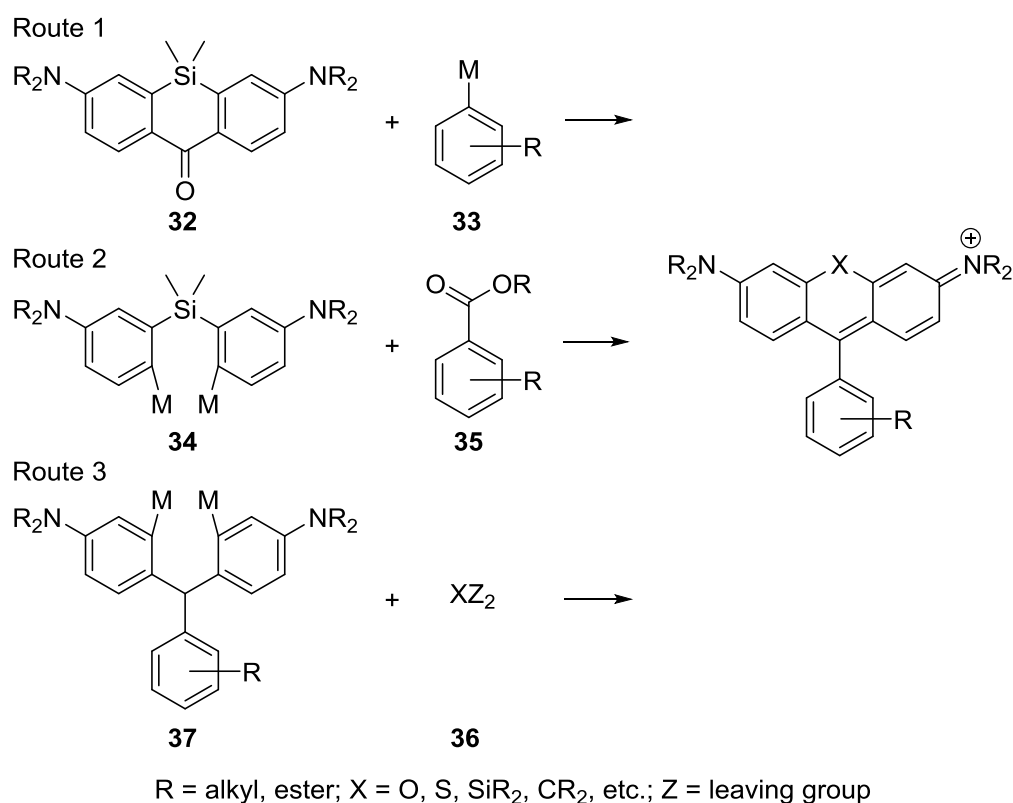


Figure 3.5 – Synthetic strategies for producing non-oxygenic rhodamine dyes.

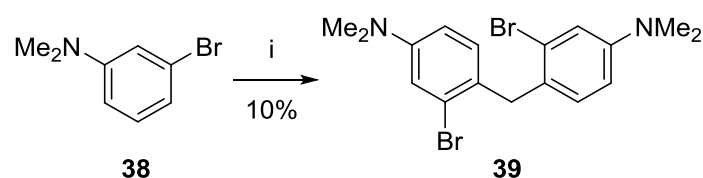
An alternate synthesis (Route 2, Figure 3.5) was recently published by Grimm, and co-workers in which the electronics of the reacting partners are reversed. This modification uses an electron-rich *bis*-metalated nucleophile (**34**) to attack an electron-poor aryl ester

electrophile (**35**). In this case the electronics of the reacting partners are matched, enabling the use of less harsh reagents under more scalable conditions. Although this strategy can be used to divergently synthesise rhodamine dyes with varied pendant aryl groups, the nucleophilic xanthene precursor must be synthesised under different conditions for every atomic variant at the 10 position of the resulting xanthene dye.

An alternate synthesis is proposed (Route 3, Figure 3.5), in which an electrophilic source of the desired heteroatom (**36**) is reacted with a *bis*-metalated xanthene precursor within which the aryl pendant is already installed (**37**). In the simplest case, this precursor can be synthesised in one high-yielding Friedel-Crafts reaction. Although the electronics of the reacting partners are not as well matched as in route 2, this route allows for any number of heteroatomic variants to be synthesised so long as an appropriate electrophile can be purchased or prepared. This method has been exploited by several researchers to synthesise a range of non-oxygenic TMR derivatives (including phosphorus, bismuth, and others),<sup>173,174</sup> but has not been used to divergently synthesise a range of dyes.

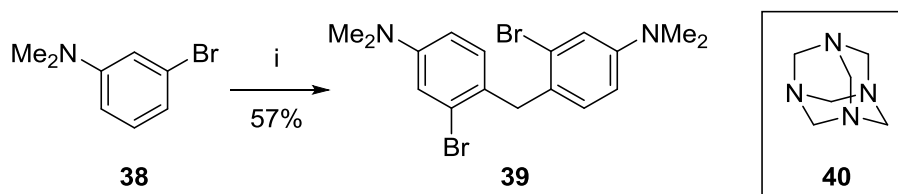
### 3.2 Dye synthesis

Variants of TMR containing different heteroatoms are most often synthesised by first condensing two molecules of 3-bromo-*N,N*-dimethylaniline (**38**) with formaldehyde to form a methylene bridge (**39**, Scheme 3.2).



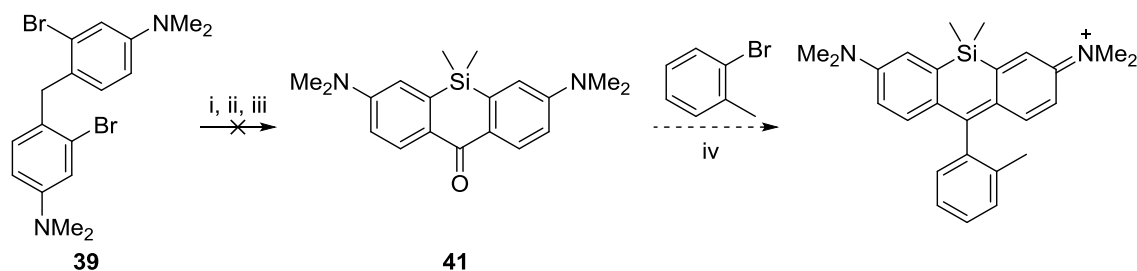
Scheme 3.2 – Synthesis of bis aryl bromide **39** using formaldehyde solution. i)  $\text{H}_2\text{CO}$  (37% w/v in  $\text{H}_2\text{O}$ ),  $\text{AcOH}$ , 60 °C, 30 min, 10%.

The yield of this reaction was poor, so in an attempt to improve it an alternate source of formaldehyde was used. When hexamethylenetetramine (**40**) was used as the source of formaldehyde, there was a substantial increase in yield to 57% (Scheme 3.3).



Scheme 3.3 – Synthesis of bis-aryl bromide **39** using hexamethylenetetramine (**40**). i) AcOH, **40**, 60 °C, 24 h, 57%.

With the *bis*-aryl bromide (**39**) in hand, subsequent functionalisation was attempted. When the traditional route (Route 1, Figure 3.5) was attempted using Me<sub>2</sub>SiCl<sub>2</sub> as the electrophile the first step was unsuccessful (Scheme 3.4). Despite the reaction being well precededented, the reaction failed in our hands, and no organic material could be isolated after the reaction was worked up despite the consumption of the starting material.

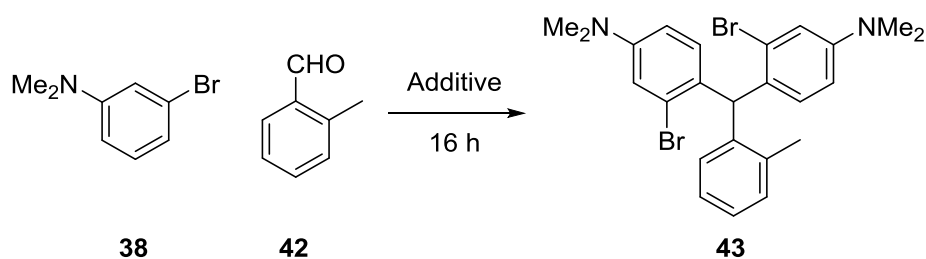


Scheme 3.4 – Attempted synthesis of ketone **41** and subsequent reaction. i) *s*-BuLi, THF, 78 °C. ii) Me<sub>2</sub>SiCl<sub>2</sub>, -78 °C – rt. iii) KMnO<sub>4</sub>, acetone, -15 °C, 2 h.

Since this approach was ineffective, the synthesis was approached via the new, proposed synthesis (Route 3, Figure 3.5), and if it was not possible to add the *o*-tolyl moiety at the end of the synthesis it would instead be added at the start. Initial attempts at condensing the bromide (**38**) with 2-methylbenzaldehyde (**42**) were not particularly fruitful under

various conditions (using *p*-toluenesulfonic acid monohydrate [PTSA.H<sub>2</sub>O] in toluene, with and without using molecular sieves, or using 1 M HCl as solvent) that had been documented in the literature,<sup>173,175</sup> so a range of Lewis acids were trialled. Of the three Lewis acids used (Bi[NO<sub>3</sub>]<sub>3</sub>.5H<sub>2</sub>O, AlCl<sub>3</sub>, and TiCl<sub>4</sub>), only titanium(IV) chloride enabled the reaction to proceed, with a good conversion of 61%.

Table 3.1 – Reaction optimisation for the condensation of aryl bromide **38** and aldehyde **42**.



| Entry          | Solvent   | Volume / mL | Additive (X)   | Eq. X | Temp / °C  | Conversion / % <sup>a</sup> |
|----------------|-----------|-------------|--|-------|------------|-----------------------------|
| 1              | PhMe      | 5           | PTSA.H <sub>2</sub> O                                | 1     | rt         | 3                           |
| 2 <sup>b</sup> | PhMe      | 10          | PTSA.H <sub>2</sub> O                                | 1     | rt         | 0                           |
| 3 <sup>c</sup> | HCl (2 M) | 10          | -  | -     | rt         | 0                           |
| 4              | DCM       | 2           | Bi(NO <sub>3</sub> ) <sub>3</sub> .5H <sub>2</sub> O | 1     | rt         | 0                           |
| 5              | DCM       | 2           | AlCl <sub>3</sub>                                    | 1     | rt         | 0                           |
| 6              | DCM       | 2           | TiCl <sub>4</sub>                                    | 1     | rt         | 61                          |
| 7              | DCM       | 2           | TiCl <sub>4</sub>                                    | 1     | 50         | 85                          |
| 8 <sup>d</sup> | DCM       | 2           | TiCl <sub>4</sub>                                    | 1     | - 78 to rt | 35                          |
| 9              | DCM       | 10          | TiCl <sub>4</sub>                                    | 1     | rt         | 63                          |
| 10             | DCM       | 2           | TiCl <sub>4</sub>                                    | 1.5   | rt         | 36                          |

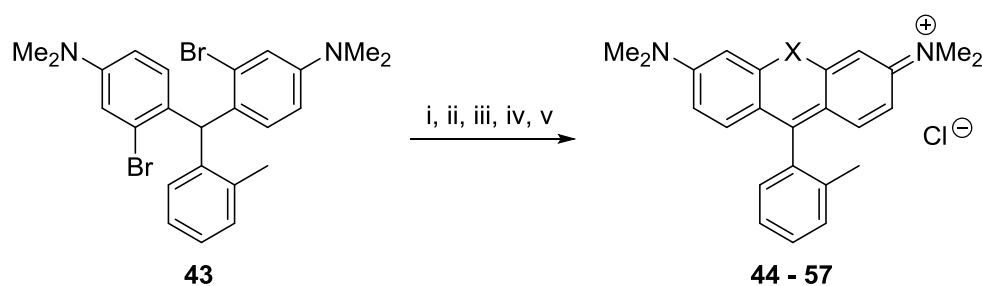
<sup>a</sup> Calculated by comparison of appropriate peaks in the <sup>1</sup>H NMR spectrum. <sup>b</sup> Using 4Å molecular sieves. <sup>c</sup> Reaction time of 3 days. <sup>d</sup> Aldehyde and TiCl<sub>4</sub> pre-mixed at -78 °C before adding the aryl bromide and allowing to return to room temperature.

At this stage the reaction was optimised and it was found that heating the reaction at reflux gave the best conversion (Table 3.1), however under these conditions (Entry 7) the solvent evaporated over the course of the reaction. Since an increased solvent volume had no effect on the conversion (Entry 9), and to avoid having to use a sealed tube, the reaction



was conducted at reflux in a larger volume which, after trituration from chloroform and methanol, gave the desired dibromide (**43**) in 75% yield.

With the dibromide (**43**) in hand, it was possible to diverge and synthesise a range of rhodamine dyes containing different heteroatoms at position 10 of the resulting structure. To install the heteroatoms, the dibromide (**43**) was treated with *s*-BuLi at -78 °C before adding an electrophilic source of the desired heteroatom (**E**, Scheme 3.5).



*Scheme 3.5 – Insertion of electrophiles into position 10 of the xanthene moiety. i) s-BuLi, -78 °C, 1 h. ii) E, -78 °C – rt, 16 h. iii) HCl. iv) K<sub>2</sub>CO<sub>3</sub>. v) Chloranil.*

In this study, the inclusion of various p-block elements into position 10 of the xanthene moiety aimed to discern the effects of including atoms not only from different periods of the periodic table, but also different groups and oxidation states (Table 3.2). It was of particular interest to how the photophysical properties of these *o*-tolyl variants compared to the parent carboxylate, especially in the context of their ability to exhibit reversible photoblinking.

The methyl group of the *o*-tolyl moiety mimicked the carboxylate group used in most rhodamine syntheses by introducing steric bulk, forcing the pendant aromatic group to rest perpendicular to the plane of the xanthene rings. This ensured that conjugation could not be continued into the benzene ring, thus altering the photophysical properties of the molecules. This rotameric behaviour was observed in computational geometric optimisation (Figure 3.8, page 80).

Table 3.2 – Details of the electrophiles used in the divergent synthesis of various heteroaromatic rhodamine dyes.

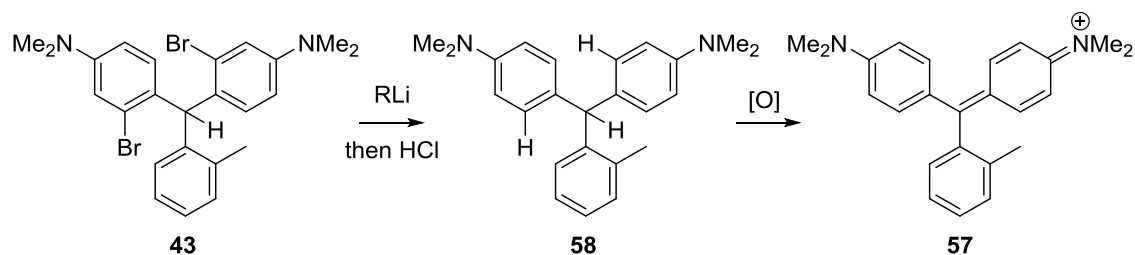
| Entry | E                                   | X (name, number)  | Yield / % <sup>a</sup> |
|-------|-------------------------------------|---|------------------------|
| 1     | B(OMe) <sub>3</sub>                 | BOMe (BOMeR, <b>44</b> )                                      | 0                      |
| 2     | Trimethyl boroxine                  | BMe (BMeR, <b>45</b> )  | 0                      |
| 3     | PhBCl <sub>2</sub>                  | BPh (BPhR, <b>46</b> )  | 0                      |
| 4     | (EtO) <sub>2</sub> CO               | C(allyl) <sub>2</sub> (CR, <b>47</b> ) <sup>b</sup>           | 0                      |
| 5     | Si(Me) <sub>2</sub> Cl <sub>2</sub> | Si(Me) <sub>2</sub> (SiR, <b>48</b> )                         | 8                      |
| 6     | Ge(Me) <sub>2</sub> Cl <sub>2</sub> | Ge(Me) <sub>2</sub> (GeR, <b>49</b> )                         | 60                     |
| 7     | Cl <sub>2</sub> NTs                 | NTs (NR, <b>50</b> )  | 0                      |
| 8     | <i>i</i> -Pentyl nitrite            | NO (NOR, <b>51</b> )  | 46                     |
| 9     | Cl <sub>2</sub> POEt                | P(OEt) (P[III]R, <b>52</b> )                                  | 0                      |
| 10    | Cl <sub>2</sub> POEt                | PO <sub>2</sub> <sup>-</sup> (P[V]R, <b>53</b> ) <sup>c</sup> | 10                     |
| 11    | SOCl <sub>2</sub>                   | S(O) (S[IV]R, <b>54</b> )                                     | 0                      |
| 12    | SO <sub>2</sub> Cl <sub>2</sub>     | S(O) <sub>2</sub> (S[VI]R, <b>55</b> )                        | 0                      |
| 13    | Davis reagent                       | O (OR, <b>56</b> )  | Trace                  |
| 14    | O <sub>2</sub> (gas)                | O (OR, <b>56</b> )  | 0                      |
| 15    | -                                   | H, H (HR, <b>57</b> )   | 57                     |

<sup>a</sup> Refers to isolated product. <sup>b</sup> After three steps. <sup>c</sup> After two steps.

In some cases it was found that the electrophile was not suitably reactive and the correct product was not observed (Table 3.2, entries 1 – 4, 7, 9, 11 – 14). After lithium-halogen exchange, instead of reacting with the electrophiles, the lithiated intermediate was quenched and protonated on work-up to give a methine containing compound (**58**). On addition of chloranil this structure was oxidised, extending the conjugated system to give a *tris*-aryl species, which will be referred to as hydrogen rhodamine (HR, **57**, Scheme 3.6), and caused the sample to turn blue.

The fact that HR exists and has similar photophysical properties to many existing rhodamine dyes (Table 3.5) may suggest that, in some cases, the heteroatom at position 10 of the xanthene structure may not be involved in the conjugated systems of the

compounds. This was also observed in computational studies of geometric optimisations (Figure 3.8, page 80). If this is the case, tuning emission wavelength using variation at position 10 may only be a result of differences in electronegativity or molecular distortion as a result of greater atomic radius.

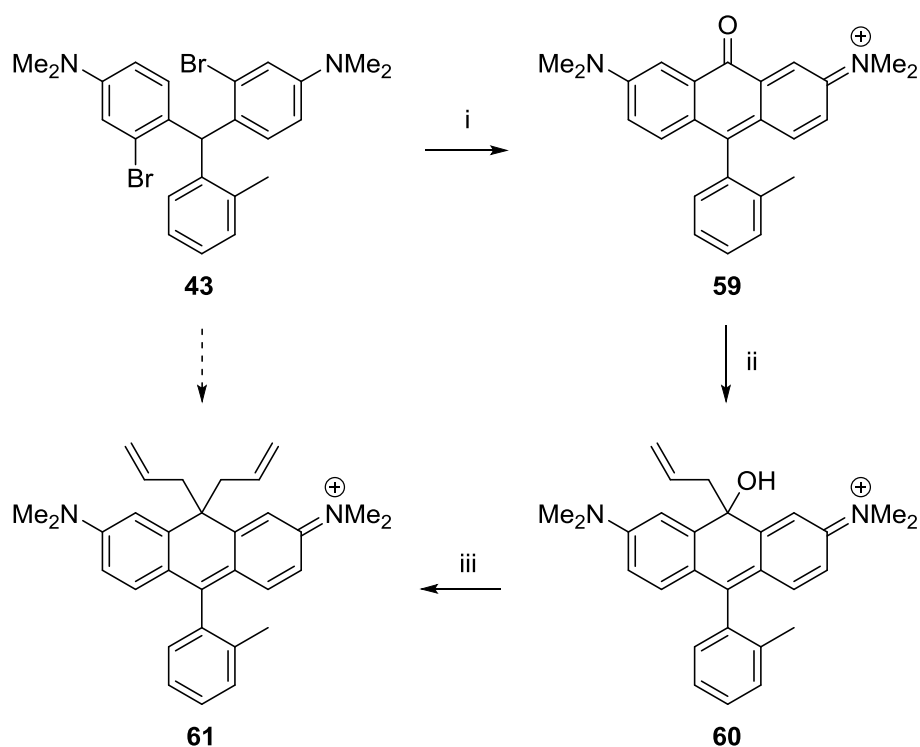


*Scheme 3.6 – Dibromide **43** is protonated after lithium-halogen exchange to tris-aryl **58**, before oxidation to lose the highlighted methine proton and give the fully aromatised species **57**.*

It was possible to observe this process using  $^1\text{H}$  NMR spectroscopy. The methine proton of the dibromide starting material (**43**) gives a singlet in the  $^1\text{H}$  NMR spectrum at 5.95 ppm and shifts to 5.51 ppm after quenching the lithiated species. After oxidation with chloranil, this peak no longer appears in the  $^1\text{H}$  NMR spectrum. These results were confirmed using high resolution mass spectrometry. Molecular ion peaks were observed at  $m/z$  501.0536, 503.0522, and 505.0503 (1:2:1 ratio,  $[\text{M}+\text{H}]^+$ ) for the dibromide starting material (**43**), at  $m/z$  344.2325 ( $[\text{M}+\text{H}]^+$ ) for the quenched, protonated lithiated species (**58**), and at  $m/z$  343.2167 for the oxidised product (**57**).

In the attempted syntheses of boron variants (Table 3.2, entries 1, 2, 3), three boron electrophiles of varying electrophilicity were trialled but none gave a positive result. Although carborhodamines have been previously synthesised *via* other routes (e.g. Figure 3.3, **29**),<sup>148</sup> it was not possible to directly synthesise an analogue where  $\text{X} = \text{C}(\text{Me})_2$  (Table 3.2, entry 4) from dibromide precursor **43** due to a lack of suitable doubly reactive

electrophiles. The synthesis of a carbon rhodamine analogue was attempted in three steps but again was unsuccessful (Scheme 3.7).



Scheme 3.7 – Proposed three-step synthesis of  $C(\text{allyl})_2$  rhodamine (**47**). i) *s*-BuLi, then  $\text{CO}(\text{OEt})_2$ , ii) Allyl magnesium bromide. iii) Titanium(IV) tetrachloride, allyl trimethylsilane.

The carbon atom was intended to be introduced after lithium-halogen exchange of dibromide **43** using diethyl carbonate to give a ketone intermediate (**59**). Unfortunately, the initial incorporation of the carbonyl group was not possible and there was no reaction with the carbonate (as proven by mass spectrometry). In the case of both the boron and carbon rhodamine analogues, purity of the electrophiles may have been an issue, since the reagents are hygroscopic, and the presence of water could have hydrolysed the reagent or quenched the lithiated species. Due to time restrictions it was not possible to investigate other synthetic routes to the boron or carbon containing rhodamines.

It would have been beneficial to have been able to synthesise a nitrogen containing rhodamine derivative, however, *bis*-electrophilic sources of nitrogen are scarcely found. Initial attempts using *N,N*-dichloro-4-methylbenzenesulfonamide ( $\text{Cl}_2\text{NTs}$ , Table 3.2, entry 7) were not successful, and the protonated by-product (HR, **57**) was seen instead. The poor electrophilicity of the sulfonamide could be attributed to the large amount of steric bulk that exists around the nitrogen atom, blocking an attack from a hindered nucleophile such as the aryl lithium species used in this study.

The next attempt at synthesising a nitrogen-containing rhodamine used *i*-pentyl nitrite as the electrophile (Table 3.2, entry 8). Since there is much less steric congestion around the electrophilic nitrogen atom in isoamyl nitrite, an *N*-oxide moiety was successfully inserted into the xanthene structure (NOR, **51**). The structure of the acridine-like structure was determined to be an *N*-oxide. Since it was possible to obtain a proton NMR spectrum, it was unlikely to be a stable oxygen radical species (**62**) as radical species are paramagnetic, and since there was no evidence to support the presence of a hydroxylamine moiety by IR or  $^1\text{H}$  NMR spectroscopy in  $\text{d}_6$ -DMSO, it was determined that the structure was most likely to be an acridine *N*-oxide (**51**) in which the nitrogen atom is involved in the aromatic system and the compound is neutral overall, as opposed to a cationic hydroxylamine structure (**63**, Figure 3.6).

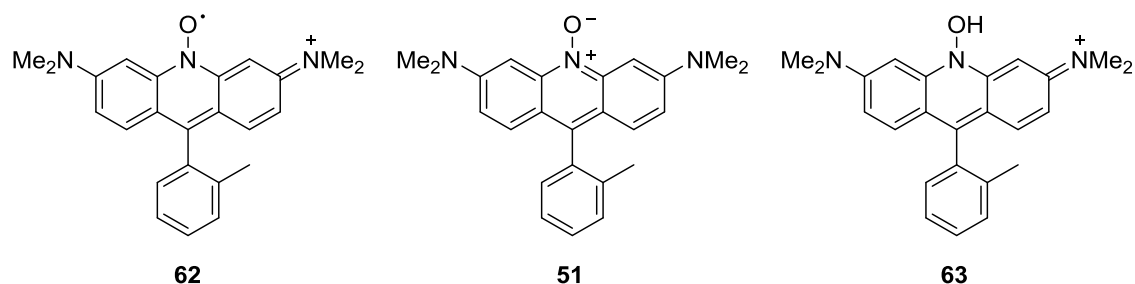
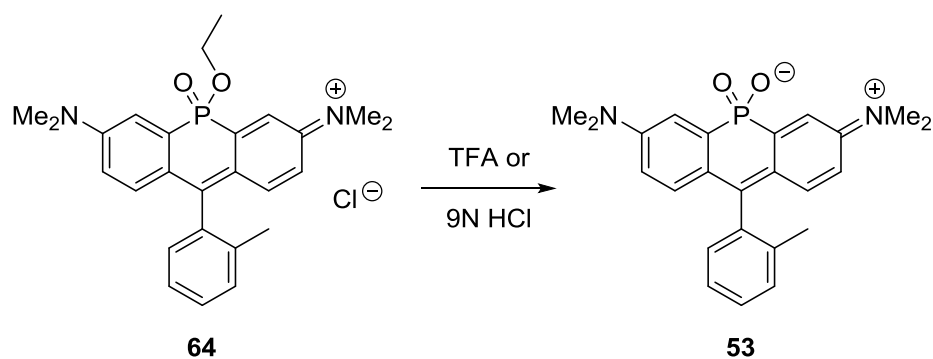


Figure 3.6 – The possible structures of NOR. From left to right: oxygen radical (**62**), *N*-oxide (**51**), and hydroxylamine (**63**).

It was noted that the colour of NOR (**51**) was red, not blue like the other successfully synthesised analogues ( $\lambda_{\text{max}}$  recorded in Section 3.3), indicating that the electronic structure may differ from the other rhodamine compounds. It appeared that the P(III) derivative (Table 3.2, **52**, entry 9) was not isolable, but the P(V) analogue (Table 3.2, **53**, entry 10) was. Despite the use of the same P(III) electrophile, to synthesise the P(V) containing xanthenes structure (**53**) an oxidation using hydrogen peroxide was required before chloranil aromatisation. Interestingly, no P(III) rhodamines have previously been reported, but P(V) rhodamines have appeared frequently in the literature since 2015.<sup>173,176–178</sup> In each of these cases, where a phosphorus electrophile was used, a P(III) reagent is inserted into the framework then oxidised to the final P(V) species before aromatisation of the xanthenes construct. It has been suggested that oxidation of the phosphorus atom to the corresponding phosphine oxide increases the chemical stability of the  $\pi$ -skeleton by offering effective conjugation between  $\sigma^*$ - $\pi^*$  orbitals.<sup>177</sup> This implies that the P(III) rhodamine was not sufficiently stable and decomposed to the protonated species HR (**57**) during work-up, which was detected using mass spectrometry.



*Scheme 3.8 – Conversion of phosphinic ester **64** to a phosphinic anion under acidic conditions.*

Interestingly, the treatment of the P(V) analogue with TFA to change the counter ion caused the ethyl group to be removed, leaving a phosphinate anion behind (Scheme 3.8),

as evidenced by  $^1\text{H}$  NMR,  $^{31}\text{P}$  NMR and mass spectrometry. This has been observed in the past when phosphinic ester **64** was treated with 9N HCl at reflux overnight.<sup>173</sup>

The synthesis of sulfur containing derivatives was attempted (Table 3.2, entries 11 and 12), using two *di*-electrophilic sulfur compounds in different oxidation states were used, however, neither of these reactions gave the desired products. It is known that some S(IV) and S(VI) chlorides can be electrophilic at the chlorine atoms.<sup>179,180</sup> In this case, continued lithium halogen exchange is possible but the lithiated species no longer has an electrophile to attack. An alternative argument could be that the sulfur atoms of each electrophile were too sterically congested, preventing attack from the bulky nucleophile. In either case, the result would be the protonated analogue, HR (**57**), which was observed when using both the sulfoxide and the sulfone electrophiles.

It was not possible to access a true rhodamine where  $X = \text{O}$  (Table 3.2, entries 13 and 14) *via* this methodology. When using the Davis reagent (Figure 3.7) trace amounts of the desired TMR analogue were detected by mass spectrometry, but not in isolable quantity. The reaction was reattempted using gaseous oxygen, however, LCMS showed no evidence that the lithiated nucleophile had reacted with oxygen gas, and HR (**57**) was isolated. In future, copper catalysis could be used to try to facilitate incorporation of an oxygen atom.<sup>181,182</sup> Since silicon rhodamines are more widely used for SMLM imaging, OR (**56**) was no longer pursued as a synthetic target.

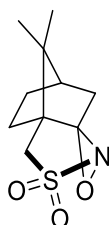
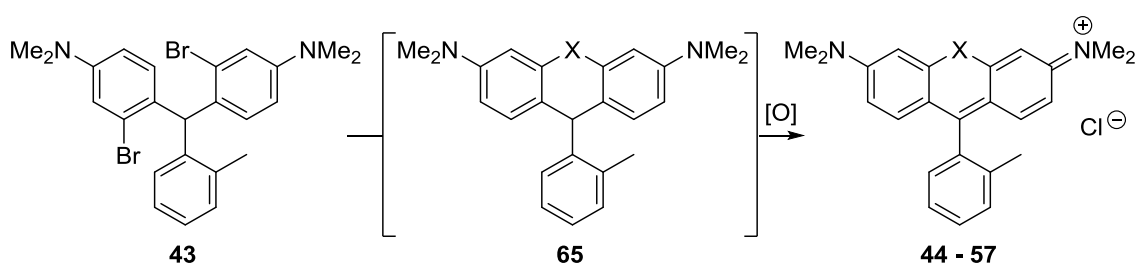


Figure 3.7 –The structure of the Davis Reagent.

A mass spectrometry study during the synthesis of the germanium analogue (**49**) showed that, although a small proportion of the fully aromatised xanthene structure had formed before the addition of chloranil, the majority of the sample existed as the intermediate in which the central ring contained a saturated carbon centre (**65**, Scheme 3.9). Further mass spectrometry analysis undertaken after reaction with chloranil showed that the majority of this intermediate had been successfully converted to the fully aromatised xanthene target compound.



*Scheme 3.9 – After reaction with an electrophile the compound exists as an intermediate which is not fully unsaturated (**65**). Further reaction with an oxidant aromatises the system.*

The counter ion in all cases was assumed to be chloride on account of the work up using hydrochloric acid. However, since the nature of the counter ion was an assumption, all compounds were converted to the trifluoroacetate salt by either stirring in a 1:1 mixture of TFA and dichloromethane for one hour, or using HPLC purification using 0.1% TFA in water as a cosolvent, conditions allowing. It was noted that, under strongly acidic conditions, all of the fluorophores changed colour from blue to orange. This colour change was reversed when the samples were evaporated to dryness. A recent study has shown that subjecting rhodamine dyes to very low pH conditions alters the emission wavelength.<sup>183</sup> With 500 equivalents of TFA the rhodamine compound went from emitting at 625 nm to 425 nm due to protonation of both aniline nitrogen atoms.



After the successful synthesis and HPLC purification of five rhodamine analogues, their photophysical properties were analysed. As with the NBD derivatives (Section 2.5), geometrically optimised structures and HOMO and LUMO energies were calculated so that they could be compared to experimental measurements, and qualities such as quantum yield ( $\Phi$ ), fluorescence lifetime ( $\tau$ ), blink rate and duty cycle were compared to existing dyes used for SMLM imaging in order to determine how suitable each dye is for localisation microscopy.

### 3.3 Computational studies and solution phase analysis

In order to predict the photophysics of the heteroaromatic analogues, computational studies were conducted in which the geometry of each successfully synthesised dye was optimised (Figure 3.8) before calculating the energies of the HOMO and LUMO molecular orbitals (Table 3.4). The structure and molecular orbital energies of the oxygen containing rhodamine were also calculated for comparison. The methods and basis sets used to perform the calculations were identical to those detailed for the benzodiazole series of compounds (Section 2.5).

Interestingly, when the structures were optimised the heteroatom at position 10 of the xanthene moiety did not appear to be involved in the dyes' conjugated systems (Figure 3.8). Although the CX bond lengths for the first row elements (CO 1.36 Å in OR, and CN 1.38 Å in NOR) correlated well with documented bond lengths of similar aromatic species (CO 1.368 Å in furan, and CN 1.384 Å in pyridinium *N*-oxide),<sup>184,185</sup> the second row elements tended to have longer bonds more similar in length to CX single bonds.

In SiR (**48**) the CSi bonds were calculated to have an average length of 1.88 Å which is more similar to the C-Si single bond length of 1.89 Å than the C=Si bond length or the aromatic CSi bonds in silabenzene (1.70 Å and 1.77 Å, respectively).<sup>186</sup> Similarly the

CGe bonds in GeR (**49**) were calculated to have an average length of 1.96 Å which correlates to a C-Ge single bond (1.98 Å).<sup>187</sup>

The CP bonds in the phosphorus derivative (P[V]R, **53**) were calculated to have an average length of 1.81 Å, which is again much closer to the C-P single bond length of 1.84 Å than the C=P double bond length (1.64 Å) or the aromatic CP bonds in a phosphorine compound (1.75 Å).<sup>186,188</sup> These calculations support the hypothesis that the heteroatom at position 10 of the xanthene structure may not always be involved in the conjugated systems of rhodamine dyes.

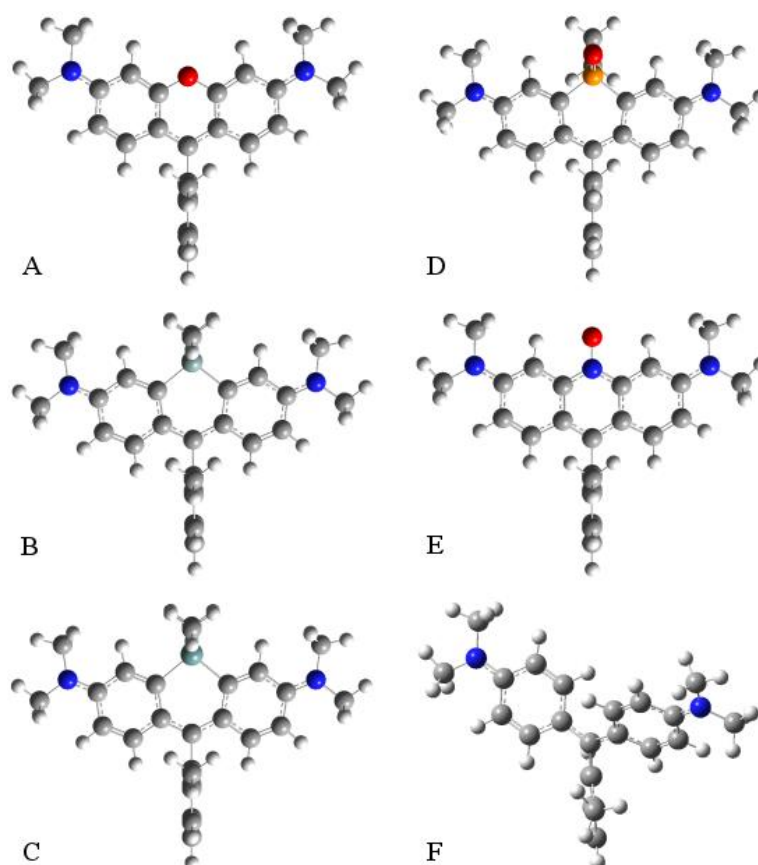


Figure 3.8 – Geometrically optimised structures of xanthene based dyes as viewed in the same plane as the conjugated system. A) X = O (**56**), B) X = Si(Me)<sub>2</sub> (**48**), C) X = Ge(Me)<sub>2</sub> (**49**), D) X = PO<sub>2</sub><sup>-</sup> (**53**), E) X = NO (**51**), F) X = H, H (**57**).

It was noted that as atomic radius increased, there was significant distortion in the molecules to accommodate them. Elements from the first row of the periodic table fit well into a regular hexagonal structure (Figure 3.8A and E), but elements from the second row (e.g. silicon and phosphorus, Figure 3.8B and D, respectively) produced large distortions. When an element from the third row was included (germanium, Figure 3.8C), there was distortion of the central ring, but of approximately the same magnitude as the second row elements. These distortions were quantified in terms of the C-X-C bond angle and the average C-X bond length to measure the degree of distortion to accommodate larger atoms (Table 3.3).

It was also evident, when viewing the molecules by looking down at the heteroatom (Figure 3.9), that as well as distorting the ring system outwards towards the dimethylamino moieties, some atoms sat out of the plane of the conjugated system. Although most of the structures remained planar, this effect was very pronounced in the structure of P(V)R (**53**, Figure 3.9E) and was quantified by measuring the average C-C-C-X dihedral angle (Table 3.3).

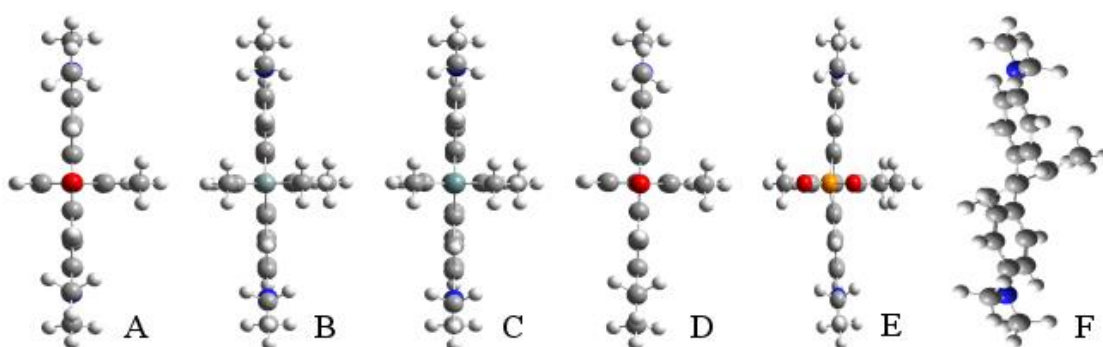


Figure 3.9 – Geometrically optimised structures of xanthene based dyes as viewed looking down at the heteroatom in position 10. A) X = O (**56**), B) X = Si(Me)<sub>2</sub> (**48**), C) X = Ge(Me)<sub>2</sub> (**49**), D) X = NO (**51**), E) X = PO<sub>2</sub><sup>-</sup> (**53**), F) X = H, H (**57**).

There is an even more drastic staggering of the protonated species (HR, **57**, Figure 3.9F), in which the dihedral angle is 26.76°. The twisting observed in this molecule avoids steric

clash and accommodates the protruding C-H bonds, but is kept to a minimum so that conjugation is still possible between the two aniline rings. Effective conjugation in torsionally strained compounds has been recorded experimentally in the literature at angles of up to 54.7°,<sup>120,189</sup> and one model calculates an upper bound of 80° for conjugation between non-linear conjugated systems.<sup>190</sup>

Table 3.3 – Measurements of the geometrically optimised rhodamine structures.

| Entry | Compound            | Avg. C-X bond length / Å <sup>a</sup> | C-X-C bond angle / ° <sup>a</sup> | Avg. C-C-C-X dihedral angle / ° <sup>a</sup> |
|-------|---------------------|---------------------------------------|-----------------------------------|--|
| 1     | OR ( <b>56</b> )    | 1.36                                  | 121.23                            | 0.06   |
| 2     | SiR ( <b>48</b> )   | 1.88                                  | 102.74                            | 0.03   |
| 3     | GeR ( <b>49</b> )   | 1.96                                  | 101.08                            | 0.09   |
| 4     | NOR ( <b>51</b> )   | 1.38                                  | 120.46                            | 0.13   |
| 5     | P(V)R ( <b>53</b> ) | 1.81                                  | 103.81                            | 4.68   |
| 6     | HR ( <b>57</b> )    | -                                     | -                                 | 26.76  |

<sup>a</sup> Calculated using Gaussian 09 using DFT theory with a B3LYP 6311g (d,p) basis set.<sup>135</sup>

Like the benzodiazole dyes (Table 2.3, Section 2.5), the calculated  $\lambda_{\max}$  for the rhodamine dyes in this series were shorter than the experimentally measured values but were predicted in the correct order. The percentage of hybrid functional (HF) exchange (used to approximate an ab initio calculation to save on computation time in which electrons are expressed in terms of orbitals rather than density) is low in the B3LYP basis set which limits the accuracy of the calculated eigenvalues.<sup>191</sup> It was predicted that the *N*-oxide rhodamine (NOR, **51**) would have a significantly lower absorption wavelength than the other rhodamine derivatives, that the silicon containing rhodamine (SiR, **48**) would absorb at a lower wavelength when compared to the other dyes, and that the P(V) rhodamine (P[V]R, **53**) would absorb at the longest wavelength. The major component of all  $S_0 - S_1$  transitions was attributed to a HOMO – LUMO transition.

Table 3.4 – Calculated energies of the geometrically optimised rhodamine structures, as compared to experimental values.

| Entry | Compound            | HOMO – LUMO difference / eV <sup>a</sup> | Calculated $\lambda_{\text{max}}$ / nm <sup>a</sup> | Calculated oscillator strength | Experimental $\lambda_{\text{max}}$ / nm <sup>b</sup> |
|-------|---------------------|--|---|--------------------------------|---|
| 1     | SiR ( <b>48</b> )   | 2.7448                                   | 568   | 1.2868                         | 530   |
| 2     | GeR ( <b>49</b> )   | 2.5007                                   | 560   | 1.3365                         | 633   |
| 3     | NOR ( <b>51</b> )   | 3.0126                                   | 436   | 0.0716                         | 467   |
| 4     | P(V)R ( <b>53</b> ) | 2.3328                                   | 602   | 1.1171                         | 666   |
| 5     | HR ( <b>57</b> )    | 2.5500                                   | 552   | 1.2739                         | 618   |

<sup>a</sup> Calculated using Gaussian 09 using TD-SCF DFT theory with a B3LYP 6311g (d,p) basis set and was solved for N=100 states.<sup>135</sup> <sup>b</sup> Measured in water.

The absorption maxima (Table 3.5, Figure 3.10A) of GeR, P(V)R, and HR (**49**, **53**, and **57**, respectively) were in the red region of the visible spectrum, as expected, and were close to, if not exactly the same, as those documented in the literature. GeR (**49**) had a measured absorption maximum of 633 nm compared to a literature value of 635 nm,<sup>70</sup> and P(V)R (**53**) had a measured absorption of 666 nm which is identical to the literature value.<sup>173</sup> The measured absorption maximum of 618 nm for HR (**57**) was identical to the recently published data for the compound with a chloride counter-ion.<sup>192</sup> The oscillator strength of the S<sub>0</sub> – S<sub>1</sub> transition for NOR (**51**) was calculated to be vastly lower than those of the other rhodamine analogues, and this is reflected in the experimentally measured molar extinction coefficient (Table 3.5).

Although the structure of the silicon containing analogue SiR (**48**) had been verified as correct using spectroscopic analysis and the purity from HPLC purification and LCMS, it was puzzling that the measured absorption curve (with a maximum of 530 nm), had the right shape, but the absorption maximum was much shorter than the maximum previously reported in the literature (646 nm).<sup>70</sup> One potential reason for this would be that the

spectral measures in this study were taken in water, whereas in the literature spectra had been reported in phosphate-buffered saline (PBS) with 0.1% DMSO. In this case, however, it would also be expected that the spectral measurements for GeR (**49**) would be shifted since the published measurements were also taken in PBS.<sup>70</sup> However, the reported absorption maxima does vary in previously published articles, and has been reported to be as low as 500 nm.<sup>170</sup> This difference may be due to the dye existing in an alternative structure before absorption, which transforms to the ‘classical’ SiR structure after photon absorption. This is supported by an excitation maximum in line with the published absorption maxima for the dye (Figure 3.10C).

The fact that the absorption maximum of NOR (**51**) was so much lower than those of the other rhodamine analogues further reinforces a vastly different electronic structure. The absorption curve for this compound was also differently shaped to the other rhodamine analogues (Figure 3.10A). The measured absorption maximum of the *N*-oxide (**51**) was 467 nm and was measured in water. This value is similar to an acridine *N*-oxide whose absorption maximum was measured to be 438 nm in both THF and acetonitrile.<sup>193</sup>

Table 3.5 – Summary of photophysical measurements of the five rhodamine derivatives.

| Entry | Compound            | $\lambda_{\text{max}} / \text{nm}^{\text{a}}$ |     | $\epsilon / \text{M}^{-1}\text{cm}^{-1 \text{b}}$ | $\Phi / \%^{\text{c}}$ | $\tau / \text{ns}^{-1 \text{d}}$ |
|-------|---------------------|---|-----|---|------------------------|----------------------------------|
|       |                     | Abs   | Em  |   |                        |                                  |
| 1     | SiR ( <b>48</b> )   | 530   | 678 | 120,000   | 7.9                    | 2.19                             |
| 2     | GeR ( <b>49</b> )   | 633   | 651 | 48,000  | 0.7                    | 4.13                             |
| 3     | NOR ( <b>51</b> )   | 467   | 556 | 2,500   | 93.3                   | 3.95                             |
| 4     | P(V)R ( <b>53</b> ) | 666   | 702 | 18,000  | 14.0                   | 3.78                             |
| 5     | HR ( <b>57</b> )    | 618   | 652 | 44,000  | 5.3                    | 1.85                             |

<sup>a</sup> Absorption and emission were measured using 100 mm solutions. <sup>b</sup> Molar extinction coefficients were extrapolated from calibration curves plotted using solutions with concentrations between 10–100 mm and are correct to two significant figures. <sup>c</sup> Quantum yield measurements taken using an integration sphere and compared to BODIPY-Br with a quantum yield of 7.5%. <sup>d</sup> Excited state lifetime measurements were taken using a time-correlated single photon counting method for time-resolved photoluminescence.

Despite the discrepancy between the measured and the literature absorption maximum for SiR (**48**), the measured emission maximum (Table 3.5, Figure 3.10B) for the compound (678 nm) is closely matched to the previously documented value (660 nm). The emission maxima of GeR and P(V)R (651 and 702 nm, **49** and **53**, respectively) were similar to the values reported for those compounds in the literature (649 and 685 nm, respectively).<sup>70,173</sup>

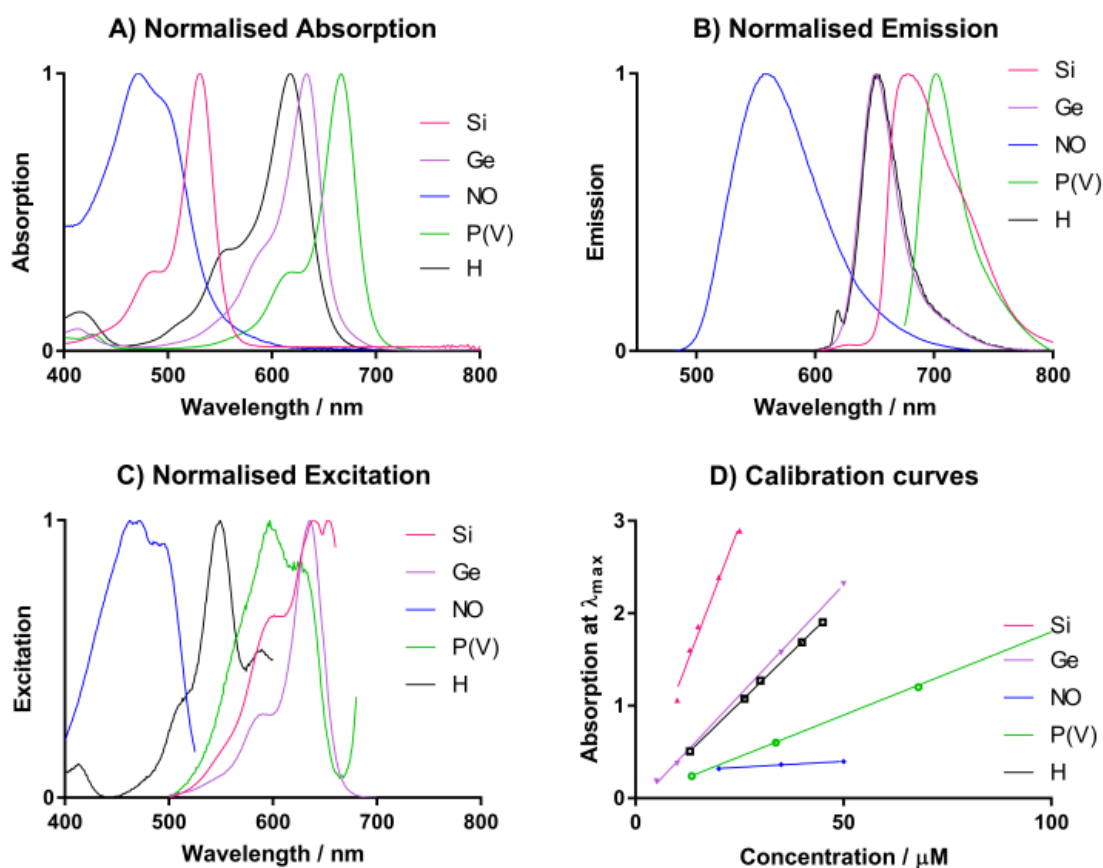


Figure 3.10 – Photophysical measurements of the five synthesised rhodamine dyes. A) Normalised absorption spectra, B) Normalised emission spectra, C) Normalised excitation spectra, D) Calibration curves used to calculate molar absorption coefficient.

There did not appear to be a trend in the molar extinction coefficients of the various rhodamine dyes (Table 3.5, Figure 3.10D). The value calculated for SiR (**48**) was particularly high compared to the other analogues, but was in line with values previously

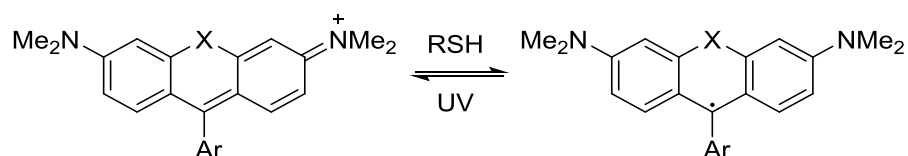
stated in the literature.<sup>170,171</sup> Conversely, the calculated extinction coefficient for NOR (**51**) is much lower than the other rhodamines.

As with the benzodiazole series, dyes with heavier atoms in their aromatic system had lower quantum yields (e.g.  $\phi_{\text{SiR}} = 7.9\%$  and  $\phi_{\text{GeR}} = 0.7\%$ ). This can, again, be attributed to the heavier atom increasing the probability of transfer of an excited electron to the triplet state *via* intersystem crossing. It was noted that, despite having a much lower molar extinction coefficient, the quantum yield for NOR (**51**) was particularly high at 93.3%. This, again, suggests the electronic structure of the dye is vastly different to the other rhodamine analogues (since it is preferable for an excited electron to radiatively decay, rather than undergo intersystem crossing to another electronic state).

Again, there was no trend in the values measured for the excited state lifetimes of the five molecules (Table 3.5). The values of the molecules were, however, all very similar, suggesting that they share similar properties (e.g. blink rate) under SMLM conditions. The excited state lifetimes of SiR and HR (**48** and **57**, respectively) were measured to be approximately half of the measured values for the other three derivatives. A less stable excited state (indicated by a shorter excited state lifetime) may be indicative of a faster blink rate, as these molecules may be more likely to transition to their dark state.

SiR, GeR, P(V)R, and HR (**48**, **49**, **53** and **57**, respectively) were all photostable to continued laser irradiation at 100 mW for 1 hour (Figure 3.11). On the addition of  $\beta$ -mercaptoethylamine (MEA), fluorescence was quenched, and only the brightest dyes (SiR and GeR, **48** and **49**, respectively) exhibited detectable fluorescence (Figure 3.11A, B). This loss of fluorescence intensity was attributed to the formation of a stable, non-fluorescent tertiary radical species (Scheme 3.10), whose stability stems from being alpha to three aromatic systems.<sup>60,194,195</sup>

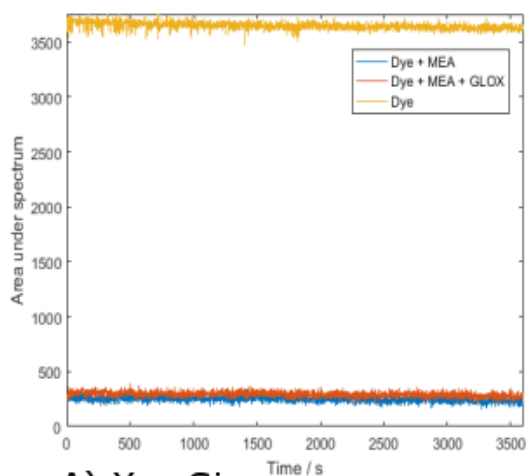




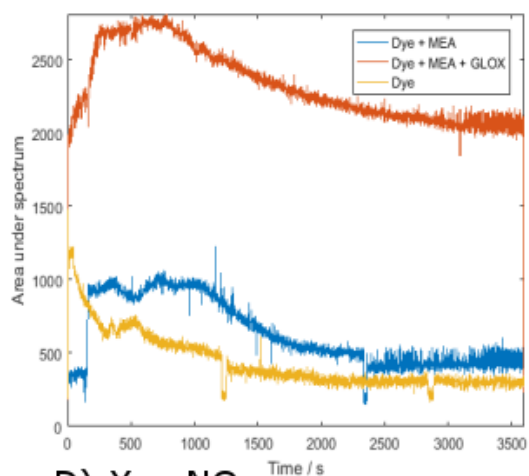
*Scheme 3.10 – Reversible formation of a stable radical in rhodamine dyes on exposure to thiols.*

Some fluorescence intensity was recovered with the addition of GLOX buffers in GeR and HR (**49** and **57**, respectively) dyes, however, even if the fluorescence intensity increased in the GLOX buffer, there was no decay over the course of 1 hour, and the dyes were still photostable (Figure 3.11B, C). This suggested that the dyes may not be suitable for SMLM imaging. It may be that the photoblinking observed when using rhodamine dyes is purely based on the ring opening/closing between the open and spirolactam forms (Scheme 3.1, page 64), as opposed to having an electronic dark state. Indeed, it may not be possible for the xanthene moiety to exhibit photoblinking under normal dSTORM conditions in the absence of a 2-carboxyl moiety on the pendant aryl ring. In order to test whether this method of solution phase analysis is suitable for SMLM dye assessment, observation of the dyes blinking under SMLM conditions must be undertaken.

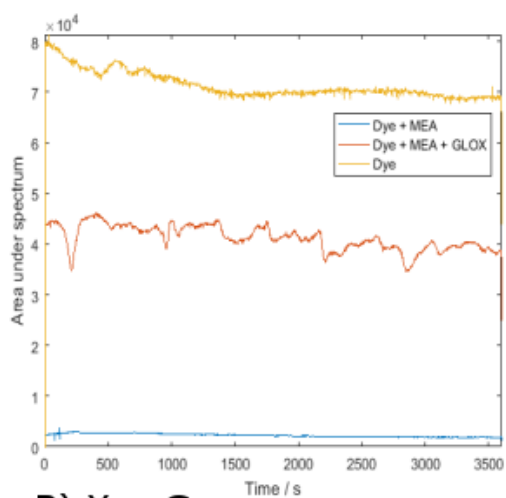
Again, the *N*-oxide rhodamine (**51**) behaved differently to the other dyes in that it was not photostable to continued laser irradiation, and was not initially quenched by MEA (Figure 3.11D). However, although fluorescence intensity did slowly decrease over time, there was no recovery of fluorescence intensity when oxygen was reincorporated into the sample by agitation. Interestingly, fluorescence intensity increased in the presence of GLOX buffer. *N*-Oxides have previously been shown to quench fluorescence,<sup>196,197</sup> so the rise in fluorescence intensity could be explained by the presence of the GLOX system, which removes oxygen from the system (thus leaving only one fluorescence quenching species in solution).



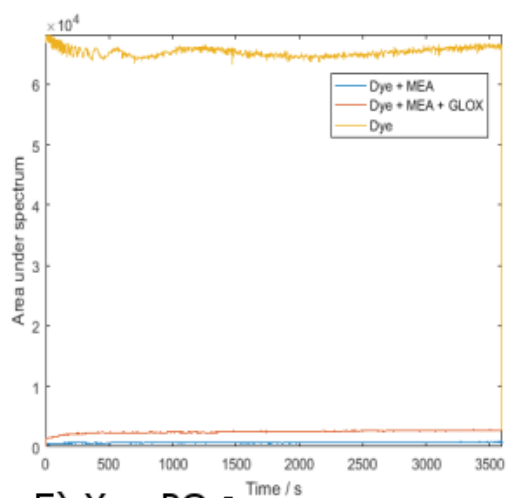
A)  $X = \text{Si}$



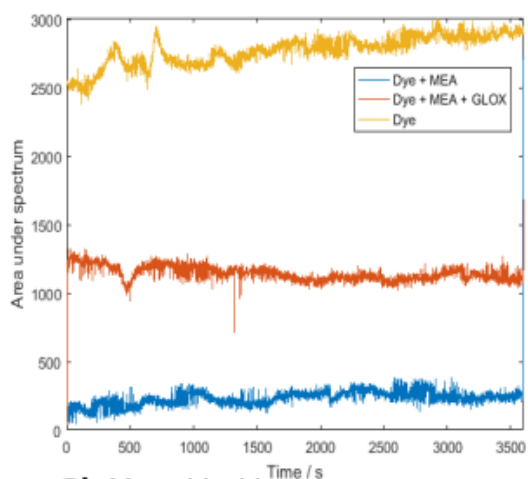
D)  $X = \text{NO}$



B)  $X = \text{Ge}$



E)  $X = \text{PO}_2^-$



C)  $X = \text{H}, \text{H}$

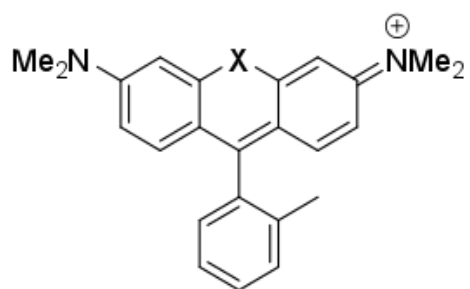


Figure 3.11 – Fluorescence intensity over time with continued laser intensity for the five rhodamine derivatives. A)  $X = \text{Si}(\text{Me})_2$  (**48**), B)  $X = \text{Ge}(\text{Me})_2$  (**49**), C)  $X = \text{H}, \text{H}$  (**57**) D)  $X = \text{NO}$  (**51**), E)  $X = \text{PO}_2^-$  (**53**).

### 3.4 PVA blinking studies

Since GLOX buffer had previously been confirmed as the superior buffer system for SMLM imaging with the benzodiazole dyes, only this system was used to test the blinking activity of the rhodamine dyes. The dyes were, once again, suspended in PVA matrices on glass slides and imaged 30-60 minutes after the addition of GLOX buffer.

Despite the photostability of SiR, GeR, P(V)R, and HR (**48**, **49**, **53**, and **57**, respectively) in solution (Figure 3.11A, B, C, E), and the inability of NOR (**51**) to recover any fluorescence intensity after bleaching (Figure 3.11D), all dyes exhibited photoblinking activity under the microscope when suspended in a PVA matrix in the presence of GLOX buffer. However, despite this positive outcome the solution phase bleaching experiments were then deemed unreliable for predicting the SMLM suitability of fluorophores due to their inability to predict the photoswitching behaviour of the five rhodamine derivatives.

Table 3.6 – Blink analysis of the various rhodamine derivatives.

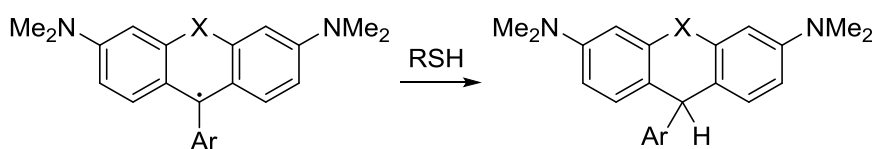
| Dye                  | Average blink density /<br>$\mu\text{m}^{-2}$ <sup>b</sup> | Average on time /<br>s <sup>c</sup> | Average number of<br>cycles <sup>c</sup> |
|----------------------|--|-------------------------------------|--|
| SiR ( <b>49</b> )    | 2.59   | 0.29                                | 1.9                                      |
| GeR ( <b>48</b> )    | 60.57  | 0.23                                | 1.9                                      |
| NOR ( <b>51</b> )    | 4.28   | 0.21                                | 1.6                                      |
| P(V)R ( <b>53</b> )  | 3.75   | 0.13                                | 1.4                                      |
| HR ( <b>57</b> )     | 6.85   | 0.21                                | 3.3                                      |
| Control <sup>d</sup> | 0.03   | 0.06                                | 1.0                                      |

<sup>a</sup> All dye solutions were diluted to  $1 \times 10^{-8}$  M in 1 wt% PVA (48,000 MW) in distilled water. Andor Solis was used with Fiji<sup>51,52</sup> and the ThunderSTORM plugin<sup>50</sup> to record and analyse blink data. <sup>b</sup> Calculated as the number of blinking events captured within a specified area over the duration of the experiment. <sup>c</sup> Calculated by plotting z-axis profiles of pixel intensity for individual molecules. <sup>d</sup> 1% PVA solution dropped onto microscope slide with no dye.

In most cases, the five dyes performed very similarly to each other. GeR (**49**) had a very large blink density of 60.57 which was an order of magnitude larger than the other dyes.

This may, however, be as a result of having the best absorption spectrum overlap with the 647 nm laser, resulting in more fluorophores being activated at any one time. Nevertheless, this result should not be discounted since 647 nm is one of the most commonly used lasers in super-resolution imaging labs due to the popularity of the dye AlexaFluor 647.<sup>195</sup> As such, it is favourable to be able to synthesise dyes that have good spectral overlaps with commonly used lasers.

The phosphorus containing dye (P[V]R, **53**), on average, fluoresced for approximately half the time that the other rhodamine analogues did. This suggests that the dark state is more easily accessible for this dye as it is able to transition to the dark state more quickly. Conversely, it may be more difficult for the phosphorus dye to exit the dark state, as reflected by the slightly lower number of blinking cycles. In this case it could be inferred that the dark state is more stable. The nature of the dark state may either be the radical, or this could react with the thiol in solution to give a protonated species (FIG).



*Scheme 3.11 – Proposed protonation of a radical rhodamine species to give a protonated analogue.*

Molecules of HR (**57**) tended to blink many more times than the other dyes. If the dark state in these molecules is due to a stable radical (Scheme 3.10) it may be that the orientation of the three aryl rings (Figure 3.8) cannot provide sufficient orbital overlap to stabilise the benzyl radical. If this radical is indeed less stable the dye would decay back to the ground state more quickly, giving the dye more opportunity to blink on multiple occasions. In all cases the dyes blinked relatively slowly, and at similar rates to NPT- and

NPSe-APTES (**7** and **8**, respectively) over the course of the experiment and were deemed to blink at a suitable rate for SMLM imaging.

Again,  $z$ -axis profiles that were converted to on/off trajectories were used to extract data about the dyes. Since the camera that had been used to study the rhodamine dyes had been replaced (with the Andor iXon Ultra 888), new parameters had to be used to calculate data. The threshold for deciding whether a dye was emitting at a sufficient level was raised to 500 counts.

In this case the analog-to-digital conversion ratio was not so simple. The calculation in this case was a four-step process, as defined by the manufacturer in their user manual (Figure 3.12) based on intrinsic properties of the dyes (quantum yield, QY) and the camera (bias offset and pre-amplification factor), as well as the EM gain (set by the user before taking data).

Based on an average noise signal of 200 counts and a dark current of 0.00025 amps (specified in the manufacturer's user manual), the value used to account for the bias offset and pre-amplification factor (pre-amp) was -199.9875, and while imaging the EM gain was set at 50. The number of electrons detected was converted to a number of photons by multiplying by the quantum yield measured at the wavelength of maximum emission.

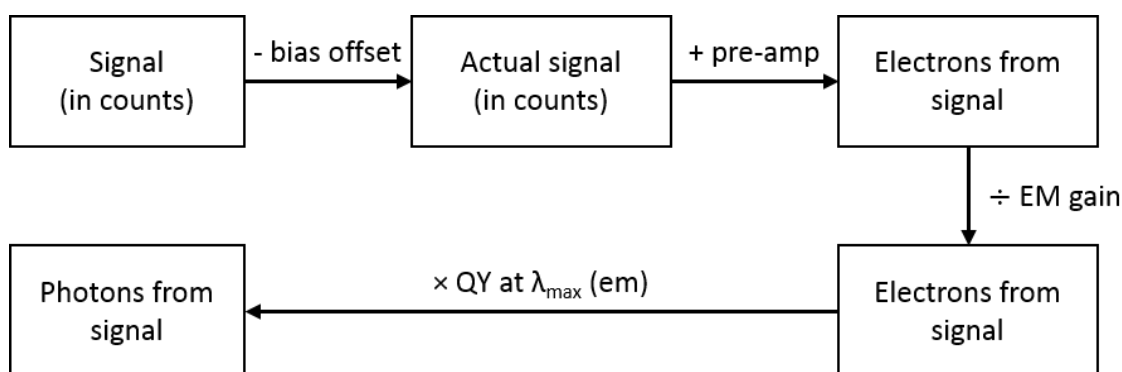


Figure 3.12 – The process used to calculate the number of photons detected per blinking event.

Though the average numbers of photons detected per blinking event do look very different between dyes, the values do reflect the magnitude of the quantum yield for each dye (Table 3.7). Although the number of photons detected for the germanium containing dye (GeR, **49**) is low at only 66.0 photons, the fact that the blinking events could be reliably detected by the camera means that the dye is appropriate for use in SMLM imaging. The rest of the dyes emitted detectable photons at similar magnitudes to dyes in the literature with similar structures.<sup>142</sup>

The on/off duty cycles of the five rhodamine derivatives were of an appropriate magnitude for the dyes to be practically useful for SMLM imaging, and comparable to the top-performing dyes currently used, as analysed by Dempsey, and coworkers.<sup>142</sup>

*Table 3.7 – Further blink analysis of the rhodamine derivatives, as compared to their measured quantum yields.*

| Dye                 | $\Phi$ / % | Avg. photons detected per blink <sup>c</sup> | Avg. on/off duty cycle |
|---------------------|------------|--|------------------------|
| SiR ( <b>49</b> )   | 7.9        | 832.1  | 0.0037                 |
| GeR ( <b>48</b> )   | 0.7        | 66.0   | 0.0029                 |
| NOR ( <b>51</b> )   | 93.3       | 11886.3                                      | 0.0024                 |
| P(V)R ( <b>53</b> ) | 14.0       | 1148.0                                       | 0.0012                 |
| HR ( <b>57</b> )    | 5.3        | 127.7  | 0.0048                 |

<sup>a</sup> All dye solutions were diluted to  $3 \times 10^{-8}$  M in a 1 wt% PVA (48,000 MW) in distilled water. FITC filter cube was used. Andor Solis was used with Fiji,<sup>51,52</sup> and the ThunderSTORM plugin to record and analyse blinking data.<sup>50</sup> <sup>b</sup> A: Dye solution with MEA (0.1 M); B: Dye solution with MEA (0.1 M) and GLOX buffer. <sup>c</sup> Calculated based on the analog-to-digital ratio for the camera used (Andor Zyla sCMOS) being 0.28 as stated in the manufacturers specifications.

It was suggested that because SiR and HR (**48** and **57**, respectively) had lower excited state lifetimes, their blinking behaviour may be different. The duty cycles of these two molecules were notably higher than the other three rhodamine analogues (i.e. these molecules spent more time in their ‘on’ state than the other molecules). In HR (**57**) this may be as a result of a higher number of blinking cycles, which in turn may be attributed

to a less stable excited state, as evidenced by the molecule having a low excited state lifetime. In SiR (**48**) this can be attributed to molecules being ‘on’ for longer periods of time, despite having a similar number of blinking cycles compared to the other dyes.

### 3.5 Conclusions

In summary, it was possible to synthesise a range of rhodamine-like dyes with heteroaromatic substitution at the 10-position of the xanthene structure. The introduction of larger atoms led to the distortion of the central ring, resulting in a change in intrinsic photophysical properties such as emission maxima and quantum yield. An *N*-oxide acridine-type dye (NOR, **51**) was synthesised and was found to have drastically different photophysical properties to the other structural analogues.

Despite these differences in photophysical behaviour, the dyes performed remarkably similarly under SMLM conditions, with few exceptions. The majority of dyes also performed similarly in bleaching experiments, in that little to no bleaching was observed. Conversely, the *N*-oxide acridine dye (**51**) did exhibit photobleaching during the solution-phase bleaching experiments but it was not possible to restore fluorescence intensity with the reincorporation of oxygen into solution. None of these results reflected the observed photoblinking behaviour of the dyes when suspended in the PVA matrices, and as such the bleaching experiments were deemed unreliable for the prediction of whether or not a dye would be useful for SMLM imaging.

As for the suitability of the dyes for super-resolution techniques, each dye performed well and had parameters (e.g. number of cycles, photons detected, duty cycle) in line with dyes that are currently used to capture super-resolution images. As well as this, the synthesis of each dye was identical with the exception of the use of a different electrophile in each case, meaning that no dye is more difficult to obtain than any other. As such, all five dyes

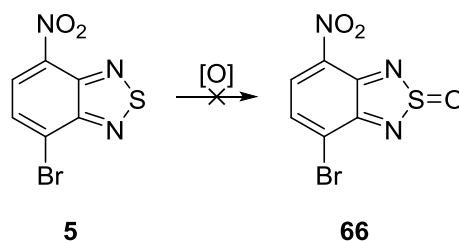
could be considered viable choices, however, it is important to consider the wavelength of lasers available. In this case the germanium containing dye (GeR, **49**) outperformed the other analogues in terms of blink density due to good spectral overlap with the laser used, despite all dyes being present at the same concentration. These results demonstrate the need for another large scale screening of dyes capable of exhibiting photoblinking behaviour to measure key properties (such as blink rate, blinking density, etc.). Although this has previously been done by Dempsey, and coworkers, this study was published in 2011, and many new dyes have been developed, such as those detailed in this work.



## 4 Conclusions and future work

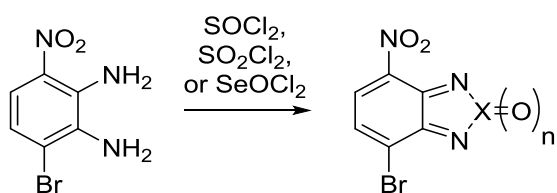
The aims of this work were to synthesise and analyse a range of chemically similar dyes by initial assessment in the solution phase, then to image the dyes in a PVA matrix and/or supported on a silica nanoparticle. This was to be achieved using two sets of dyes with atomic substitution either down a group of the periodic table or with elements from around the p-block. In the case of the 4-nitrobenzochalcogenazole dyes, both PVA matrices and silica nanoparticles were used successfully to assess whether dyes could be used for SMLM imaging. It was found that, due to a combination of having the most desirable qualities and being synthetically accessible, the benzothiazole was most amenable for super-resolution imaging using STORM.

In the future it may be interesting to explore other analogues of the benzodiazole dyes with atoms from other groups of the periodic table (e.g. a benzotriazole). Although this was considered as an option, no compounds of this type were prepared due to time constraints. It may also be interesting to examine the NPT- and NPSe-APTES (**7** and **8**, respectively) analogues with different oxidation states at sulfur and selenium, respectively. In this study, only S(II) and Se(II) derivatives were synthesised, but it is well known that both elements can exist in oxidation states IV and VI.<sup>198</sup>



*Scheme 4.1 – Attempted oxidation of NPT-Br (**5**) to a sulfoxide analogue (**66**).*

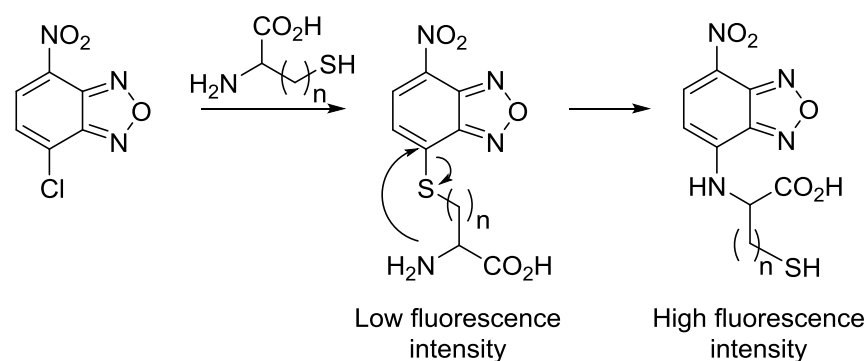
Some attempts were made to oxidise NPT-Br (**5**) to its sulfoxide analogue (**66**, Scheme 4.1). This may be, as previously stated, because the sulfur atom could exist in its S(IV) oxidation state within the heteroaromatic ring. Various oxidising agents were used, including oxone, and aqueous hydrogen peroxide, however in both of these cases only starting material was returned. Other stronger oxidants (e.g. Jones oxidation, permanganates, or O<sub>2</sub> gas), or reaction of dianilines with reagents such as SOCl<sub>2</sub>, SO<sub>2</sub>Cl<sub>2</sub>, or SeOCl<sub>2</sub> (Scheme 4.2) could be trialled.



*Scheme 4.2 – Proposed alternate synthesis to access benzothia- and benzoselenadiazoles at higher oxidation states. X = S or Se, n = 1 or 2.*

A recent journal article detailed the synthesis of an NBD analogue in which the side chain is either a cysteine or homocysteine residue aimed to find a mechanism for distinguishing between the two (Scheme 4.3).<sup>199</sup> The free amine is able to spontaneously displace the sulfur atom *via* a 5- or 6-membered transition state, and this process was much quicker in cysteine. The aryl thioether had a low fluorescence intensity and the aryl amine had a high fluorescence intensity, and this system was used as a 'turn-on' fluorescent probe.

It may be interesting to examine these types of structures as 'turn-on' fluorescent dyes, in which the rearrangement occurs in response to an external stimulus (e.g. illumination of a certain wavelength of light, or response to changes in pH), specifically with respect to dyes capable of photoblinking.



*Scheme 4.3 – The proposed spontaneous rearrangement of cysteine or homocysteine to go from a low fluorescence intensity aryl thioether to a high fluorescence intensity aryl amine.  $n = 1$  or  $2$ .*

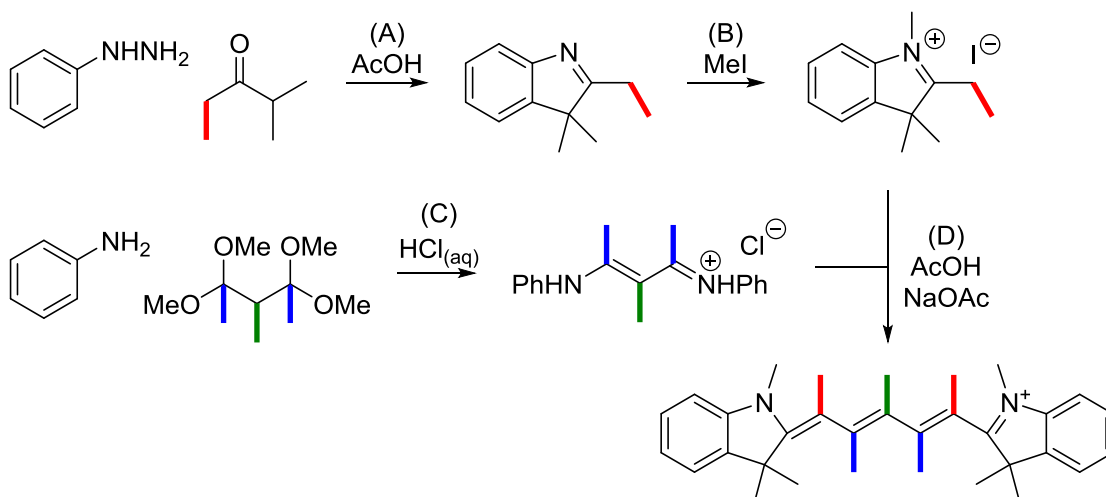
It was also possible to assess a range of rhodamine derivatives for their suitability to be SMLM dyes by suspending them in PVA matrices. It was found that all of the dyes that were synthesised in this study had properties desirable for capturing super-resolution images using STORM, but since the dyes absorbed and emitted across a large portion of the visible spectrum, care should be taken when selecting a dye to choose a dye that will have good overlap with the available laser wavelengths.

It would have been interesting to analyse a larger range of rhodamine derivatives, but due to synthetic challenges and time constraints, it was not possible to access the other target compounds. It was particularly interesting to note that HR (**57**) also showed that it was capable of photoblinking despite the absence of an atom at position 10 of the xanthene structure, which resulted in a large torsional angle between the aryl rings. It would be prudent to further explore the concept of torsion in a range of molecules capable of photoblinking to see how the photophysical properties are affected.

One might suggest starting with the more commonly used dyes. An example would be to monitor the effects of introducing torsion to the polymethine chain in cyanine 5 (Cy5) dyes. Since Cy5 is the backbone for one of the most popular dyes used for STORM and related techniques (AlexaFluor 647, or AF647), analyses to see how the photophysical

properties (in particular the photoblinking behaviour) are altered with increasing torsion in the molecule could be undertaken. This may, in turn, prove useful in the rational design of new photoblinking fluorophores in the future.

The published synthesis of Cy5 is, in theory, easy to modify to include methyl groups along the pentamethine chain (Scheme 4.4).<sup>200</sup> The proposed route has been colour coded to make the origin of each pendant methyl group more evident. It is not only possible to use this route to synthesise symmetrical cyanine dyes, but in step (D) two different indole compounds can be added sequentially to give an asymmetric cyanine dye rather than adding two equivalents of the same indole at once.<sup>200</sup>



Scheme 4.4 – Synthetic route that can be taken to synthesise a range of methylated cyanine dyes.

With specific reference to the aim of this body of work (to assess the qualities that make small organic fluorophores STORM compatible to influence the future synthesis of rationally designed fluorophores), it seems that it is not possible to create a list of ideal properties that all dye families will fit into in order for them to be SMLM active, and each family of dye must be assessed in its own right. In the case of the benzodiazoles the

addition of heavier atoms slowed the blink rate, making the heavier dye molecules more suited for the technique.

In the case of the rhodamine analogues, all of the structurally similar dyes performed similarly, regardless of their degree of aromaticity. This is likely to be due to a different blinking mechanism, and the relative stabilities of a *tris*-benzyl radical dark state. As such, further work is required in which other families of dyes with different blinking mechanisms are studied before a definitive list of desirable qualities can be compiled.

## 5 Experimental

All starting materials were purchased from Sigma–Aldrich, Alfa Aesar or Fluorochem and used as purchased. Air sensitive reactions were conducted in flame-dried glassware under an atmosphere of nitrogen or argon.  $^1\text{H}$  and  $^{13}\text{C}$  NMR spectra were recorded in  $\text{CDCl}_3$ , MeOD, or  $\text{D}_6$ -DMSO as specified on Bruker 400 MHz spectrometers. Chemical shifts are recorded on the  $\delta$  scale relative to the residual solvent peak and coupling constant ( $J$ ) values are reported in Hz.

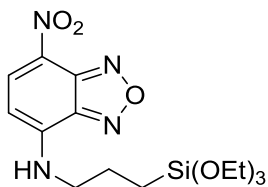
Liquid chromatographic mass spectrometry (LCMS) was performed using electron ionisation (EI), electrospray ionisation (ES or ESI), affinity purification (AP) or direct infusion using either a Walter ITC Premier XE instrument or a Micromass LCT instrument. Infrared spectra were obtained using a PerkinElmer RX1 FT-IR spectrometer with a Sinsir Technologies DuraSimlir II ATR attachment. UV/Vis absorption spectra were measured using a Cary Bio 3 spectrophotometer. Excitation and emission spectra were recorded a Fluoromax Fluorometer. Dynamic light scattering data was collected using a Malvern Zetasizer NanoZS instrument. Confocal microscopy images were taken using a wide-field Delta Vision confocal microscope. Scanning electron microscopy images were taken using a Philips XL-20 SEM. Melting points were measured using a Gallenkamp melting point apparatus. Dye photobleaching data was recorded using Ocean Optics STS-VIS Miniature Spectrometer. Blink rate analysis was undertaken using a Nikon Eclipse Ti microscope coupled to a Andor Zyla sCMOS camera, or an Andor iXon Ultra.

Geometry optimisations were calculated using Gaussian 09 using density functional theory (DFT) with a B3LYP 6311 g (d,p) basis set. All frequencies were confirmed to be

real. Energy levels were calculated using a time-dependent self-contained field (TD-SCF) DFT with a B3LYP 6311 g (d,p) basis set and were solved for N=100 states.

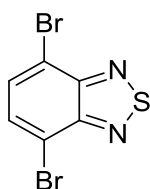
Data for time-resolved photoluminescence lifetimes was obtained using the time-correlated single photon counting (TCSPC) method. The samples were excited with a pulsed laser of 510 nm, repetition rate 2.5 MHz, average power <4 mW, pulse width <60 ns. The PL was detected with a single-photon avalanche diode, which has an instrument response function that was measured to be around 1 ns.

### 7-Nitro-*N*-[3-(triethoxysilyl)propyl]-2,1,3-benzoxadiazol-4-amine (3)



A sample of 4-chloro-7-nitrobenzo-2,1,3-oxadiazole (0.10 g, 0.5 mmol) was stirred in ethanol (10 mL). Once dissolved, the solution was cooled to 0 °C and (3-aminopropyl)triethoxysilane (0.14 mL, 0.6 mmol, 1.2 eq.) was added. The reaction mixture was stirred in the dark for 2 h at 0 °C then for 24 h at room temperature during which time the mixture turned from yellow to dark green. The solvent was removed *in vacuo* to leave a dark green residue which was purified by flash column chromatography on silica gel, eluting with petroleum ether/ethyl acetate 2:1 to yield the product as an orange/red solid (0.10 g, 48%); m.p. 110–114 °C;  $R_f = 0.73$  (petroleum ether: ethyl acetate 2:1);  $^1\text{H NMR}$  (400 MHz,  $\text{CDCl}_3$ ): 8.48 (1H, d,  $J$  8.7, ArCH), 6.95 (1H, s, NH), 6.17 (1H, d,  $J$  8.7, ArCH), 3.86 (6H, q,  $J$  7.0,  $3 \times \text{OCH}_2\text{CH}_3$ ), 3.61–3.50 (2H, m,  $\text{NHCH}_2$ ), 2.04–1.93 (2H, m,  $\text{CH}_2$ ), 1.24 (9H, t,  $J$  7.0,  $3 \times \text{OCH}_2\text{CH}_3$ ), 0.77 (2H, t,  $J$  7.6,  $\text{SiCH}_2$ );  $m/z$  ( $\text{ES}^+$ ) 439 (8%), 407.1379 (100,  $\text{M}+\text{Na}^+$ ,  $\text{C}_{15}\text{H}_{24}\text{N}_4\text{O}_6\text{NaSi}$  requires 407.1363), 393 (8), 339 (22,  $\text{M}^+-\text{OEt}$ ), 235 (5), 210 (5). Data in accordance with the literature.<sup>91</sup>

### 4,7-Dibromo-2,1,3-benzothiadiazole (6)

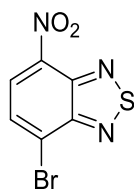


Benzo-2,1,3-thiadiazole (2.86 g, 21 mmol, 1 eq.) was heated at reflux in aqueous hydrobromic acid (48% w/w, 8 mL). Bromine (3 mL, 58 mmol, 2.75 eq.) was added over



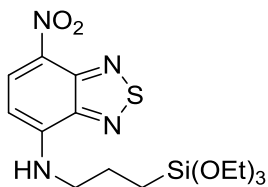
thirty minutes. On complete addition the mixture was heated for a further 3 h before allowing to return to room temperature and adding potassium bicarbonate (sat. aq., 20 mL). The resulting precipitate was filtered and washed with cold water (3 × 20 mL) and diethyl ether (3 × 20 mL) before drying under vacuum to give the product as a yellow powder (6.02 g, 98%) which was used without further purification; m.p. 186 °C (lit.<sup>201</sup> 187 – 188 °C); <sup>1</sup>H NMR (400 MHz, D<sub>6</sub>-DMSO): 7.97 (2H, s, ArCH). Data in accordance with the literature.<sup>201</sup>

#### 4-Bromo-7-nitro-2,1,3-benzothiadiazole (5)



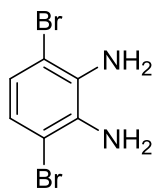
4,7-Dibromobenzo-2,1,3-thiadiazole (0.10 g, 0.34 mmol) was dissolved in nitric acid (68%, 5 mL). The mixture was stirred at reflux for 2 h during which time the solution changed colour from orange to pale yellow. The hot solution was poured onto ice-water (10 mL) and produced a pale yellow precipitate. Filtration and drying afforded the product as a pale yellow crystalline solid which was used without further purification (0.03 g, 40%); m.p. 218–220 °C (lit.<sup>202</sup> 218–220 °C); <sup>1</sup>H NMR (400 MHz, CDCl<sub>3</sub>): 8.47 (1H, d, *J* 8.0, ArCH), 8.03 (1H, d, *J* 8.0, ArCH); <sup>13</sup>C NMR (100 MHz, D<sub>6</sub>-DMSO): 154.4 (ArC), 145.8 (ArC), 139.1 (ArC), 131.4 (ArCH), 128.8 (ArCH), 122.3 (ArC); *m/z* (EI<sup>+</sup>) 261 (48%, C<sub>6</sub>H<sub>2</sub>N<sub>3</sub>O<sub>2</sub>S<sup>81</sup>Br), 259 (47), 231 (81), 229 (80), 203 (46), 201 (43), 134 (100), 83 (88). Data in accordance with the literature.<sup>106</sup>

## 7-Nitro-*N*-[3-(triethoxysilyl)propyl]-2,1,3-benzothiadiazole-4-amine (7)



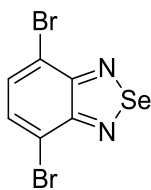
A sample of bromide **5** (0.030 g, 0.12 mmol) was stirred in ethanol (10 mL) with (3-aminopropyl)triethoxysilane (0.034 g, 0.15 mmol, 1.25 eq.) at 0 °C in the dark. Solid potassium carbonate (0.017 g, 0.012 mmol, 0.1 eq.) was added to the stirred solution which was kept at 0 °C for 2 h, then at room temperature for a further 22 h, during which time the reaction mixture turned from yellow to green. The solvent was removed under reduced pressure and the residue re-dissolved in ethyl acetate (25 mL). This solution was washed with water (2 × 25 mL) and brine (2 × 25 mL), dried over MgSO<sub>4</sub>, filtered and concentrated *in vacuo*, followed by purification using flash column chromatography on silica gel eluting with ethyl acetate and petroleum ether (1:3) to give the title compound as a dark orange solid; (0.022 g, 45%); m.p. 100–102 °C; *R*<sub>f</sub> = 0.51 (petroleum ether: ethyl acetate 3:1);  $\nu_{\max}$  (ATR)/cm<sup>-1</sup> 3339 (br, NH), 2972 (w, CH), 2885 (w, CH), 1563 (s, NO<sub>2</sub>), 1493 (s); <sup>1</sup>H NMR (400 MHz, CDCl<sub>3</sub>): 8.67 (1H, d, *J* 8.8, ArCH), 6.67–6.63 (1H, m, NH), 6.41 (1H, d, *J* 8.8, ArCH), 3.86 (6H, q, *J* 7.0, 3 × OCH<sub>2</sub>CH<sub>3</sub>), 3.53 (2H, app. q, *J* 7.1, NHCH<sub>2</sub>), 1.95 (2H, app. pent, *J* 7.1, CH<sub>2</sub>), 1.24 (9H, t, *J* 7.1, 3 × OCH<sub>2</sub>CH<sub>3</sub>), 0.81–0.77 (2H, m, SiCH<sub>2</sub>); <sup>13</sup>C NMR (100 MHz, CDCl<sub>3</sub>): 148.3 (ArC), 146.7 (ArC), 146.5 (ArC), 134.0 (ArCH), 128.3 (ArC), 98.9 (ArCH), 58.6 (3 × OCH<sub>2</sub>), 45.6 (CH<sub>2</sub>), 22.2 (CH<sub>2</sub>), 18.3 (3 × CH<sub>3</sub>), 7.8 (CH<sub>2</sub>); *m/z* (ESI<sup>+</sup>) 446 (6), 401.1313 (100%, MH<sup>+</sup> C<sub>15</sub>H<sub>25</sub>N<sub>4</sub>O<sub>5</sub>SSi requires 401.1309), 355 (16).

### 3,6-Dibromo-1,2-benzenediamine (10)



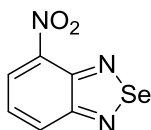
Under an atmosphere of nitrogen, NaBH<sub>4</sub> (0.64 g, 17.1 mmol, 10 eq.) was added portionwise to a suspension of 4,7-dibromobenzo-2,1,3-benzothiadiazole (0.50 g, 1.71 mmol) in ethanol (20 mL) at 0 °C. The mixture was warmed to room temperature and stirred for 20 h during which time the solution went from yellow to dark orange. The solvent was removed *in vacuo* and the orange residue was redissolved in water (10 mL). The product was extracted with diethyl ether (3 × 10 mL). The organic phases were combined, washed with brine (10 mL), dried over magnesium sulfate, filtered and evaporated to dryness. The pale yellow solid was used without further purification. (0.36 g, 78%); m.p. 94 °C (lit.<sup>107</sup> 94 – 95 °C); <sup>1</sup>H NMR (400 MHz, CDCl<sub>3</sub>): 6.84 (2H, s, ArCH), 3.89 (4H, br. s, 2 × NH<sub>2</sub>); <sup>13</sup>C NMR (100 MHz, CDCl<sub>3</sub>): 133.7 (2 × ArC), 123.3 (2 × ArCH), 109.7 (2 × ArC). Data in accordance with the literature.<sup>107</sup>

#### 4,7-Dibromo-2,1,3-benzoselenadiazole (11)



3,6-Dibromobenzene-1,2-diamine (0.34 g, 1.29 mmol) was suspended in ethanol (10 mL) and heated to reflux. A hot, aqueous solution (10 mL) of selenium(IV) oxide (0.71 g, 6.50 mmol, 5 eq.) was added. When addition was complete, a bright yellow precipitate formed. The mixture was heated at reflux for a further 2 h before cooling to room temperature and collecting the product as a bright yellow solid (0.37 g, 83%) which was used without further purification. m.p. 285-287 °C (lit.<sup>108</sup> 285-287 °C); <sup>1</sup>H NMR (400 MHz, CDCl<sub>3</sub>): 7.64 (1H, s, 2 × ArCH). Data in accordance with the literature.<sup>108</sup>

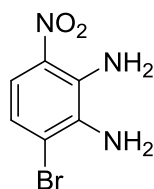
#### 4-Nitro-2,1,3-benzoselenadiazole (13)



6-Nitro-1,2-benzenediamine (0.015 g, 0.10 mmol, 1 eq.) was suspended in ethanol (25 mL) and heated at reflux. A solution of selenium(IV) dioxide (0.012 g, 0.11 mmol, 1.1 eq.) in hot water (25 mL) was added slowly. The resulting solution was stirred at reflux for a further 5 h before returning to room temperature and removing the ethanol *in vacuo*. The aqueous solution was extracted with dichloromethane (3 × 25 mL). The organic phases were combined, washed with brine (25 mL), dried over magnesium sulfate, filtered and evaporated to dryness. The residue was purified using flash column chromatography on silica gel, eluting with ethyl acetate and petroleum ether (1:1) to give the named product as a peach coloured powder with a mild eggy odour. (0.021 g, 92%);

R<sub>f</sub> 0.69 (ethyl acetate: petroleum ether, 1:1); m.p. 214 °C (lit.<sup>203</sup> 214 – 216 °C); <sup>1</sup>H NMR (400 MHz, CDCl<sub>3</sub>): 8.47 (1H, dd, *J* 7.2, 0.9, ArCH), 8.25 (1H, dd, *J* 8.9, 0.9, ArCH), 7.69 (1H, dd, *J* 8.9, 7.2, ArCH); *m/z* (ES<sup>+</sup>) 271 (13%, C<sub>6</sub>H<sub>3</sub>N<sub>3</sub>O<sub>2</sub><sup>80</sup>Se + Na<sup>+</sup> + H<sub>2</sub>O), 231 (20, C<sub>6</sub>H<sub>3</sub>N<sub>3</sub>O<sub>2</sub><sup>82</sup>Se), 229 (100, C<sub>6</sub>H<sub>3</sub>N<sub>3</sub>O<sub>2</sub><sup>80</sup>Se), 227 (36, C<sub>6</sub>H<sub>3</sub>N<sub>3</sub>O<sub>2</sub><sup>78</sup>Se), 225 (12, C<sub>6</sub>H<sub>3</sub>N<sub>3</sub>O<sub>2</sub><sup>76</sup>Se). Data in accordance with the literature.<sup>203</sup>

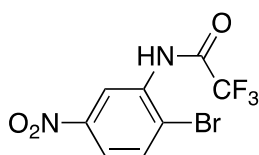
### 3-Bromo-6-nitro-1,2-benzenediamine (16)



1-Amino-2-bromo-5-nitrobenzene (0.25 g, 1.15 mmol) was dissolved in dry dimethyl sulfoxide (15 mL) at room temperature under an atmosphere of argon. 1,1,1-Trimethylhydrazinium iodide (0.23 g, 1.15 mol, 1 eq.) was added in one portion before adding fresh sodium pentoxide (0.38 g, 3.45 mmol, 3 eq.). The solution turned from orange to dark blue on immediate addition of the base. The reaction was stirred overnight at room temperature before pouring onto ice water (50 mL). The product was extracted with dichloromethane (2 × 25 mL) and the organic layers washed with aqueous hydrochloric acid (1 M, 2 × 25 mL) and brine (25 mL) before drying over magnesium sulfate, filtering and removing solvent *in vacuo* to give the product as a dark orange solid which was used without further purification (0.078 g, 30%); m.p. 145–148 °C;  $\nu_{\max}$  (ATR)/cm<sup>-1</sup> 3465 (w, NH), 3422 (w, NH), 3358 (m, NH), 1620 (s, NH), 1556 (m), 1505 (s, NO<sub>2</sub>); <sup>1</sup>H NMR (400 MHz, CDCl<sub>3</sub>): 7.62 (1H, d, *J* 9.3, ArCH), 6.91 (1H, d, *J* 9.3, ArCH), 6.16 (2H, br. s, NH<sub>2</sub>), 3.95 (2H, br. s, NH<sub>2</sub>); <sup>13</sup>C NMR (100 MHz, [D<sub>6</sub>]DMSO): 135.9 (ArC), 135.2 (ArC), 130.4 (ArC), 119.3 (ArCH), 113.9 (ArCH), 111.9 (ArC); *m/z*

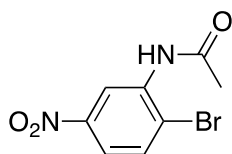
(ESI<sup>+</sup>) 233.9698 (95%, MH<sup>+</sup>, C<sub>6</sub>H<sub>7</sub>N<sub>3</sub>O<sub>2</sub><sup>81</sup>Br requires 233.9696), 232 (100, C<sub>6</sub>H<sub>7</sub>N<sub>3</sub>O<sub>2</sub><sup>79</sup>Br). <sup>1</sup>H NMR data was not in accordance with that reported in the literature.<sup>116</sup> Full analysis was undertaken.

***N*-(2-Bromo-5-nitrophenyl)-2,2,2-trifluoroacetamide (18)**



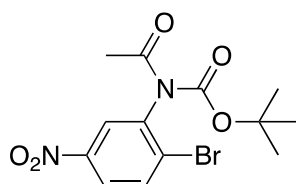
1-Amino-2-bromo-5-nitrobenzene (0.40 g, 1.84 mmol) was dissolved in a mixture of dry dichloromethane and anhydrous pyridine (1:3, 20 mL) under an atmosphere of nitrogen. Trifluoroacetic anhydride (0.29 mL, 2.02 mmol, 1.1 eq.) was added dropwise and the progress of the reaction was monitored by TLC which showed complete conversion after 2 h when the colour of the solution had completely faded. The reaction mixture was poured onto aqueous hydrochloric acid (1 M, 30 mL) and separated. The organic layer was washed with a further portion of aqueous hydrochloric acid (1 M, 30 mL) and brine (30 mL) before drying over magnesium sulfate, filtering and removing solvent under reduced pressure to give the pure product as a white solid. (0.45 g, 78%); m.p. 128–131 °C; R<sub>f</sub> = 0.56 (ethyl acetate: petroleum ether 1:3); <sup>1</sup>H NMR (400 MHz, CDCl<sub>3</sub>): 9.26 (1H, d, *J* 2.6, ArCH), 8.57 (1H, br. s, NH), 8.03 (1H, dd, *J* 8.8, 2.6, ArCH), 7.85 (1H, d, *J* 8.8, ArCH); *m/z* (ES<sup>-</sup>) 313 (100%, C<sub>8</sub>H<sub>4</sub>N<sub>2</sub>OF<sub>3</sub><sup>81</sup>Br), 311 (88, C<sub>8</sub>H<sub>4</sub>N<sub>2</sub>OF<sub>3</sub><sup>79</sup>Br). Melting point not reported in the literature but all other data was in accordance.<sup>204</sup>

### ***N*-(2-Bromo-5-nitrophenyl)acetamide (17)**



1-Amino-2-bromo-5-nitrobenzene (0.50 g, 2.3 mmol, 1 eq.) and triethylamine (0.32 mL, 2.3 mmol, 1 eq.) were dissolved in dry dichloromethane (20 mL) at 0 °C under an atmosphere of nitrogen. Acetyl chloride (0.25 mL, 3.5 mmol, 1.5 eq.) was added dropwise. On complete addition, the reaction was allowed to return to room temperature and was left to react overnight. The reaction mixture was washed with hydrochloric acid (1 M, 2 × 20 mL), saturated aqueous sodium hydrogen carbonate (2 × 20 mL) and water (20 mL) before drying the organic layer over magnesium sulfate, filtering and removing the solvent *in vacuo* to yield the product as a flaky white solid that was used without further purification. (0.57 g, 95%); m.p. 125–127 °C (lit.<sup>205</sup> 127 °C);  $R_f$  = 0.16 (petroleum ether: ethyl acetate 4:1); <sup>1</sup>H NMR (400 MHz, CDCl<sub>3</sub>): 9.31 (1H, d, *J* 2.5, ArCH), 7.87 (1H, dd, *J* 8.8, 2.5, ArCH), 7.74 (1H, d, *J* 8.8, ArCH), 7.74 (1H, br. s, NH), 2.33 (3H, s, CH<sub>3</sub>); *m/z* (ES<sup>-</sup>) 259 (95% C<sub>8</sub>H<sub>7</sub>N<sub>2</sub>O<sub>3</sub><sup>81</sup>Br), 257 (100%, C<sub>8</sub>H<sub>7</sub>N<sub>2</sub>O<sub>3</sub><sup>79</sup>Br). Melting point not reported in the literature but all other data was in accordance.<sup>118,205</sup>

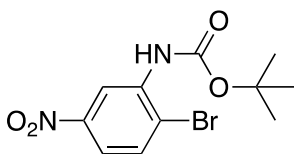
### ***tert*-Butyl acetyl(2-bromo-5nitrophenyl)carbamate (67)**



A sample of acyl protected aniline **17** (0.57 g, 2.2 mmol, 1 eq.) was dissolved in dry acetonitrile (50 mL) under an atmosphere of nitrogen. Di-*tert*-butyl dicarbonate (0.60 g,

2.75 mmol, 1.25 eq.) and *N,N*-dimethylamino pyridine (0.54 g, 0.44 mmol, 0.2 eq.) were added in one portion after which a colour change of yellow to orange was observed. The reaction was stirred at room temperature until complete by TLC. After 2.5 h the solvent was removed under reduced pressure, the residue was redissolved in ethyl acetate (50 mL), washed with hydrochloric acid (1 M, 2 × 50 mL), water (50 mL) and brine (50 mL), and dried over magnesium sulfate. After filtration, the solvent was removed *in vacuo* to afford the pure product as a pale brown solid that was used without further purification. (0.75 g, 95%); m.p. 158–162 °C;  $R_f = 0.74$  (petroleum ether: ethyl acetate 4:1);  $^1\text{H NMR}$  (400 MHz,  $\text{CDCl}_3$ ): 8.11 (1H, dd,  $J$  8.8, 2.6, ArCH), 8.07 (1H, d,  $J$  2.6, ArCH), 7.84 (1H, d,  $J$  8.8, ArCH), 2.70 (3H, s,  $\text{COCH}_3$ ), 1.41 (9H, s,  $\text{C}[\text{CH}_3]_3$ ). Melting point not reported in the literature but all other data was in accordance.<sup>118</sup>

#### ***tert*-Butyl (2-bromo-5-nitrophenyl)carbamate (19)**

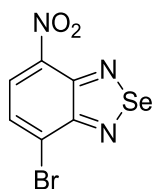


A sample of *bis*-protected aniline **67** (0.75 g, 2.1 mmol, 1 eq.) was dissolved in acetonitrile (30 mL). Hydrazine monohydrate (80% in water v/v, 0.64 mL, 10.5 mmol, 5 eq.) was added dropwise and the mixture was left to stir at room temperature for 3.5 h. The reaction was quenched with saturated aqueous ammonium chloride (30 mL) and the product was extracted with diethyl ether (3 × 30 mL). The organic phases were collected and washed with brine (30 mL) before drying over magnesium sulfate, filtering and removing the solvent under reduced pressure to give the product as a yellow solid that was used without further purification (0.60 g, 90%); m.p. 110 – 114 °C;  $R_f = 0.60$  (petroleum ether: ethyl acetate 1:2);  $^1\text{H NMR}$  (400 MHz,  $\text{CDCl}_3$ ): 9.12 (1H, d,  $J$  2.6,



ArCH), 7.78 (1H, dd, *J* 8.8, 2.6, ArCH), 7.69 (1H, d, *J* 8.8, ArCH), 7.17 (1H, br. s, NH), 1.58 (9H, s, C[CH<sub>3</sub>]<sub>3</sub>); <sup>13</sup>C NMR (100 MHz, CDCl<sub>3</sub>): 151.8 (C=O), 147.9 (ArC), 137.5 (ArC), 132.8 (ArCH), 118.4 (ArC), 117.9 (ArCH), 114.3 (ArCH), 82.4 (C[CH<sub>3</sub>]<sub>3</sub>), 28.2 (C[CH<sub>3</sub>]<sub>3</sub>); *m/z* (ES<sup>-</sup>) 317 (93%, C<sub>11</sub>H<sub>13</sub>N<sub>2</sub>O<sub>4</sub><sup>81</sup>Br), 315 (100, C<sub>11</sub>H<sub>13</sub>N<sub>2</sub>O<sub>4</sub><sup>79</sup>Br), 243 (66, C<sub>7</sub>H<sub>4</sub>N<sub>2</sub>O<sub>3</sub><sup>81</sup>Br), 241 (71, C<sub>7</sub>H<sub>4</sub>N<sub>2</sub>O<sub>3</sub><sup>79</sup>Br). Melting point not reported in the literature but all other data was in accordance.<sup>118</sup>

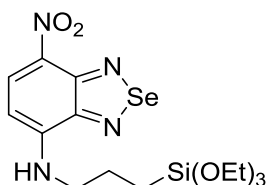
#### 4-Bromo-7-nitro-2,1,3-selenadiazole (9)



Diamine **16** (0.16 g, 0.71 mmol) was dissolved in ethanol (40 mL) and heated at reflux. A solution of selenium(IV) dioxide (0.39 g, 3.55 mmol, 5 eq.) in boiling water (20 mL) was added over 5 mins to the reaction mixture and on complete addition a yellow precipitate began to form. The mixture was maintained at reflux for a further 16 h before cooling to rt. The precipitate was isolated *via* vacuum filtration and washed with ice-cold water (2 × 10 mL) to give the title product as a mustard yellow solid which was used without further purification (0.19 g, 85%); m.p. 282–284 °C (decomp., lit.<sup>206</sup> >300 °C); Found: C, 23.4; H, 0.95; N, 13.55; Br, 26.1. C<sub>6</sub>H<sub>2</sub>N<sub>3</sub>O<sub>2</sub>SeBr requires C, 23.5; H, 0.7; N, 13.7; Br, 26.0%; *v*<sub>max</sub> (ATR)/cm<sup>-1</sup> 3461 (w), 3422 (w), 3357 (m), 3255 (w), 1618 (s), 1506 (s, NO<sub>2</sub>); <sup>1</sup>H NMR (400 MHz, [D<sub>6</sub>]DMSO): 8.39 (1H, d, *J* 8.0, ArCH), 8.12 (1H, d, *J* 8.0, ArCH); <sup>13</sup>C NMR (100 MHz, [D<sub>6</sub>]DMSO): 157.7 (ArC), 149.3 (ArC), 140.3 (ArC), 129.5 (ArCH), 127.4 (ArCH), 123.8 (ArC); *m/z* (EI<sup>+</sup>) 306.8486 (76%, M<sup>+</sup> C<sub>6</sub>H<sub>2</sub>N<sub>3</sub>O<sub>2</sub><sup>80</sup>Se<sup>79</sup>Br requires 306.8490), 277 (100), 248 (50), 182 (62), 159 (29), 131 (19), 101 (33), 80 (34).

<sup>1</sup>H NMR and IR spectra in broad agreement with the literature – no other data is reported.<sup>206</sup>

### 7-Nitro-*N*-[3-(triethoxysilyl)propyl]-2,1,3-benzoselenadiazol-4-amine (**8**)



*tris*-(Dibenzylideneacetone)dipalladium (0.0046 g, 0.005 mmol, 2 mol%) and (*S*)-(+)-PPFA (0.0062 g, 0.014 mmol, 6 mol%) were dissolved in dry THF (1 mL) in a microwave vial. Bromide **9** (0.070 g, 0.228 mmol) and APTES (0.061 g, 0.274 mmol, 1.2 eq.) were added to the solution before charging the solution with potassium *tert*-butoxide (0.033 g, 0.342 mmol, 1.5 eq.). The solution was degassed with argon for 15 mins. The tube was sealed and heated in a microwave reactor to 75 °C over 5 mins at 150 W, then held at this temperature for a further 9 mins at 100 W. On completion, the reaction mixture was diluted with ethyl acetate (10 mL) and filtered. The filtrate was evaporated to dryness purified by flash column chromatography on silica gel, eluting with petroleum ether/ethyl acetate 1:1, to give the product as a red/orange solid. (0.0015 g, 7%);  $R_f = 0.56$  (petroleum ether/ethyl acetate); m.p. 68–71 °C;  $\nu_{\max}$  (ATR)/ $\text{cm}^{-1}$  3465 (w, NH), 3361 (m, NH), 2926 (m), 1621 (s, C=N), 1511 (s, NO<sub>2</sub>); <sup>1</sup>H NMR (500 MHz, CDCl<sub>3</sub>): 8.62 (1H, d, *J* 8.8, ArCH), 6.65–6.61 (1H, m, NH), 6.17 (1H, d, *J* 8.8, ArCH), 3.78 (6H, q, *J* 7.2, 3 × CH<sub>2</sub>CH<sub>3</sub>), 3.42 (2H, app. q, *J* 7.0, NCH<sub>2</sub>), 1.85 (2H, app. quin, *J* 7.0, CH<sub>2</sub>), 1.18 (9H, t, *J* 7.2, 3 × CH<sub>2</sub>CH<sub>3</sub>), 0.71–0.68 (2H, m, SiCH<sub>2</sub>); <sup>13</sup>C NMR (125 MHz, CDCl<sub>3</sub>): 152.7 (ArC), 152.5 (ArC), 147.5 (ArC), 135.7 (ArCH), 129.9 (ArC), 97.2 (ArCH), 58.6 (3 × OCH<sub>2</sub>),

45.7 (NCH<sub>2</sub>), 22.3 (CH<sub>2</sub>), 18.3 (3 × CH<sub>3</sub>), 7.9 (SiCH<sub>2</sub>); *m/z* (ESI<sup>+</sup>) 449.0757 (100%, MH<sup>+</sup>, C<sub>15</sub>H<sub>25</sub>N<sub>4</sub>O<sub>5</sub>Si<sup>80</sup>Se requires 449.0754).

### **General procedure A for the preparation of dye coated silica nanoparticles**

Tetraethyl orthosilicate (TEOS, 1.7 mL, 7.6 mmol) was added to a stirred mixture of water (4.5 mL) and ammonium hydroxide (35%, 330 μL) in ethanol (43.5 mL). The mixture was stirred rapidly at room temperature for 24 h, after which a solution of APTES conjugated dye in ethanol (18 mM, 50 μL) was added with additional TEOS (10 μL). The particles were left to stir with the dye for 5 h at rt. Coated particles were isolated by centrifugation, re-suspended in ethanol (30 mL), isolated by centrifugation, re-suspended again in water (30 mL), and isolated by centrifugation.

### **Preparation of buffers for photophysical analysis**

Aqueous stock solutions of catalase from bovine liver (4 mg per 1 mL), glucose oxidase from *Aspergillus niger* (5 mg per 1 mL) and mercaptoethylamine (MEA, 1 M) were prepared.

*To make 10 mL MEA buffer:* take 1 mL MEA stock and make up to 10 mL with distilled water.

*To make 10 mL GLOX buffer:* take 1 mL MEA stock, 1 mL glucose oxidase stock, 0.1 mL catalase stock and make up to 10 mL with distilled water. Add solid glucose (1 g, 10% w/v).

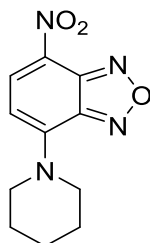
### **General procedure B for the preparation and imaging of PVA suspensions**

Fluorophores were diluted to a nanomolar concentration in 1 wt% PVA (48,000 MW) in distilled water. 50  $\mu$ L of this was added to each slide before air-drying in a fume hood overnight. Samples were imaged between 30 and 60 mins after buffer solution (MEA or GLOX, 15  $\mu$ L) was added to allow sufficient time for matrix penetration but to avoid rehydration and degradation of the polymer. Slides were sealed with a cover slip and 740 clear Rimmel London 60 second nail polish. Each sample was imaged twice in two different regions of the matrix under each buffer condition. Two samples were imaged for each dye/buffer combination. Samples were excited using a 470 nm laser with a power of 550 mW. Imaging videos were captured at a rate of 20 frames per second for 3000 frames. The ThunderSTORM plugin for Fiji was used to analyse captured data.

### **General procedure C for the cross coupling of aryl bromides and amines**

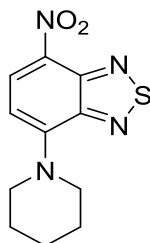
Under an atmosphere of argon, *tris*(dibenzylideneacetone)dipalladium (0.0023 g, 0.0025 mmol, 2 mol%) and (*S*)-(+)-PPFA (0.0033 g, 0.0075 mmol, 6 mol%) were dissolved in dry THF (0.5 mL) in a flame dried microwave tube. Aryl halide (0.125 mmol) and an amine (0.15 mmol, 1.2 eq.) were added to the solution before charging the vessel with potassium *tert*-butoxide (0.018 g, 0.1875 mmol, 1.5 eq.). The solution was degassed for 15 minutes then back filled with argon. In a microwave, after one minute of pre-stirring, the temperature was ramped to 75 °C over 5 minutes using 150 W then held at this temperature for a further 9 minutes at 100 W. On completion, the reaction mixture was diluted with ethyl acetate (10 mL) and gravity filtered. The filtrate was evaporated to dryness before purifying by flash column chromatography on silica gel eluting with petroleum ether and ethyl acetate.

#### 4-Nitro-7-(piperidin-1-yl)-2,1,3-benzoxadiazole (68)



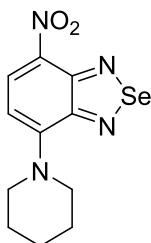
Prepared using chloride **1** (0.025 g, 0.125 mmol) and piperidine (0.013 g, 0.150 mmol) following general procedure C. Isolated as an orange solid (0.027, 87%);  $R_f$  0.61 (ethyl acetate: petroleum ether, 1:1); m.p. 164–166 °C (lit.<sup>207</sup> 166 °C);  $^1\text{H}$  NMR (400 MHz,  $\text{CDCl}_3$ ): 8.46 (1H, d,  $J$  9.2, ArCH), 6.30 (1H, d,  $J$  9.2, ArCH), 4.15 (4H, br. s,  $2 \times \text{CH}_2$ ), 1.87 (6H, br. s,  $3 \times \text{CH}_2$ ). Data in accordance with the literature.<sup>207</sup>

#### 4-Nitro-7-(piperidin-1-yl)-2,1,3-benzothiadiazole (69)



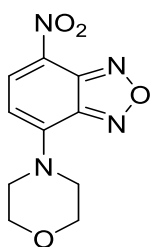
Prepared using bromide **5** (0.033 g, 0.125 mmol) and piperidine (0.013 g, 0.150 mmol) following general procedure C. Isolated as an orange solid (0.020 g, 61%);  $R_f$  0.61 (ethyl acetate: petroleum ether, 1:3); m.p. 162–164 °C;  $^1\text{H}$  NMR (400 MHz,  $\text{CDCl}_3$ ): 8.62 (1H, d,  $J$  9.3, ArCH), 6.62 (1H, d,  $J$  9.3, ArCH), 4.13–4.06 (4H, m,  $2 \times \text{CH}_2$ ), 1.89–1.81 (6H, m,  $3 \times \text{CH}_2$ ). Melting point not reported in the literature but all other data was in accordance.<sup>208</sup>

#### 4-Nitro-7-(piperidin-1-yl)-2,1,3-benzoselenadiazole (70)



Prepared using bromide **9** (0.038 g, 0.125 mmol) and piperidine (0.013 g, 0.150 mmol) following general procedure C. Isolated as a red solid (0.012 g, 30%);  $R_f$  0.70 (ethyl acetate: petroleum ether, 2:3); m.p. 196–198 °C;  $\nu_{\max}$  (ATR)/ $\text{cm}^{-1}$  3099 (w), 2937 (w), 1577 (m), 1523 (s), 1223 (s);  $^1\text{H}$  NMR (400 MHz,  $\text{CDCl}_3$ ): 8.59 (1H, d,  $J$  9.0, ArCH), 6.48 (1H, d,  $J$  9.0, ArCH), 4.04–3.98 (4H, m,  $2 \times \text{CH}_2$ ), 1.90–1.80 (6H, m,  $3 \times \text{CH}_2$ );  $^{13}\text{C}$  NMR (100 MHz,  $\text{CDCl}_3$ ): 154.0 (ArC), 153.8 (ArC), 150.4 (ArC), 133.5 (ArCH), 130.9 (ArC), 104.6 (ArCH), 51.6 ( $2 \times \text{NCH}_2$ ), 26.1 ( $2 \times \text{CH}_2$ ), 24.4 ( $\text{CH}_2$ );  $m/z$  (ESI $^+$ ) 313.0201 (100%,  $\text{MH}^+$ ,  $\text{C}_{11}\text{H}_{12}\text{N}_4\text{O}_2^{80}\text{Se}$  requires 313.0198).

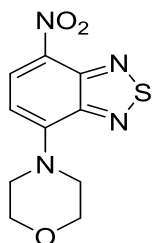
#### 4-(Morpholin-4-yl)-7-nitro-2,1,3-benzoxadiazole (71)



Prepared using chloride **1** (0.025 g, 0.125 mmol) and morpholine (0.013 g, 0.150 mmol) following general procedure C. Isolated as an orange crystalline solid (0.009 g, 30%);  $R_f$  0.48 (ethyl acetate: petroleum ether, 1:1); m.p. 218–210 °C (lit.<sup>209</sup> 227–228 °C);  $^1\text{H}$  NMR (400 MHz,  $\text{CDCl}_3$ ): 8.48 (1H, d,  $J$  8.9, ArCH), 6.36 (1H, d,  $J$  8.9, ArCH), 4.11 (4H, app.

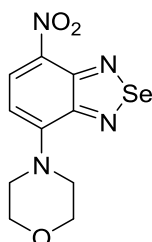
t,  $J$  4.7,  $2 \times \text{CH}_2$ ), 3.99 (4H, app. t,  $J$  4.7,  $2 \times \text{CH}_2$ ). All data in accordance with the literature.<sup>209</sup>

#### 4-(Morpholin-4-yl)-7-nitro-2,1,3-benzothiadiazole (72)



Prepared using bromide **5** (0.033 g, 0.125 mmol) and morpholine (0.013 g, 0.150 mmol) following general procedure C. Isolated as a dark orange crystalline solid (0.015 g, 45%);  $R_f$  0.64 (ethyl acetate: petroleum ether, 1:1); m.p. 192–194 °C;  $\nu_{\text{max}}$  (ATR)/ $\text{cm}^{-1}$  3293 (br, w), 3119 (w), 2924 (w), 2870 (w), 1602 (s), 1551 (s);  $^1\text{H}$  NMR (400 MHz,  $\text{CDCl}_3$ ): 8.63 (1H, d,  $J$  8.9, ArCH), 6.67 (1H, d,  $J$  8.9, ArCH), 4.08–4.04 (4H, m,  $2 \times \text{CH}_2$ ), 4.02–3.98 (4H, m,  $2 \times \text{CH}_2$ );  $^{13}\text{C}$  NMR (100 MHz,  $\text{CDCl}_3$ ): 149.3 (ArC), 148.5 (ArC), 147.8 (ArC), 131.8 (ArCH), 130.3 (ArC), 105.8 (ArCH), 66.6 ( $2 \times \text{CH}_2$ ), 49.6 ( $2 \times \text{CH}_2$ );  $m/z$  (ESI<sup>+</sup>) 289 (39%,  $[\text{M}+\text{Na}]^+$ ), 267.0545 (100,  $\text{MH}^+$ ,  $\text{C}_{10}\text{H}_{10}\text{N}_4\text{O}_3\text{S}$  requires 267.0546), 236 (16), 221 (28), 187 (75,  $\text{MH}^+ - \text{C}_4\text{H}_8\text{NO}$ ), 124 (19).

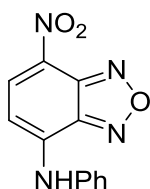
#### 4-(Morpholin-4-yl)-7-nitro-2,1,3-benzoselenadiazole (73)



Prepared using bromide **9** (0.038 g, 0.125 mmol) and morpholine (0.013 g, 0.150 mmol) following general procedure C. Isolated as a red powder (0.009 g, 23%);  $R_f$  0.37 (ethyl acetate: petroleum ether, 3:1); m.p. 180 °C (decomp.);  $\nu_{\text{max}}$  (ATR)/ $\text{cm}^{-1}$  2922 (w), 2855

(w), 1583 (m), 1525 (s), 1259 (s), 1020 (s);  $^1\text{H}$  NMR (400 MHz,  $\text{CDCl}_3$ ): 8.60 (1H, d,  $J$  8.8, ArCH), 6.53 (1H, d,  $J$  8.8, ArCH), 4.03–3.95 (8H, m,  $4 \times \text{CH}_2$ );  $^{13}\text{C}$  NMR (100 MHz,  $\text{CDCl}_3$ ): 154.0 (ArC), 153.6 (ArC), 150.0 (ArC), 132.7 (ArCH), 128.4 (ArC), 105.5 (ArCH), 67.0 ( $2 \times \text{CH}_2$ ), 50.2 ( $2 \times \text{CH}_2$ );  $m/z$  (ESI $^+$ ) 336 (15%,  $[\text{M}+\text{Na}]^+$ ), 314.9991 (100,  $\text{MH}^+$ ,  $\text{C}_{10}\text{H}_{10}\text{N}_4\text{O}_3$  $^{80}\text{Se}$  requires 314.9991).

#### 7-Nitro-*N*-phenyl-2,1,3-benzoxadiazol-4-amine (74)



Prepared using chloride **1** (0.025 g, 0.125 mmol) and aniline (0.014 g, 0.150 mmol) following general procedure C. Isolated as a red powder (0.013 g, 41%);  $R_f$  0.45 (dichloromethane); m.p. 116 °C;  $^1\text{H}$  NMR (400 MHz,  $\text{CDCl}_3$ ): 8.49 (1H, d,  $J$  8.6, ArCH), 7.81 (1H, br, s, NH), 7.58–7.52 (2H, m,  $2 \times \text{ArCH}$ ), 7.46–7.36 (3H, m,  $3 \times \text{ArCH}$ ), 6.76 (1H, d,  $J$  8.6, ArCH). Melting point not reported in the literature but all other data was in accordance.<sup>208</sup>

#### 7-Nitro-*N*-phenyl-2,1,3-benzothiadiazol-4-amine (75)



Prepared using bromide **5** (0.033 g, 0.125 mmol) and aniline (0.014 g, 0.150 mmol) following general procedure C. Isolated as an orange crystalline solid (0.008 g, 24%);  $R_f$  0.42 (ethyl acetate: petroleum ether, 1:3); m.p. 108 °C;  $^1\text{H}$  NMR (400 MHz,  $\text{CDCl}_3$ ): 8.65 (1H, d,  $J$  8.8, ArCH), 7.97 (1H, br, s, NH), 7.57–7.50 (2H, m,  $2 \times \text{ArCH}$ ), 7.47–7.42 (2H,



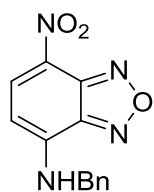
m, 2 × ArCH), 7.34 (1H, td, *J* 7.3, 1.1, ArCH), 7.01 (1H, d, *J* 8.8, ArCH). Melting point not reported in the literature but all other data was in accordance.<sup>210</sup>

#### 7-Nitro-*N*-phenyl-2,1,3-benzoselenadiazol-4-amine (76)



Prepared using bromide **9** (0.038 g, 0.125 mmol) and aniline (0.014 g, 0.150 mmol) following general procedure C. Isolated as a red solid (0.009 g, 23%); *R<sub>f</sub>* 0.40 (ethyl acetate: petroleum ether, 2:1); m.p. 120–122 °C;  $\nu_{\text{max}}$  (ATR)/cm<sup>-1</sup> 2923 (w), 1590 (m), 1538 (s), 1486 (s), 1261 (s); <sup>1</sup>H NMR (400 MHz, CDCl<sub>3</sub>): 8.67 (1H, d, *J* 8.8, ArCH), 8.12 (1H, br. s, NH), 7.56–7.30 (5H, m, 5 × ArCH), 6.87 (1H, d, *J* 8.8, ArCH); <sup>13</sup>C NMR (100 MHz, CDCl<sub>3</sub>): 137.3 (ArC), 134.8 (ArCH), 134.7 (ArC), 133.7 (ArC), 130.1 (ArCH), 126.0 (ArCH), 123.1 (ArCH), 122.3 (ArCH), 121.2 (ArC), 112.4 (ArC), 99.7 (ArCH), 91.9 (ArCH); *m/z* (ESI<sup>+</sup>) 320.9889 (100%, MH<sup>+</sup>, C<sub>12</sub>H<sub>8</sub>N<sub>4</sub>O<sub>2</sub><sup>80</sup>Se requires 320.9885).

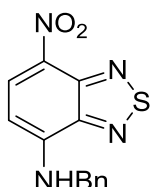
#### *N*-Benzyl-7-nitro-2,1,3-benzoxadiazol-4-amine (77)



Prepared using chloride **1** (0.025 g, 0.125 mmol) and benzylamine (0.016 g, 0.150 mmol) following general procedure C. Isolated as a brown crystalline solid (0.011 g, 33%); *R<sub>f</sub>* 0.59 (ethyl acetate: petroleum ether, 2:1); m.p. 210–211 °C (lit.<sup>211</sup> 214–215 °C); <sup>1</sup>H NMR (400 MHz, CDCl<sub>3</sub>): 8.50 (1H, d, *J* 8.7, ArCH), 7.50–7.37 (5H, m, 5 × ArCH), 6.54 (1H,

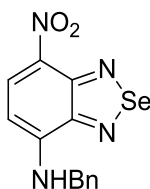
br. s, NH), 6.25 (1H, d, *J* 8.7, ArCH), 4.70 (2H, d, *J* 5.7, CH<sub>2</sub>). All data in accordance with the literature.<sup>211,212</sup>

### ***N*-Benzyl-7-nitro-2,1,3-benzothiadiazol-4-amine (78)**



Prepared using bromide **5** (0.033 g, 0.125 mmol) and benzylamine (0.016 g, 0.150 mmol) following general procedure *C*. Isolated as a dark yellow crystalline solid (0.006 g, 17%); *R*<sub>f</sub> 0.74 (ethyl acetate: petroleum ether, 1:2); m.p. 162 °C;  $\nu_{\text{max}}$  (ATR)/cm<sup>-1</sup> 2930 (w), 2854 (w), 1571 (s), 1211 (s); <sup>1</sup>H NMR (400 MHz, CDCl<sub>3</sub>): 8.66 (1H, d, *J* 8.8, ArCH), 7.47–7.36 (5H, m, 5 × ArCH), 6.70–6.63 (1H, m, NH), 6.44 (1H, d, *J* 8.8, ArCH), 4.71 (2H, d, *J* 5.8, CH<sub>2</sub>); <sup>13</sup>C NMR (100 MHz, CDCl<sub>3</sub>): 146.8 (ArC), 145.9 (ArC), 135.9 (ArC), 133.8 (ArCH), 132.8 (ArC), 129.3 (2 × ArCH), 128.4 (ArCH), 127.5 (2 × ArCH), 111.0 (ArC), 99.7 (ArCH), 47.7 (CH<sub>2</sub>); *m/z* (ESI<sup>+</sup>) 287.0596 (100%, MH<sup>+</sup>, C<sub>13</sub>H<sub>10</sub>N<sub>4</sub>O<sub>2</sub>S requires 287.0597).

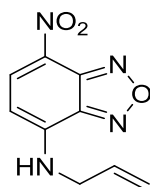
### ***N*-Benzyl-7-nitro-2,1,3-benzoselenadiazol-4-amine (79)**



Prepared using bromide **9** (0.038 g, 0.125 mmol) and benzylamine (0.016 g, 0.150 mmol) following general procedure *C*. Isolated as a red crystalline solid (0.005, 12%); *R*<sub>f</sub> 0.39 (ethyl acetate: petroleum ether, 1:1); m.p. 84–86 °C;  $\nu_{\text{max}}$  (ATR)/cm<sup>-1</sup> 2922 (m), 2854 (w), 1725 (w), 1549 (m), 1256 (s); <sup>1</sup>H NMR (400 MHz, CDCl<sub>3</sub>): 8.68 (1H, d, *J* 8.7, ArCH),

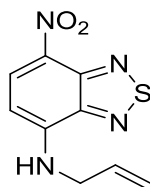
7.46–7.36 (5H, m,  $5 \times \text{ArCH}$ ), 6.81 (1H, m, NH), 6.28 (1H, d,  $J$  8.7, ArCH), 4.69 (2H, d,  $J$  5.8,  $\text{CH}_2$ );  $^{13}\text{C}$  NMR (100 MHz,  $\text{CDCl}_3$ ): 149.8 (ArC), 148.4 (ArC), 137.1 (ArC), 135.6 (ArCH), 134.6 (ArC), 129.5 ( $2 \times \text{ArCH}$ ), 128.4 (ArCH), 127.5 ( $2 \times \text{ArCH}$ ), 112.0 (ArC), 98.0 (ArCH), 47.8 ( $\text{CH}_2$ );  $m/z$  (ESI<sup>+</sup>) 335.0045 (100%,  $\text{MH}^+$ ,  $\text{C}_{13}\text{H}_{10}\text{N}_4\text{O}_2$ <sup>80</sup>Se requires 335.0042).

### 7-Nitro-*N*-(prop-2-en-1-yl)-2,1,3-benzoxadiazol-4-amine (80)



Prepared using chloride **1** (0.025 g, 0.125 mmol) and allylamine (0.009 g, 0.150 mmol) following general procedure C. Isolated as an orange crystalline solid (0.003 g, 11%);  $R_f$  0.63 (ethyl acetate: petroleum ether, 1:2); m.p. 105–107 °C (lit.<sup>213</sup> 106–108 °C);  $^1\text{H}$  NMR (400 MHz,  $\text{CDCl}_3$ ): 8.69 (1H, d,  $J$  8.8, ArCH), 6.43 (1H, d,  $J$  8.8, ArCH), 6.00 (1H, ddt,  $J$  17.2, 10.4, 5.5,  $\text{CH}=\text{CH}_2$ ), 5.45–5.35 (2H, m,  $\text{CH}=\text{CH}_2$ ), 4.18 (2H, app. t,  $J$  5.5,  $\text{CH}_2$ ). All data in accordance with the literature.<sup>213</sup>

### 7-Nitro-*N*-(prop-2-en-1-yl)-2,1,3-benzothiadiazol-4-amine (81)



Prepared using bromide **5** (0.033 g, 0.125 mmol) and allylamine (0.009 g, 0.150 mmol) following general procedure C. Isolated as an orange solid (0.002 g, 6%);  $R_f$  0.56 (ethyl acetate: petroleum ether, 1:2); m.p. 82 °C;  $\nu_{\text{max}}$  (ATR)/ $\text{cm}^{-1}$  2926 (w), 2851 (w), 1540 (m), 1240 (s);  $^1\text{H}$  NMR (400 MHz,  $\text{CDCl}_3$ ): 8.69 (1H, d,  $J$  8.8, ArCH), 6.47 (1H, br. s, NH),

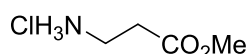
6.43 (1H, d, *J* 8.8, ArCH), 6.07–5.96 (1H, m, CH=CH<sub>2</sub>), 5.45–5.35 (2H, m, CH=CH<sub>2</sub>), 4.17 (2H, app. t, *J* 5.6, CH<sub>2</sub>); <sup>13</sup>C NMR (100 MHz, CDCl<sub>3</sub>): 147.1 (ArC), 133.2 (ArC), 129.6 (ArCH), 125.4 (ArC), 124.2 (ArCH), 119.4 (ArC), 118.8 (CH=CH<sub>2</sub>), 100.0 (CH=CH<sub>2</sub>), 46.0 (NCH<sub>2</sub>); *m/z* (ESI<sup>+</sup>) 237.0442 (100%, MH<sup>+</sup>, C<sub>9</sub>H<sub>8</sub>N<sub>4</sub>O<sub>2</sub>S requires 237.0441).

### 7-Nitro-*N*-(prop-2-en-1-yl)-2,1,3-benzoselenadiazol-4-amine (82)



Prepared using bromide **9** (0.038 g, 0.125 mmol) and allylamine (0.009 g, 0.150 mmol) following general procedure C. Isolated as a red solid (0.008 g, 23%); *R*<sub>f</sub> 0.49 (ethyl acetate: petroleum ether, 4:1); m.p. 91–93 °C; *v*<sub>max</sub> (ATR)/cm<sup>-1</sup> 2923 (w), 1546 (m), 1528 (s); <sup>1</sup>H NMR (400 MHz, CDCl<sub>3</sub>): 8.70 (1H, d, *J* 8.8, ArCH), 6.64 (1H, br. s, NH), 6.26 (1H, d, *J* 8.8, ArCH), 6.07–5.95 (1H, m, CH=CH<sub>2</sub>), 5.45–5.33 (2H, m, CH=CH<sub>2</sub>), 4.17 – 4.12 (2H, m, CH<sub>2</sub>); <sup>13</sup>C NMR (100 MHz, CDCl<sub>3</sub>): 152.3 (ArC), 146.8 (ArC), 143.4 (ArCH), 138.0 (ArC), 125.3 (ArCH), 119.7 (ArC), 118.5 (CH=CH<sub>2</sub>), 97.8 (CH=CH<sub>2</sub>), 46.0 (NCH<sub>2</sub>); *m/z* (ESI<sup>+</sup>) 285.9882 (100%, MH<sup>+</sup>, C<sub>9</sub>H<sub>8</sub>N<sub>4</sub>O<sub>2</sub><sup>80</sup>Se requires 284.9885).

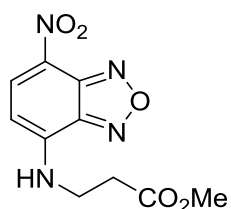
### β-Alanine methyl ester (hydrochloride salt, **21**)



3-Aminopropionic acid (3.0 g, 33.7 mmol) was suspended in methanol (20 mL) and cooled to 0 °C. Thionyl chloride (5.1 mL, 70.8 mmol, 2.1 eq.) was added dropwise over

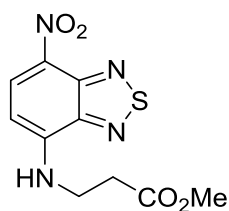
5 minutes. The mixture was warmed to room temperature then heated at reflux for 2 h. Solvent was removed *in vacuo* and the resulting solid was triturated using hot methanol and cold diethyl ether to furnish the hydrochloride salt of the methylated amino acid as a pale yellow solid (4.07 g, 87%); m.p. 95–97 °C (lit.<sup>214</sup> 101 °C); <sup>1</sup>H NMR (400 MHz, MeOD): 3.76 (3H, s, OCH<sub>3</sub>), 3.23 (2H, t, *J* 6.6, NCH<sub>2</sub>), 2.78 (2H, t, *J* 6.6, CH<sub>2</sub>). All data in accordance with the literature.<sup>214</sup>

***N*-(7-Nitro-2,1,3-benzoxadiazol-4-yl)-β-Alanine methyl ester (86)**



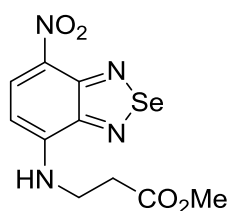
Prepared using chloride **1** (0.025 g, 0.125 mmol) and β-alanine methyl ester (**21**, 0.015 g, 0.150 mmol) following general procedure C. Isolated as an orange solid (0.003 g, 8%); *R*<sub>f</sub> 0.39 (ethyl acetate: petroleum ether, 1:1); m.p. 121–125 °C; *v*<sub>max</sub> (ATR)/cm<sup>-1</sup> 2942 (m), 1738 (m, C=O), 1559 (m), 1280 (s, CO); <sup>1</sup>H NMR (400 MHz, CDCl<sub>3</sub>): 8.52 (1H, d, *J* 8.7, ArCH), 6.70 (1H, br. s, NH), 6.25 (1H, d, *J* 8.7, ArCH), 3.90–3.82 (2H, m, NCH<sub>2</sub>), 3.79 (3H, s, CH<sub>3</sub>), 2.83 (2H, t, *J* 6.1, CH<sub>2</sub>); <sup>13</sup>C NMR (100 MHz, CDCl<sub>3</sub>): 178.5 (C=O), 139.1 (ArC), 138.8 (ArC), 136.9 (ArC), 132.9 (ArCH), 98.4 (ArCH), 94.6 (ArC), 52.4 (OCH<sub>3</sub>), 38.9 (CH<sub>2</sub>), 33.0 (CH<sub>2</sub>); *m/z* (ESI<sup>+</sup>) 266.0653 (100%, MH<sup>+</sup>, C<sub>10</sub>H<sub>10</sub>N<sub>4</sub>O<sub>5</sub> requires 266.0651).

***N*-(7-Nitro-2,1,3-benzothiadiazol-4-yl)- $\beta$ -Alanine methyl ester (87)**



Prepared using bromide **5** (0.033 g, 0.125 mmol) and  $\beta$ -alanine methyl ester (**21**, 0.015 g, 0.150 mmol) following general procedure *C*. Isolated as a dark yellow solid (0.005 g, 15%);  $R_f$  0.52 (ethyl acetate: petroleum ether, 1:1); m.p. 118–120 °C;  $\nu_{\max}$  (ATR)/ $\text{cm}^{-1}$  2925 (w), 1732 (m, C=O), 1569 (s), 1309 (s, CO);  $^1\text{H NMR}$  (400 MHz,  $\text{CDCl}_3$ ): 8.69 (1H, d,  $J$  8.8, ArCH), 6.77 (1H, br. s, NH), 6.45 (1H, d,  $J$  8.8, ArCH), 3.88–3.81 (2H, m, NCH<sub>2</sub>), 3.78 (3H, s, CH<sub>3</sub>), 2.83 (2H, t,  $J$  6.1, CH<sub>2</sub>);  $^{13}\text{C NMR}$  (100 MHz,  $\text{CDCl}_3$ ): 174.9 (C=O), 138.4 (ArC), 137.2 (ArC), 136.4 (ArC), 133.8 (ArCH), 98.9 (ArCH), 94.5 (ArC), 52.4 (OCH<sub>3</sub>), 38.8 (CH<sub>2</sub>), 33.0 (CH<sub>2</sub>);  $m/z$  (ESI<sup>+</sup>) 283.0496 (100%, MH<sup>+</sup>, C<sub>10</sub>H<sub>10</sub>N<sub>4</sub>O<sub>4</sub>S requires 283.0496).

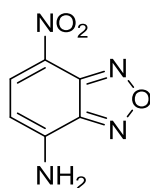
***N*-(7-Nitro-2,1,3-benzoselenadiazol-4-yl)- $\beta$ -Alanine methyl ester (88)**



Prepared using bromide **9** (0.038 g, 0.125 mmol) and  $\beta$ -alanine methyl ester (**21**, 0.015 g, 0.150 mmol) following general procedure *C*. Isolated as a red solid (0.004 g, 10%);  $R_f$  0.41 (ethyl acetate: petroleum ether, 3:1); m.p. 94–96 °C;  $\nu_{\max}$  (ATR)/ $\text{cm}^{-1}$  2922 (m), 1735 (m, C=O), 1549 (m), 1259 (s, CO);  $^1\text{H NMR}$  (400 MHz,  $\text{CDCl}_3$ ): 8.71 (1H, d,  $J$  8.1, ArCH), 6.90 (1H, br. s, NH), 6.28 (1H, d,  $J$  8.1, ArCH), 3.81 (2H, app. q,  $J$  6.3, NCH<sub>2</sub>),

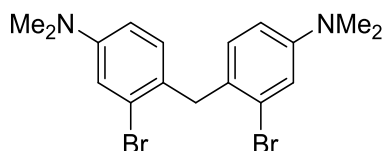
3.78 (3H, s, CH<sub>3</sub>), 2.83 (2H, t, *J* 6.3, CH<sub>2</sub>); <sup>13</sup>C NMR (100 MHz, CDCl<sub>3</sub>): 186.1 (C=O), 144.6 (ArC), 143.2 (ArC), 141.2 (ArC), 135.6 (ArCH), 97.5 (ArCH), 94.8 (ArC), 52.6 (OCH<sub>3</sub>), 39.2 (CH<sub>2</sub>), 33.1 (CH<sub>2</sub>); *m/z* (ESI<sup>+</sup>) 330.9940 (100%, MH<sup>+</sup>, C<sub>10</sub>H<sub>10</sub>N<sub>4</sub>O<sub>4</sub><sup>80</sup>Se requires 330.9940).

### 7-Nitro-2,1,3-benzothiadiazol-4-amine (89)



Prepared using chloride **1** (0.025 g, 0.125 mmol) and propargyl amine (0.0083g, 0.150 mmol) following general procedure C. Isolated as a red/orange solid (0.0087 g, 32%); R<sub>f</sub> 0.57 (ethyl acetate: petroleum ether, 2:1); m.p. 110 °C; *v*<sub>max</sub> (ATR)/cm<sup>-1</sup> 3374, 3339 (m, NH<sub>2</sub>), 1562 (m), 1304 (s); <sup>1</sup>H NMR (400 MHz, CDCl<sub>3</sub>): 8.57 (1H, d, *J* 8.3, ArCH), 6.44 (1H, d, *J* 8.3, ArCH), 5.74 (2H, br. s, NH<sub>2</sub>); *m/z* (ESI<sup>-</sup>) 179.0217 (100%, [M-H]<sup>-</sup>, C<sub>6</sub>H<sub>4</sub>N<sub>4</sub>O<sub>3</sub> requires 179.0211), 112 (30). Melting point not reported in the literature but all other data was in accordance.<sup>215,216</sup>

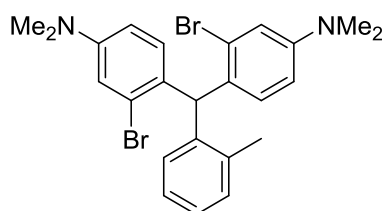
### 4,4'-Methylenebis(3-bromo-*N,N*-dimethylaniline) (39)



*N,N*-Dimethyl-3-bromoaniline (0.50 g, 2.5 mmol) and hexamethylenetetramine (0.70 g, 5.0 mmol, 2 eq.) were dissolved in acetic acid (3 mL) and heated at 60 °C for 24 h. On complete reaction, the mixture was poured onto distilled water (20 mL) and extracted

with dichloromethane (3 × 20 mL). The combined organic layers were washed with saturated sodium bicarbonate (2 × 20 mL) and brine (20 mL), dried with magnesium sulfate, filtered, and evaporated to dryness. The resulting red oil was purified using flash column chromatography eluting with petroleum ether and ethyl acetate (9:1) to give the named product as a beige solid (0.29 g, 57%);  $R_f$  0.47 (ethyl acetate: petroleum ether, 1:9); m.p. 96–98 °C (lit.<sup>217</sup> 97–99 °C);  $^1\text{H NMR}$  (400 MHz,  $\text{CDCl}_3$ ): 6.99 (2H, d,  $J$  2.6, 2 × ArCH), 6.89 (2H, d,  $J$  8.5, 2 × ArCH), 6.62 (2H, dd,  $J$  8.5, 2.6, 2 × ArCH), 4.05 (2H, s,  $\text{CH}_2$ ), 2.95 (12H, s, 2 × N[ $\text{CH}_3$ ]<sub>2</sub>). All data in accordance with the literature.<sup>173,217</sup>

#### 4,4'-[(2-Methylphenyl)methylene]bis[3-bromo-*N,N*-dimethyl]-benzenamine (43)



*N,N*-Dimethyl-3-bromoaniline (0.86 g, 4.31 mmol, 2 eq.), 2-methylbenzaldehyde (0.26 g, 2.15 mmol, 1 eq.), and titanium(IV) chloride (0.41 g, 2.15 mmol, 1 eq.) were dissolved in dichloromethane (15 mL). The mixture was heated at reflux for 16 h then returned to room temperature. Distilled water (10 mL) and diethyl ether (10 mL) were added and the mixture stirred until all residues had dissolved. The layers were separated and the organic fraction dried over magnesium sulfate, filtered and evaporated to dryness. The resulting residue was triturated in chloroform and methanol over ice to give the named product as a fine white powder (0.80 g, 75%); m.p. 188–190 °C;  $^1\text{H NMR}$  (400 MHz,  $\text{CDCl}_3$ ): 7.15–7.02 (3H, m, ArCH), 6.97 (2H, br. s, ArCH), 6.74 (1H, d,  $J$  7.7, ArCH), 6.64 (2H, d,  $J$  8.6, ArCH), 6.57 (2H, br. d,  $J$  8.6, ArCH), 5.98 (1H, s, CH), 2.94 (12H, s, 2 × N[ $\text{CH}_3$ ]<sub>2</sub>), 2.22 (3H, s, ArCH<sub>3</sub>);  $m/z$  (ESI<sup>+</sup>) 505.0503 (51%,  $\text{MH}^+$ ,  $\text{C}_{24}\text{H}_{26}^{81}\text{Br}_2\text{N}_2$  requires 505.0500),

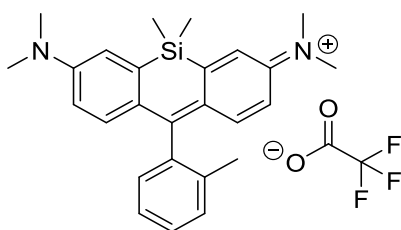


503.0522 (100, C<sub>24</sub>H<sub>26</sub><sup>79</sup>Br<sup>81</sup>BrN<sub>2</sub>), 501.0536 (51, C<sub>24</sub>H<sub>26</sub><sup>79</sup>Br<sub>2</sub>N<sub>2</sub>). Melting point not reported in the literature but all other data was in accordance.<sup>173</sup>

#### **General procedure *D* for the synthesis of heteroaromatic rhodamine derivatives**

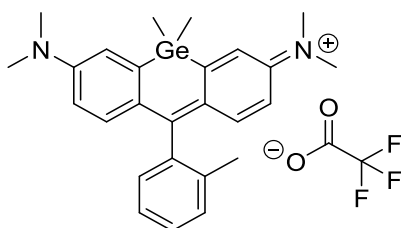
A sample of bis-aryl bromide **43** (0.050 g, 0.1 mmol, 1 eq.) was dissolved in anhydrous THF (5 mL) under a nitrogen atmosphere. The mixture was cooled to -78 °C and stirred for five minutes before the dropwise addition of *s*-BuLi (1.4 M in hexanes, 0.22 mL, 3 eq.). The mixture was stirred for 90 minutes at -78 °C. The electrophile (2 eq.) was added at -78 °C and the mixture was returned to room temperature and stirred for 16 h. The reaction was quenched with hydrochloric acid (1 M, 2 mL) then treated with K<sub>2</sub>CO<sub>3</sub> (5 mL). The organic phase was separated, dried over magnesium sulfate, filtered, and evaporated to dryness. The residue was redissolved in dichloromethane (5 mL) and chloranil (5 eq.) was added. The reaction was stirred for a further 2 h before evaporating to dryness and initial purification using flash column chromatography on silica gel eluting with dichloromethane and methanol (4:1). The resulting residue was stirred in a mixture of dichloromethane and trifluoroacetic acid (1:1, 5 mL). Title compounds were isolated using preparative HPLC purification in a mixture of acetonitrile and 0.1% TFA in Milli-Q water.

***N*-(7-[Dimethylamino]-5,5-dimethyl-10-[*o*-tolyl]dibenzo[*b,e*]silin-3[5*H*]-ylidene)-*N*-methylmethanaminium 2,2,2-trifluoroacetate (SiR, 48)**



Prepared using dichlorodimethylsilicon (0.026 g, 0.2 mmol) as the electrophile following general procedure *D*. Isolated as a deep blue solid (0.005 g, 8%);  $R_f$  0.62 (MeOH: DCM, 1:4); m.p. 176 °C;  $^1\text{H NMR}$  (400 MHz,  $\text{CDCl}_3$ ): 7.45 (1H, app. t,  $J$  7.5, ArCH), 7.36 (2H, d,  $J$  7.5, 2  $\times$  ArCH), 7.20 (2H, s, 2  $\times$  ArCH), 7.14–7.07 (3H, m, 3  $\times$  ArCH), 6.62 (2H, d,  $J$  9.3, 2  $\times$  ArCH), 3.37 (12H, s, 2  $\times$  N[CH<sub>3</sub>]<sub>2</sub>), 2.05 (3H, s, ArCH<sub>3</sub>), 0.63 (3H, s, SiCH<sub>3</sub>), 0.61 (3H, s, SiCH<sub>3</sub>);  $m/z$  (ESI<sup>+</sup>) 399.2257 (100%, M<sup>+</sup>, C<sub>26</sub>H<sub>31</sub>N<sub>2</sub>Si requires 399.2251). Melting point not reported in the literature but all other data was in accordance.<sup>70,218</sup>

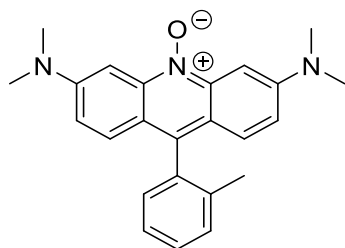
***N*-(7-[Dimethylamino]-5,5-dimethyl-10-[*o*-tolyl]dibenzo[*b,e*]germin-3[5*H*]-ylidene)-*N*-methylmethanaminium 2,2,2-trifluoroacetate (GeR, 49)**



Prepared using dichlorodimethyl germanium (0.034 g, 0.2 mmol) as the electrophile following general procedure *D*. Isolated as a deep blue crystalline solid (0.029 g, 60%);  $R_f$  0.63 (MeOH: DCM, 1:4); m.p. 152–155 °C (decomp.);  $^1\text{H NMR}$  (400 MHz,  $\text{CDCl}_3$ ): 7.41–7.32 (4H, m, 4  $\times$  ArCH), 7.23 (2H, d,  $J$  2.9, 2  $\times$  ArCH), 6.97 (2H, d,  $J$  9.6, 2  $\times$  ArCH), 6.61 (2H, dd  $J$  9.6, 2.9, 2  $\times$  ArCH), 3.41 (12H, s, 2  $\times$  N[CH<sub>3</sub>]<sub>2</sub>), 2.05 (3H, s,

ArCH<sub>3</sub>), 0.83 (3H, s, GeCH<sub>3</sub>), 0.81 (3H, s, GeCH<sub>3</sub>); <sup>13</sup>C NMR (100 MHz, CDCl<sub>3</sub>): 169.3 (ArCH), 153.8 (ArC), 152.7 (ArC), 141.9 (ArCH), 139.1 (ArC), 135.7 (ArC), 130.3 (ArCH), 128.8 (ArCH), 127.3 (ArC), 125.7 (ArCH), 120.8 (ArCH), 114.2 (ArC), 113.7 (ArCH), 41.2 (2 × N[CH<sub>3</sub>]<sub>2</sub>), 19.4 (ArCH<sub>3</sub>), -0.3 (GeCH<sub>3</sub>), -0.4 (GeCH<sub>3</sub>); *m/z* (ESI<sup>+</sup>) 445.1701 (100%, M<sup>+</sup>, C<sub>26</sub>H<sub>31</sub>N<sub>2</sub><sup>74</sup>Ge requires 445.71694). Melting point and <sup>13</sup>C NMR spectrum not reported in the literature but all other data was in accordance.<sup>70</sup>

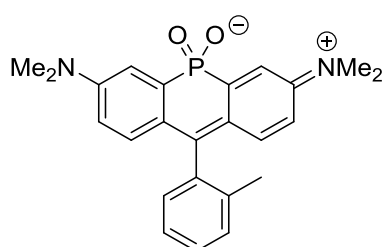
### 3,6-bis(Dimethylamino)-9-(*o*-tolyl)acridine 10-oxide (NOR, 51)



A sample of *bis*-aryl bromide **43** (0.050 g, 0.1 mmol, 1 eq.) was dissolved in anhydrous THF (5 mL) under a nitrogen atmosphere. The mixture was cooled to -78 °C and stirred for five minutes before the dropwise addition of *s*-BuLi (1.4 M in hexanes, 0.25 mL, 3 eq.). The mixture was stirred for 90 minutes at -78 °C. *i*-Pentyl nitrite (0.023 g, 0.2 mmol, 2 eq.) was added at -78 °C and the mixture was returned to room temperature and stirred for 16 h. The mixture was quenched with hydrochloric acid (1 M, 2 mL) then treated with K<sub>2</sub>CO<sub>3</sub> (5 mL). The organic phase was separated, dried over magnesium sulfate, filtered, and evaporated to dryness. Purification using flash column chromatography on silica gel eluting with 0–7.5% methanol in DCM gave the product as a red solid (0.017 g, 46%); *R<sub>f</sub>* 0.46 (1:9 MeOH: DCM); m.p. 116 °C (decomp.); *v*<sub>max</sub> (ATR)/cm<sup>-1</sup> 3480 and 3362 (OH from solvent), 1589 (s); <sup>1</sup>H NMR (400 MHz, CDCl<sub>3</sub>): 7.85 (2H, d, *J* 2.2, ArCH), 7.50–7.34 (3H, m, ArCH), 7.29 (2H, d, *J* 3.0, ArCH), 7.24 (1H, d, *J* 7.6, ArCH), 7.00 (2H, dd, *J* 9.5 2.6, ArCH), 3.22 (12H, s, 2 × N[CH<sub>3</sub>]<sub>2</sub>), 1.92 (3H, s, ArCH<sub>3</sub>); <sup>13</sup>C NMR (100 MHz,

CDCl<sub>3</sub>): 152.1 (2 × ArC), 141.1 (2 × ArC), 137.5 (ArC), 135.5 (ArC), 130.7 (ArCH), 130.1 (2 × ArCH), 128.4 (ArCH), 128.4 (ArCH), 125.7 (ArCH), 117.5 (2 × ArC), 115.3 (2 × ArCH), 103.0 (ArC), 94.6 (2 × ArCH), 40.4 (2 × N[CH<sub>3</sub>]<sub>2</sub>), 19.7 (ArCH<sub>3</sub>); *m/z* (ESI<sup>+</sup>) 372.2080 (100%, MH<sup>+</sup>, C<sub>24</sub>H<sub>25</sub>N<sub>3</sub>O requires 372.2070), 356.2131 (52, MH<sup>+</sup> – O).

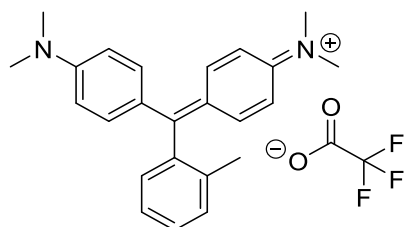
**3-(Dimethylamino)-6-(dimethyliminio)-9-(2-methylphenyl)-10-oxo-10λ<sup>5</sup>-acridophosphin-10-olate (P[V]R, 53)**



A sample of *bis*-aryl bromide **43** (0.050 g, 0.1 mmol, 1 eq.) was dissolved in anhydrous THF (5 mL) under a nitrogen atmosphere. The mixture was cooled to -78 °C and stirred for five minutes before the dropwise addition of *s*-BuLi (1.4 M in hexanes, 0.25 mL, 3 eq.). The mixture was stirred for 90 minutes at -78 °C. Ethyl dichlorophosphite (0.030 g, 0.2 mmol, 2 eq.) was added at -78 °C and the mixture was returned to room temperature and stirred for 16 h. The reaction was quenched with hydrochloric acid (1 M, 2 mL) then treated with K<sub>2</sub>CO<sub>3</sub> (5 mL). The organic phase was separated, dried over magnesium sulfate, filtered, and evaporated to dryness. The residue was stirred in a solution of hydrogen peroxide (30% w/w in H<sub>2</sub>O, 10 mL) for 3 h then quenched with saturated aqueous sodium sulfate (20 mL). The product was extracted using dichloromethane (3 × 20 mL), and the collected organic phases were combined, dried over magnesium sulfate, filtered, and evaporated. The residue was redissolved in dichloromethane (5 mL) and chloranil (5 eq.) was added. The reaction was stirred for a further 2 h before evaporating to dryness and initial purification using flash column chromatography on silica gel eluting

with dichloromethane and methanol (4:1). The blue residue was stirred in a mixture of DCM and trifluoroacetic acid (1:1, 5 mL). The title compound was isolated using preparative HPLC purification in a mixture of acetonitrile and 0.1% TFA in Milli-Q water as a dark blue solid (0.004 g, 7%);  $R_f$  0.31 (MeOH: DCM, 1:4); m.p. 122–123 °C;  $\nu_{\max}$  (ATR)/ $\text{cm}^{-1}$  2962 (w), 1678 (s), 1581 (s), 1175 (s, P=O);  $^1\text{H NMR}$  (400 MHz,  $\text{CDCl}_3$ ): 7.80 (2H, dd,  $J$  7.8, 2.8,  $2 \times \text{ArCH}$ ), 7.36 (2H, d,  $J$  7.8,  $2 \times \text{ArCH}$ ), 7.19–7.14 (2H, m,  $2 \times \text{ArCH}$ ), 7.01 (2H, dd,  $J$  9.4, 6.2,  $2 \times \text{ArCH}$ ), 6.57 (2H, dd,  $J$  9.4, 2.8,  $2 \times \text{ArCH}$ ), 3.38 (12H, s,  $2 \times \text{N}[\text{CH}_3]_2$ ), 2.08 (3H, s,  $\text{ArCH}_3$ );  $m/z$  (ESI $^+$ ) 405.1728 (100%,  $\text{MH}^+$ ,  $\text{C}_{24}\text{H}_{25}\text{N}_2\text{O}_2\text{P}$  requires 405.1726). Melting point and IR spectrum not reported in the literature but all other data was in accordance.<sup>173</sup>

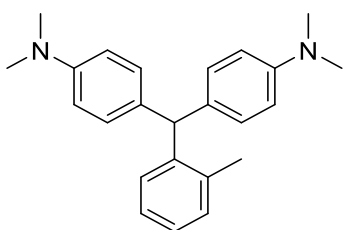
***N*-(4-[[4-(Dimethylamino)phenyl]{*o*-tolyl}methylene]cyclohexa-2,5-dien-1-ylidene)-*N*-methylmethanaminium chloride (HR, 57)**



A sample of bis-aryl bromide **43** (0.050 g, 0.1 mmol, 1 eq.) was dissolved in anhydrous THF (5 mL) under a nitrogen atmosphere. The mixture was cooled to -78 °C and stirred for five minutes before the dropwise addition of *s*-BuLi (1.4 M in hexanes, 0.25 mL, 3 eq.). The mixture was stirred for 90 minutes at -78 °C. The mixture was returned to room temperature and stirred for 16 h. The reaction was quenched with hydrochloric acid (1 M, 2 mL) then treated with  $\text{K}_2\text{CO}_3$  (5 mL). The organic phase was separated, dried over magnesium sulfate, filtered, and evaporated to dryness. The residue was redissolved in dichloromethane (5 mL) and chloranil (5 eq.) was added. The reaction was stirred for a

further 2 h before evaporating to dryness and initial purification using flash column chromatography on silica gel eluting with dichloromethane and methanol (4:1) to give the named product as a blue solid (0.027 g, 78%);  $R_f$  0.52 (MeOH: DCM, 1:4); m.p. 100 °C (decomp.);  $\nu_{\max}$  (ATR)/ $\text{cm}^{-1}$  1678 (s), 1567 (s), 1106 (s);  $^1\text{H}$  NMR (400 MHz,  $\text{CDCl}_3$ ): 7.50 (1H, app. t,  $J$  7.6, ArCH), 7.43 – 7.29 (6H, m,  $6 \times$  ArCH), 7.07 (1H, d,  $J$  7.0, ArCH), 6.97 (4H, d,  $J$  9.1,  $4 \times$  ArCH), 3.40 (12H, s,  $2 \times$  N[CH<sub>3</sub>]<sub>2</sub>), 1.95 (3H, s, ArCH<sub>3</sub>);  $^{13}\text{C}$  NMR (100 MHz,  $\text{CDCl}_3$ ): 176.7 (ArC), 157.0 ( $2 \times$  ArC), 140.1 ( $4 \times$  ArCH), 139.2 (ArC), 139.2 (ArC), 132.9 (ArCH), 131.3 (ArCH), 131.1 (ArCH), 127.4 ( $2 \times$  ArC), 125.7 (ArCH), 114.0 ( $4 \times$  ArCH), 41.0 ( $2 \times$  N[CH<sub>3</sub>]<sub>2</sub>), 20.3 (ArCH<sub>3</sub>);  $m/z$  (ESI<sup>+</sup>) 345.2325 (28%, MH<sup>+</sup>, C<sub>24</sub>H<sub>27</sub>N<sub>2</sub> requires 345.2325), 173 (100).

#### 4,4'-(*o*-Tolylmethylene)bis(*N,N*-dimethylaniline) (58)



A sample of *bis*-aryl bromide **43** (0.050 g, 0.1 mmol, 1 eq.) was dissolved in anhydrous THF (5 mL) under a nitrogen atmosphere. The mixture was cooled to -78 °C and stirred for 5 minutes before the dropwise addition of *s*-BuLi (1.4 M in hexanes, 0.25 mL, 3 eq.). The mixture was stirred for 90 minutes at -78 °C. The mixture returned to room temperature and stirred for 16 h. The reaction was quenched with hydrochloric acid (1 M, 2 mL) then treated with K<sub>2</sub>CO<sub>3</sub> (5 mL). The organic phase was separated, dried over magnesium sulfate and evaporated to dryness. The residue was purified using flash column chromatography on silica gel eluting with dichloromethane and methanol (4:1) and the title compound isolated as a white solid (0.006 g, 87%);  $R_f$  0.62 (MeOH: DCM,

1:4); m.p. 97–100 °C (lit.<sup>219</sup> 98–100 °C); <sup>1</sup>H NMR (400 MHz, CDCl<sub>3</sub>): 7.19–7.07 (4H, m, 4 × ArCH), 6.97–6.92 (4H, m, 4 × ArCH), 6.70–6.66 (4H, m, 4 × ArCH), 5.51 (1H, s, CH), 2.94 (12H, s, 2 × N[CH<sub>3</sub>]<sub>2</sub>), 2.25 (3H, s, ArCH<sub>3</sub>); *m/z* (ESI<sup>+</sup>) 345.2325 (100%, M<sup>+</sup>, C<sub>24</sub>H<sub>28</sub>N<sub>2</sub> requires 345.2325). Data in accordance with the literature.<sup>219,220</sup>

## 6 Appendix

### 6.1 Appendix 1: MatLab code used to obtain bleaching data

Code A:

```
function [ filelist ] = LM_filelist( folder )
%LM_FILELIST Summary of this function goes here
% Detailed explanation goes here

files=dir(folder);

if isempty(files)
    disp('Path not found. Typo?');
end

nfiles=size(files,1);

filelist=cell(nfiles,1);

%filelist=cellstr(filelist);

for i=1:nfiles;
    if (not(isempty(strfind(lower(files(i).name), 'tif'))))
        filelist{i}=fullfile(folder, files(i).name);
    end
end

filelist=filelist(cellfun('length', filelist)>0);

end
```

Code B:

```
function [ slash ] = LM_osslash()
%LM_OSSLASH Summary of this function goes here
% Detailed explanation goes here

%gets path delimiting slash character for current operating system
if (strcmp(getenv('os'), 'Windows_NT')==1)
    slash='\';
else
    slash='/';
end

end
```



### Code C:

```
path='\\Users\ntp13dj\OneDrive\Documents\CDT\PhD\Photophysics\NPSe
bleaching\2016 03 09\NPSe 10-4M\';
files=dir(path);
name=strcat(path,files(3).name);
M(:,1:2) = dlmread(name, '\t',17,0);

for I=4:length(files)
    name=strcat(path,files(I).name);

    M(:,I-1) = dlmread(name, '\t',17,1);

end

testa=sum(M(543:792,2:end));
plot(testa);
axis([0 1800 0 inf])
xlabel('Time / s')
ylabel('Area under spectrum')
legend({'Dye + MEA', 'Dye + MEA + GLOX', 'Dye'})
```

Absorption spectra were recorded at 1 second intervals throughout the course of the bleaching experiments. Each spectrum was stored in an individual text file. Code A enabled MatLab to go into each file in order to access the data. Code B ensures files can be read on OS X, MacOS and Windows operating systems. Code C plots a graph using Code A and Code B by taking the integral of each spectrum between specified wavelengths (in this case 543:792 means between 543-792 nm, and this range is changed for each dye). The axis dimensions are set using the command line “axis([0 1800 0 inf])” where, in this case, the x-axis starts at 0 and has a maximum of 1800, and the y-axis starts at 0 and the maxima is determined by the largest value in the dataset.

## 7 References

- 1 G. Sines and Y. A. Sakellarakis, *Am. J. Archaeology*, 1987, **91**, 191–196.
- 2 C. S. Ball, *Bios*, 1966, **37**, 51–60.
- 3 D. Bardell, *Bioscience*, 1983, **33**, 36–38.
- 4 J. B. West, *Am. J. Physiol. - Lung Cell. Mol. Physiol.*, 2013, **304**, 383–390.
- 5 E. Abbe, *Arch. für Mikroskopische Anat.*, 1873, **9**, 413–418.
- 6 H. von Helmholtz, *Ann. Phys. (N. Y.)*, 1874, 557.
- 7 P. Ellinger, *Biol. Rev.*, 1940, **15**, 323–347.
- 8 M. Minski, *Scanning*, 1988, **10**, 128–138.
- 9 M. Schrader and S. W. Hell, *Am. Inst. Phys.*, 1996, **69**, 3644–3646.
- 10 C. Kisielowski, P. Specht, S. M. Gyax, B. Barton, H. A. Calderon, J. H. Kang and R. Cieslinski, *Micron*, 2014, **68**, 186–193.
- 11 W. Kaiser and C. Garrett, *Phys. Rev. Lett.*, 1961, **7**, 229–231.
- 12 W. Denk, J. H. Strickler and W. W. Webb, *Science*, 1990, **248**, 73–6.
- 13 M. Pawlicki, H. A. Collins, R. G. Denning and H. L. Anderson, *Angew. Chem. Int. Ed.*, 2009, **48**, 3244–3266.
- 14 W. Denk and K. Svoboda, *Neuron*, 1997, **18**, 351–357.
- 15 K. Greger, J. Swoger and E. H. K. Stelzer, *Rev. Sci. Instrum.*, 2007, **78**, 23705-1-7.
- 16 Z. Lavagnino, F. C. Zanicchi, E. Ronzitti and A. Diaspro, *Opt. Express*, 2013, **21**, 5998–6008.

- 17 S. Wolf, W. Supatto, G. Debrégeas, P. Mahou, S. G. Kruglik, J.-M. Sintes, E. Beaufrepire and R. Candelier, *Nat. Methods*, 2015, **12**, 379–380.
- 18 B. Huang, M. Bates and X. Zhuang, *Annu. Rev. Biochem.*, 2009, **78**, 993–1016.
- 19 V. Westphal, S. O. Rizzoli, M. A. Lauterbach, D. Kamin, R. Jahn and S. W. Hell, *Science*, 2008, **320**, 246–249.
- 20 M. Reuss, J. Engelhardt and S. W. Hell, *Opt. Express*, 2010, **18**, 1049–1058.
- 21 D. Wildanger, B. R. Patton, H. Schill, L. Marseglia, J. P. Hadden, S. Knauer, A. Schonle, J. G. Rarity, J. L. O’Brien, S. W. Hell and J. M. Smith, *Adv. Mater.*, 2012, **24**, 309–313.
- 22 M. Fernández-Suárez and A. Ting, *Nat. Rev. Mol. Cell Biol.*, 2008, **9**, 929–943.
- 23 M. Friedrich, Q. Gan, V. Ermolayev and G. S. Harms, *Biophys. J.*, 2011, **100**, L43–L45.
- 24 B. R. Long, D. C. Robinson and H. Zhong, *Wiley Interdiscip. Rev. Syst. Biol. Med.*, 2014, **6**, 151–168.
- 25 E. Betzig, a. Lewis, a. Harootunian, M. Isaacson and E. Kratschmer, *Biophys. J.*, 1986, **49**, 269–279.
- 26 E. Betzig, J. Trautman, T. Harris, J. Weiner and R. Kostelak, *Science*, 1991, **251**, 1468–1470.
- 27 S. W. Hell, *Nat. Biotech.*, 2003, **21**, 1347–1355.
- 28 T. Hirschfeld, *Appl. Opt.*, 1976, **15**, 2965–2966.
- 29 W. Moerner and L. Kador, *Phys. Rev. Lett.*, 1989, **62**, 2535–2538.
- 30 E. Betzig and R. J. Chichester, *Science*, 1993, **262**, 1422–1425.

- 31 R. M. Dickson, A. B. Cubitt, R. Y. Tsien and W. E. Moerner, *Nature*, 1997, **388**, 355–358.
- 32 E. Betzig, G. H. Patterson, R. Sougrat, O. W. Lindwasser, S. Olenych, J. S. Bonifacino, M. W. Davidson, J. Lippincott-Schwartz and H. F. Hess, *Science*, 2006, **313**, 1642–1645.
- 33 S. T. Hess, T. P. K. Girirajan and M. D. Mason, *Biophys. J.*, 2006, **91**, 4258–4272.
- 34 M. Rust, M. Bates and X. Zhuang, *Nat. Methods*, 2006, **3**, 793–795.
- 35 H. Shroff, C. G. Galbraith, J. A. Galbraith and E. Betzig, *Nat. Methods*, 2008, **5**, 417–423.
- 36 D. N. Dempster, T. Morrow, R. Kankin and G. F. Thompson, *J. Chem. Soc. Faraday Trans. 2 Mol. Chem. Phys.*, 1972, **68**, 1479–1496.
- 37 M. Bates, B. Huang, G. Dempsey and X. Zhuang, *Science*, 2007, **317**, 1749–1753.
- 38 S. Shim, C. Xia, G. Zhong, H. P. Babcock, J. C. Vaughan, B. Huang, X. Wang, C. Xu, G.-Q. Bi and X. Zhuang, *PNAS*, 2012, **109**, 13978–13983.
- 39 R. D. Turner, A. F. Hurd, A. Cadby, J. K. Hobbs and S. J. Foster, *Nat. Commun.*, 2013, **4**, 1496.
- 40 A. Gahlmann and W. E. Moerner, *Nat. Rev. Microbiol.*, 2014, **12**, 9–22.
- 41 T. Klein, S. Proppert and M. Sauer, *Histochem. Cell Biol.*, 2014, **141**, 561–75.
- 42 D. Baddeley, I. D. Jayasinghe, C. Cremer, M. B. Cannell and C. Soeller, *Biophys. J.*, 2009, **96**, L22–L24.
- 43 J. Fölling, M. Bossi, H. Bock and R. Medda, *Nat. Methods*, 2008, **5**, 943–945.
- 44 M. Heilemann, S. van de Linde, M. Schüttpelz, R. Kasper, B. Seefeldt, A.

- Mukherjee, P. Tinnefeld and M. Sauer, *Angew. Chem. Int. Ed.*, 2008, **47**, 6172–6.
- 45 S. W. Englander, D. B. Calhoun and J. J. Englander, *Anal. Biochem.*, 1987, **161**, 300–306.
- 46 Y. Harada, K. Sakurada, T. Aoki, D. D. Thomas and T. Yanagida, *J. Mol. Biol.*, 1990, **216**, 49–68.
- 47 B. Fischer and J. Schumann, *J. Funct. Program.*, 2003, **13**, 483–508.
- 48 R. Henriques, M. Lelek, E. F. Fornasiero, F. Valtorta, C. Zimmer and M. M. Mhlanga, *Nat. Methods*, 2010, **7**, 339–340.
- 49 D. Sage, H. Kirshner, T. Pengo, N. Stuurman, J. Min, S. Manley and M. Unser, *Nat. Methods*, 2015, **12**, 1–12.
- 50 M. Ovesný, P. Křížek, J. Borkovec, Z. Švindrych and G. M. Hagen, *Bioinformatics*, 2014, **30**, 2389–2390.
- 51 C. a Schneider, W. S. Rasband and K. W. Eliceiri, *Nat. Methods*, 2012, **9**, 671–675.
- 52 J. Schindelin, I. Arganda-Carreras, E. Frise, V. Kaynig, M. Longair, T. Pietzsch, S. Preibisch, C. Rueden, S. Saalfeld, B. Schmid, J.-Y. J.-Y. Tinevez, D. J. White, V. Hartenstein, K. Eliceiri, P. Tomancak, A. Cardona, K. Liceiri, P. Tomancak and C. A., *Nat. Methods*, 2012, **9**, 676–682.
- 53 B. Huang, W. Wang, M. Bates and X. Zhuang, *Science*, 2008, **319**, 810–813.
- 54 K. Xu, H. P. Babcock and X. Zhuang, *Nat. Methods*, 2012, **9**, 185–188.
- 55 S. R. P. Pavani, M. A. Thompson, J. S. Biteen, S. J. Lord, N. Liu, R. J. Twieg, R. Piestun and W. E. Moerner, *PNAS*, 2009, **106**, 2995–2999.
- 56 M. Heilemann, S. van de Linde, A. Mukherjee and M. Sauer, *Angew. Chem. Int.*

- Ed.*, 2009, **48**, 6903–6908.
- 57 A. M. Bittel, A. Nickerson, I. S. Saldivar, N. J. Dolman, X. Nan and S. L. Gibbs, *Sci. Rep.*, 2016, **6**, 29687.
- 58 M. Bates, T. Blosser and X. Zhuang, *Phys. Rev. Lett.*, 2005, **94**, 108101.
- 59 S. Nanguneri, B. Flottmann, F. Herrmannsdörfer, T. Kuner and M. Heilemann, *Microsc. Res. Tech.*, 2014, **77**, 510–516.
- 60 S. N. Uno, D. K. Tiwari, M. Kamiya, Y. Arai, T. Nagai and Y. Urano, *Microscopy*, 2015, **64**, 263–277.
- 61 D. M. Chudakov, S. Lukyanov and K. A. Lukyanov, *Trends Biotechnol.*, 2005, **23**, 605–613.
- 62 A. Shivanandan, H. Deschout, M. Scarselli and A. Radenovic, *FEBS Lett.*, 2014, **588**, 3595–3602.
- 63 I. Chamma, O. Rossier, G. Giannone, O. Thoumine and M. Sainlos, *Nat. Protoc.*, 2017, **12**, 748–763.
- 64 L. Nahidiazar, A. V. Agronskaia, J. Broertjes, B. Den Van Broek and K. Jalink, *PLoS One*, 2016, **11**, 1–18.
- 65 J. Vogelsang, T. Cordes, C. Forthmann, C. Steinhauer and P. Tinnefeld, *PNAS*, 2009, **106**, 8107–12.
- 66 B. Dietzek, B. Brüggemann, P. Persson and A. Yartsev, *Chem. Phys. Lett.*, 2008, **455**, 13–19.
- 67 D. P. Mahoney, E. A. Owens, C. Fan, J.-C. Hsiang, M. M. Henary and R. M. Dickson, *J. Phys. Chem. B*, 2015, **119**, 4637–43.
- 68 P. Holzmeister, A. Gietl and P. Tinnefeld, *Angew. Chem. Int. Ed.*, 2014, 5685–

- 5688.
- 69 R. Zondervan, F. Kulzer, S. B. Orlinskii and M. Orrit, *J. Phys. Chem. A*, 2003, **107**, 6770–6776.
- 70 Y. Koide, Y. Urano, K. Hanaoka, T. Terai and T. Nagano, *ACS Chem. Biol.*, 2011, **6**, 600–608.
- 71 M. R. Detty and P. B. Merkel, *JACS*, 1990, **112**, 3845–3855.
- 72 M. R. Detty, P. N. Prasad, D. J. Donnelly, T. Ohulchansky, S. L. Gibson and R. Hilf, *Bioorg. Med. Chem.*, 2004, **12**, 2537–2544.
- 73 N. R. Conley, A. Dragulescu-Andrasi, J. Rao and W. E. Moerner, *Angew. Chem. Int. Ed.*, 2012, **51**, 3350–3353.
- 74 Y. S. Park, T. S. Kale, C.-Y. Nam, D. Choi and R. B. Grubbs, *Chem. Comm.*, 2014, 7964–7967.
- 75 M. S. Afzal, J.-P. Pitteloud and D. Buccella, *Chem. Comm.*, 2014, **50**, 11358–61.
- 76 C. W. Bird, *Tetrahedron*, 1992, **48**, 335–340.
- 77 A. T. Balaban, D. C. Oniciu and A. R. Katritzky, *Chem. Rev.*, 2004, **104**, 2777–2812.
- 78 A. R. Katritzky, I. P. Barczynski, G. Musumarra, D. Pisano and M. Szafranll, *JACS*, 1989, **111**, 7–15.
- 79 A. R. Katritzky and P. Barczynski, *J. Prakt. Chem.*, 1990, **332**, 885–897.
- 80 A. C. Benniston, A. Harriman, P. V. Patel and C. A. Sams, *Eur. J. Org. Chem.*, 2005, 4680–4686.
- 81 R. Elghanian, *Science*, 1997, **277**, 1078–1081.

- 82 J. Aizpurua, P. Hanarp, D. Sutherland, M. Käll, G. Bryant and F. García de Abajo, *Phys. Rev. Lett.*, 2003, **90**, 57401.
- 83 S. Santra, K. Wang, R. Tapeç and W. Tan, *J. Biomed. Opt.*, 2001, **6**, 160–166.
- 84 I. Halter, *JACS*, 1978, **100**, 8050–8055.
- 85 L. Pauling, *Am. Mineral.*, 1980, **65**, 321–323.
- 86 J. N. Clifford, T. D. M. Bell, P. Tinnefeld, M. Heilemann, S. M. Melnikov, J. Hotta, M. Sliwa, P. Dedecker, M. Sauer, J. Hofkens and E. K. L. Yeow, *J. Phys. Chem. B*, 2007, **111**, 6987–91.
- 87 M. E. Jung, T. A. Dong and X. Cai, *Tet. Lett.*, 2011, **52**, 2533–2535.
- 88 E. Kuru, H. V. Hughes, P. J. Brown, E. Hall, S. Tekkam, F. Cava, M. A. de Pedro, Y. V Brun and M. S. VanNieuwenhze, *Angew. Chem. Int. Ed.*, 2012, **51**, 12519–12523.
- 89 K. Sugihara, J. Vörös and T. Zambelli, *ACS Nano*, 2010, **4**, 5047–5054.
- 90 J. P. Richard, K. Melikov, E. Vives, C. Ramos, B. Verbeure, M. J. Gait, L. V Chernomordik and B. Lebleu, *J. Biol. Chem.*, 2003, **278**, 585–590.
- 91 B. Liu, F. Zeng, G. Wu and S. Wu, *Chem. Comm.*, 2011, **47**, 8913–8915.
- 92 L. X. Yu, Y. Liu, S. C. Chen, Y. Guan and Y. Z. Wang, *Chinese Chem. Lett.*, 2014, **25**, 389–396.
- 93 Y. K. Tsui, S. Devaraj and Y. P. Yen, *Sensors Actuators B Chem.*, 2012, **161**, 510–519.
- 94 Y. Shen, Y. Zhang, X. Zhang, C. Zhang, L. Zhang, J. Jin, H. Li and S. Yao, *Anal. Methods*, 2014, **6**, 4797–4802.



- 95 S. Chen, Z. Qin, T. Liu, X. Wu, Y. Y. Li, H. Liu, Y. Song and Y. Y. Li, *Phys. Chem. Chem. Phys.*, 2013, **15**, 12660–12666.
- 96 P. Ghosh and B. Everitt, *J. Med. Chem.*, 1974, **417**, 203–206.
- 97 R. Munigunti, S. Gathiaka, O. Acevedo, R. Sahu, B. Tekwani and A. I. Calderón, *Chem. Cent. J.*, 2013, **7**, 175–182.
- 98 T. Davidenko and I. Romanovskaya, *Pharm. Chem. J.*, 1989, **23**, 473–476.
- 99 R. Edwards, I. Cummins and P. Steel, *WO 2009/034396 A2*, 2009.
- 100 C. Pasquier, V. Charriere and H. J. Braun, *WO 02/22093 A1*, 2002.
- 101 E. Sawicki and A. Carr, *JOC*, 1958, **23**, 610–612.
- 102 S. Grivas, W. Tian, E. Ronne, S. Lindstrom and K. Olsson, *Acta Chem. Scand.*, 1993, **47**, 521–528.
- 103 M. Edin and S. Grivas, *ARKIVOC*, 2001, **2**, 144–153.
- 104 G. E. Garrett, G. L. Gibson, R. N. Straus, D. S. Seferos and M. S. Taylor, *JACS*, 2015, **137**, 4126–4133.
- 105 K. Pilgram and M. Zupan, *JOC*, 1971, **36**, 1970–1972.
- 106 M. Pagano, D. Castagnolo, M. Bernardini, A. L. Fallacara, I. Laurenzana, D. Deodato, U. Kessler, B. Pilger, L. Stergiou, S. Strunze, C. Tintori and M. Botta, *ChemMedChem*, 2014, **9**, 129–150.
- 107 M. J. Edelmann, J. Raimundo, N. F. Utesch and F. Diederich, *Helv. Chim. Acta*, 2002, **85**, 2195–2213.
- 108 S. Xu, Y. Liu, J. Li, Y. Wang and S. Cao, *Polym. Adv. Technol.*, 2010, **21**, 663–668.

- 109 P. J. Amal Joseph, S. Priyadarshini, M. Lakshmi Kantam and H. Maheswaran, *Tet. Lett.*, 2012, **53**, 1511–1513.
- 110 M. Makosza, J. Golixiski and J. Baran, *JOC*, 1984, **49**, 1488–1494.
- 111 A. R. Katritzky and K. S. Lorenzo, *JOC*, 1986, **51**, 5039–5040.
- 112 S. Seko and N. Kawamura, *JOC*, 1996, **61**, 442–443.
- 113 S. Seko, K. Miyake and N. Kawamura, *J. Chem. Soc. Perkin Trans. 1*, 1999, 1437–1444.
- 114 P. F. Pagoria, A. R. Mitchell and R. D. Schmidt, *JOC*, 1996, **61**, 2934–2935.
- 115 M. Grzegozek, B. Szpakiewicz and P. Kowalski, *ARKIVOC*, 2009, **2009**, 84–88.
- 116 U. Baettig, I. Bruce, N. J. Press and S. J. Watson, *PCT Int. Appl.*, 2010, **WO 2010/06**, 47.
- 117 L. Grehn, K. Gunnarsson and U. Ragnarsson, *J. Chem. Soc. Chem. Commun.*, 1985, 1317–1318.
- 118 P. Thansandote, D. G. Hulcoop, M. Langer and M. Lautens, *JOC*, 2009, **74**, 1673–1678.
- 119 H.-J. Niclas, B. Göhrmann and E. Gründemann, *Synth. Commun.*, 1989, **19**, 2789–2797.
- 120 S. Chen, Y. Li, C. Liu, W. Yang and Y. Li, *Eur. J. Org. Chem.*, 2011, 6445–6451.
- 121 S. Chen, N. Chen, Y. L. Yan, T. Liu, Y. Yu, Y. Li, H. Liu, Y. S. Zhao and Y. Li, *Chem. Comm.*, 2012, **48**, 9011–3.
- 122 J. L. Rogers, L. Bayeh, T. H. Scheuermann, J. Longgood, J. Key, J. Naidoo, L. Melito, C. Shokri, D. E. Frantz, R. K. Bruick, K. H. Gardner, J. B. MacMillan and

- U. K. Tambar, *J. Med. Chem.*, 2013, **56**, 1739–1747.
- 123 M. A. Bastrakov, A. M. Starosotnikov, A. A. Pavlov, I. L. Dalinger and S. A. Shevelev, *Chem. Heterocycl. Compd.*, 2016, **52**, 690–693.
- 124 T. Wang, D. R. Magnin and L. G. Hamann, *Org. Lett.*, 2003, **5**, 897–900.
- 125 M. Pal, K. Parasuraman and K. R. Yeleswarapu, *Heterocycles*, 2003, 6–9.
- 126 M. Santra, S. K. Ko, I. Shin and K. H. Ahn, *Chem Commun*, 2010, **46**, 3964–3966.
- 127 R. Balamurugan, C.-C. Chien, K.-M. Wu, Y.-H. Chiu and J.-H. Liu, *Analyst*, 2013, **138**, 1564–9.
- 128 D. Rambabu, S. Bhavani, N. K. Swamy, M. V. Basaveswara Rao and M. Pal, *Tet. Lett.*, 2013, **54**, 1169–1173.
- 129 W. Kaim and S. Kohlmann, *Inorg. Chem.*, 1990, **29**, 1898–1902.
- 130 Y. Yamashita, K. Ono, M. Tomura and S. Tanaka, *Tetrahedron*, 1997, **53**, 10169–10178.
- 131 N. Nijegorodov and R. Mabbs, *Spectrochim. Acta - Part A Mol. Biomol. Spectrosc.*, 2001, **57**, 1449–1462.
- 132 T. Y. Ohulchansky, D. J. Donnelly, M. R. Detty and P. N. Prasad, *J. Phys. Chem. B*, 2004, **108**, 8668–8672.
- 133 Y. Xiang, Y. Zhao, N. Xu, S. Gong, F. Ni, K. Wu, J. Luo, G. Xie, Z. Lu and C. Yang, *J. Mater. Chem. C*, 2017, **5**, 12204–12210.
- 134 J. Jona, W. Derbyshire and H. S. Gutowsky, *J. Phys. Chem.*, 1965, **69**, 1.
- 135 M. J. Frisch, G. W. Trucks, H. B. Schlegel, G. E. Scuseria, M. A. Robb, J. R. Cheeseman, G. Scalmani, V. Barone, B. Mennucci, G. A. Petersson, H. Nakatsuji,

- M. Caricato, X. Li, H. P. Hratchian, A. F. Izmaylov, J. Bloino, G. Zheng, J. L. Sonnenberg, M. Hada, M. Ehara, K. Toyota, R. Fukuda, J. Hasegawa, M. Ishida, T. Nakajima, Y. Honda, O. Kitao, H. Nakai, T. Vreven, J. A. J. Montgomery, J. E. Peralta, F. Ogliaro, M. Bearpark, J. J. Heyd, E. Brothers, K. N. Kudin, V. N. Staroverov, R. Kobayashi, J. Normand, K. Raghavachari, A. Rendell, J. C. Burant, S. S. Iyengar, J. Tomasi, M. Cossi, N. Rega, J. M. Millam, M. Klene, J. E. Knox, J. B. Cross, V. Bakken, C. Adamo, J. Jaramillo, R. Gomperts, R. E. Stratmann, O. Yazyev, A. J. Austin, R. Cammi, C. Pomelli, J. W. Ochterski, R. L. Martin, K. Morokuma, V. G. Zakrzewski, G. A. Voth, P. Salvador, J. J. Dannenberg, S. Dapprich, A. D. Daniels, Ö. Farkas, J. B. Foresman, J. V. Ortiz, J. Cioslowski and D. J. Fox, *Gaussian 09, Revision E.01*, Gaussian, Inc., Wallingford, CT, 2009.
- 136 S. Stimpson, D. R. Jenkinson, A. Sadler, M. Latham, D. A. Wragg, A. J. H. M. Meijer and J. A. Thomas, *Angew. Chem. Int. Ed.*, 2015, **54**, 3000–3003.
- 137 E. Laureto, M. A. T. Da Silva, R. V. Fernandes, J. L. Duarte, I. F. L. Dias, H. De Santana and A. Marletta, *Synth. Met.*, 2011, **161**, 87–91.
- 138 G. Donnert, C. Eggeling and S. W. Hell, *Nat. Methods*, 2007, **4**, 81–86.
- 139 *Matlab R2016a*, The MathWorks Inc., Natick, MA, 2016.
- 140 S. Mai, M. Pollum, L. Martínez-Fernández, N. Dunn, P. Marquetand, I. Corral, C. E. Crespo-Hernández and L. González, *Nat. Commun.*, 2016, **7**, 13077.
- 141 T. Ha and P. Tinnefeld, *Annu. Rev. Phys. Chem.*, 2012, **63**, 595–617.
- 142 G. T. Dempsey, J. C. Vaughan, K. H. Chen, M. Bates and X. Zhuang, *Nat. Methods*, 2011, **8**, 1027–1036.
- 143 S.-H. Wu, C.-Y. Mou and H.-P. Lin, *Chem. Soc. Rev.*, 2013, **42**, 3862.

- 144 A. von Baeyer, *Berichte der Dtsch. Chem. Gesellschaft*, 1871, 555–558.
- 145 M. Ceresole, *DR Pat.*, 1887, **44002**.
- 146 L. D. Lavis, *Annu. Rev. Biochem.*, 2017, 1–19.
- 147 L. D. Lavis and R. T. Raines, *ACS Chem. Biol.*, 2008, **3**, 142–155.
- 148 L. D. Lavis and R. T. Raines, *ACS Chem. Biol.*, 2014, **9**, 855–866.
- 149 L. V. Johnson, M. L. Walsh, B. Chen and J. M. Buchanan, *Froc. Natl. Acad. Sc. USA Cell Biol.*, 1980, **77**, 990–994.
- 150 W. R. Legant, L. Shao, J. B. Grimm, T. A. Brown, D. E. Milkie, B. B. Avants, L. D. Lavis and E. Betzig, *Nat. Methods*, 2016, **13**, 359–365.
- 151 A. Minta, J. P. Y. Kao and R. Y. Tsien, *J. Biol. Chem.*, 1989, **264**, 8171–8178.
- 152 K. R. Gee, K. A. Brown, W.-N. U. Chen, J. Bishop-Stewart, D. Gray and I. Johnson, *Cell Calcium*, 2000, **27**, 97–106.
- 153 E. W. Miller, A. E. Albers, A. Pralle, E. Y. Isacoff and C. J. Chang, *JACS*, 2005, **127**, 16652–16659.
- 154 J. Chan, S. C. Dodani and C. J. Chang, *Nat. Chem.*, 2012, **4**, 973–984.
- 155 Z. Q. Wang, J. Liao and Z. Diwu, *Bioorganic Med. Chem. Lett.*, 2005, **15**, 2335–2338.
- 156 A. Rukavishnikov, K. R. Gee, I. Johnson and S. Corry, *Anal. Biochem.*, 2011, **419**, 9–16.
- 157 V. N. Belov, C. A. Wurm, V. P. Boyarskiy, S. Jakobs and S. W. Hell, *Angew. Chem. Int. Ed.*, 2010, **49**, 3520–3523.
- 158 S. Banala, D. Maurel, S. Manley and K. Johnsson, *ACS Chem. Biol.*, 2012, **7**, 289–

293.

- 159 L. M. Wysocki, J. B. Grimm, A. N. Tkachuk, T. A. Brown, E. Betzig and L. D. Lavis, *Angew. Chem. Int. Ed.*, 2011, **50**, 11206–11209.
- 160 J. B. Grimm, B. P. English, H. Choi, A. K. Muthusamy, B. P. Mehl, P. Dong, T. A. Brown, J. Lippincott-Schwartz, Z. Liu, T. Lionnet and L. D. Lavis, *Nat. Methods*, 2016, **13**, 985–988.
- 161 H. Li, H. Guan, X. Duan, J. Hu, G. Wang and Q. Wang, *Org. Biomol. Chem.*, 2013, **11**, 1805.
- 162 M. V. Kvach, I. A. Stepanova, I. A. Prokhorenko, A. P. Stupak, D. A. Bolibrukh, V. A. Korshun and V. V. Shmanai, *Bioconjug. Chem.*, 2009, **20**, 1673–1682.
- 163 J. B. Grimm, T. Klein, B. G. Kopek, G. Shtengel, H. F. Hess, M. Sauer and L. D. Lavis, *Angew. Chem. Int. Ed.*, 2016, **55**, 1723–1727.
- 164 J. Arden-Jacob, J. Frantzeskos, N. U. Kemnitzer, A. Zilles and K. H. Drexhage, *Spectrochim. Acta - Part A Mol. Biomol. Spectrosc.*, 2001, **57**, 2271–2283.
- 165 K. Kolmakov, V. N. Belov, C. A. Wurm, B. Harke, M. Leutenegger, C. Eggeling and S. W. Hell, *Eur. J. Org. Chem.*, 2010, 3593–3610.
- 166 J. B. Grimm, A. J. Sung, W. R. Legant, P. Hulamm, S. M. Matlosz, E. Betzig and L. D. Lavis, *ACS Chem. Biol.*, 2013, **8**, 1303–1310.
- 167 M. Fu, Y. Xiao, X. Qian, D. Zhao and Y. Xu, *Chem. Comm.*, 2008, 1780.
- 168 G. Lukinavičius, K. Umezawa, N. Olivier, A. Honigmann, G. Yang, T. Plass, V. Mueller, L. Reymond, I. R. Corrêa, Z.-G. Luo, C. Schultz, E. a Lemke, P. Heppenstall, C. Eggeling, S. Manley and K. Johnsson, *Nat. Chem.*, 2013, **5**, 132–9.

- 169 G. Lukinavičius, C. Blaukopf, E. Pershagen, A. Schena, L. Reymond, E. Derivery, M. Gonzalez-Gaitan, E. D'Este, S. W. Hell, D. Wolfram Gerlich and K. Johnsson, *Nat. Commun.*, 2015, **6**, 8497.
- 170 Y. Kushida, T. Nagano and K. Hanaoka, *Analyst*, 2015, **140**, 685–695.
- 171 J. Liu, Y. Q. Sun, H. Zhang, H. Shi, Y. Shi and W. Guo, *ACS Appl. Mater. Interfaces*, 2016, **8**, 22953–22962.
- 172 R. W. Watkins, L. D. Lavis, V. M. Kung, G. V Los and R. T. Raines, *Org. Biomol. Chem.*, 2009, **7**, 3969–3975.
- 173 X. Zhou, R. Lai, J. R. Beck, H. Li and C. I. Stains, *Chem. Commun.*, 2016, **52**, 12290–12293.
- 174 T. Hirayama, A. Mukaimine, K. Nishigaki, H. Tsuboi, S. Hirosawa, K. Okuda, M. Ebihara and H. Nagasawa, *Dalt. Trans.*, 2017, **46**, 15991–15995.
- 175 Y. Koide, Y. Urano, K. Hanaoka, W. Piao, M. Kusakabe, N. Saito, T. Terai, T. Okabe and T. Nagano, *JACS*, 2012, **134**, 5029–5031.
- 176 M. Grzybowski, M. Taki and S. Yamaguchi, *Chem. Eur. J.*, 2017, **23**, 13028–13032.
- 177 A. Fukazawa, S. Suda, M. Taki, E. Yamaguchi, M. Grzybowski, Y. Sato, T. Higashiyama and S. Yamaguchi, *Chem. Commun.*, 2016, **52**, 1120–1123.
- 178 X. Chai, X. Cui, B. Wang, F. Yang, Y. Cai, Q. Wu and T. Wang, *Chem. Eur. J.*, 2015, **21**, 16754–16758.
- 179 R. BOLTON, P. B. D. D. LA MARE and H. SUZUKI, *Recl. des Trav. Chim. des Pays-Bas*, 1966, **85**, 1206–1210.
- 180 I. A. El-Sakka and N. A. Hassan, *J. Sulfur Chem.*, 2005, **26**, 33–97.

- 181 R. Paul, M. A. Ali and T. Punniyamurthy, *Synthesis*, 2010, 4268–4272.
- 182 J. Chen, T. Yuan, W. Hao and M. Cai, *Catal. Commun.*, 2011, **12**, 1463–1465.
- 183 G. Liu, W. Li, Y. M. Zhang, M. Li and S. X. A. Zhang, *Dye. Pigment.*, 2017, **147**, 529–536.
- 184 F. H. Allen, O. Kennard, D. G. Watson, A. G. Orpen, L. Brammer and R. Taylor, *J. Chem. Soc. Dalt. Trans.*, 1987, S1–S83.
- 185 J. F. Chiang, *J. Chem. Phys.*, 1974, **61**, 1280–1283.
- 186 K. Wakita, N. Tokitoh, R. Okazaki, N. Takagi and S. Nagase, *JACS*, 2000, **122**, 5648–5649.
- 187 M. E. Vol'pin, V. G. Dulova, Y. T. Struchkov, N. K. Bokiya and D. N. Kursanov, *J. Organomet. Chem.*, 1967, **8**, 87–96.
- 188 R. J. Newland, M. F. Wyatt, R. L. Wingad and S. M. Mansell, *Dalt. Trans.*, 2017, **46**, 6172–6176.
- 189 K. K. Halder, T. Sen and A. Patra, *Phys. Chem. Chem. Phys.*, 2005, **7**, 3677–3679.
- 190 R. C. Haddon, *JACS*, 1986, **108**, 2837–2842.
- 191 G. Zhang and C. B. Musgrave, *J. Phys. Chem. A*, 2007, **111**, 1554–1561.
- 192 J. Cheriaa, M. Khaireddine, M. Rouabhia and A. Bakhrouf, *Sci. World J.*, 2012, **2012**, 1–9.
- 193 T. Nishida, A. Fukazawa, E. Yamaguchi, H. Oshima, S. Yamaguchi, M. Kanai and Y. Kuninobu, *Chem. - An Asian J.*, 2014, **9**, 1026–1030.
- 194 S. van de Linde, I. Krstić, T. Prisner, S. Doose, M. Heilemann and M. Sauer, *Photochem. Photobiol. Sci.*, 2011, **10**, 499–506.



- 195 T. J. Chozinski, L. A. Gagnon and J. C. Vaughan, *FEBS Lett.*, 2014, **588**, 3603–3612.
- 196 H. Xu, Y. Yang, Y. Z. Zhu and J. Y. Zheng, *Chinese J. Chem.*, 2006, **24**, 1589–1593.
- 197 F. Lin, D. Pei, W. He, Z. Huang, Y. Huang and X. Guo, *J. Mater. Chem.*, 2012, **22**, 11801.
- 198 C. Jacob, G. I. Giles, N. M. Giles and H. Sies, *Angew. Chem. Int. Ed.*, 2003, **42**, 4742–4758.
- 199 L.-Y. Niu, H.-R. Zheng, Y.-Z. Chen, L.-Z. Wu, C.-H. Tung and Q.-Z. Yang, *Analyst*, 2014, 1389–1395.
- 200 A. Mishra, R. K. Behera, P. K. Behera, B. K. Mishra and G. B. Behera, *Chem. Rev.*, 2000, **100**, 1973–2012.
- 201 R. Yang, R. Tian, J. Yan, Y. Zhang, J. Yang, Q. Hou, W. Yang, C. Zhang and Y. Cao, *Macromolecules*, 2005, **38**, 244–253.
- 202 V. G. Pesin, A. M. Khaletskii and V. A. Sergeev, *Zhurnal Obs. Khimii*, 1963, **33**, 1759–1766.
- 203 S. W. Wright and L. D. McClure, *J. Heterocycl. Chem.*, 2004, **41**, 1023–1026.
- 204 Z. Guo, M. Xian, W. Zhang, A. McGill and P. G. Wang, *Bioorg. Med. Chem.*, 2001, **9**, 99–106.
- 205 P. Hrobárik, I. Sigmundová, P. Zahradník, P. Kasák, V. Arion, E. Franz and K. Clays, *J. Phys. Chem. C*, 2010, **114**, 22289–22302.
- 206 R. Edwards, I. Cummins and P. Steel, *PCT Int. Appl.*, 2009, **WO20090343**, 119.
- 207 M. R. Crampton, C. Isanbor and T. C. Willett, *Can. J. Chem.*, 2005, **83**, 1222–

1227.

- 208 F. Song, Z. Li, J. Li, S. Wu, X. Qiu, Z. Xi and L. Yi, *Org. Biomol. Chem.*, 2016, **14**, 11117–11124.
- 209 F. S. Levinson, R. V. Varganov, M. M. Zakiev, I. M. Shakirova, A. B. Sheremetev, D. E. Dmitriev, D. B. Krivolapov, I. A. Litvinov, D. R. Sharafutdinova and Y. Y. Efremov, *Mendeleev Commun.*, 2008, **18**, 329–331.
- 210 A. Yasunori, *PCT Int. Appl.*, 2017, **CN 1065656**, 9.
- 211 H. Heberer and H. Kersting, *J. fuer Prakt. Chemie*, 1985, **3**, 487.
- 212 J. L. Yap, H. Wang, A. Hu, J. Chauhan, K. Y. Jung, R. B. Gharavi, E. V. Prochownik and S. Fletcher, *Bioorganic Med. Chem. Lett.*, 2013, **23**, 370–374.
- 213 N. Lavignac, C. J. Allender and K. R. Brain, *Tet. Lett.*, 2004, **45**, 3625–3627.
- 214 F. J. Dekker, M. Ghizzoni, N. van der Meer, R. Wisastra and H. J. Haisma, *Bioorg. Med. Chem.*, 2009, **17**, 460–466.
- 215 W. Jiang, Q. Fu, H. Fan, J. Ho and W. Wang, *Angew. Chemie*, 2007, **46**, 8445–8448.
- 216 M. Boiocchi, L. Del Boca, D. Esteban-Gómez, L. Fabbrizzi, M. Licchelli and E. Monzani, *Chem. Eur. J.*, 2005, **11**, 3097–3104.
- 217 J. Pan, J. Li, R. Huang, X. Zhang, H. Shen, Y. Xiong and X. Zhu, *Tetrahedron*, 2015, **71**, 5341–5346.
- 218 H. Zhang, J. Liu, C. Liu, P. Yu, M. Sun, X. Yan, J. P. Guo and W. Guo, *Biomaterials*, 2017, **133**, 60–69.
- 219 J.-T. Hou, J.-W. Gao and Z.-H. Zhang, *Monatshefte für Chemie*, 2011, **142**, 495–499.

220 C.-P. Dong, S. Kodama, A. Uematsu, A. Nomoto, M. Ueshima and A. Ogawa,  
*JOC*, 2017, **82**, 12530–12538.